DYNAMIC MODELLING OF COMBUSTION PROCESSES

A Thesis submitted to Cardiff University for the Degree of

Doctor of Philosophy

by

Yong Qin

School of Engineering, Cardiff University, Wales.

2007

ProQuest LLC
789 East Eisenhower Parkway
P.O. Box 1346
Ann Arbor, MI 48106-1346

ABSTRACT

In this thesis, a dynamic model has been developed for oscillating combustion systems. It comprises of three sections, an inlet pipe, a combustor and a tailpipe, in the expectation that this can be adapted to a wide range of combustion systems. The modelling results have been validated against available experimental data from pulsating combustors, whilst further possibilities are considered in the context of neural network modelling.

Neural aided combustion oscillator models (NACO) have been developed for time domain prediction of low frequency oscillations. The NACO method consists of two stages, one is the design of a core-stimulation (CS) model based on the combustion properties; in the second stage the CS model is combined with a compensation neural network, which is trained to interact with and adjust the CS model. The effectiveness of the training of the non-linear models can be verified by predicting and comparing the outputs with experimental data at a wide variety of different conditions. The limitations of this approach however lie in the simplicity of the core-stimulation model and the necessity for large quantities of training data. This leads to the main thrust of this thesis to evolve a generalised dynamic combustion model which has more general applicability and which can be in the fullness of time be integrated with neural network modelling to improve data, using only sparse training data.

The initial section of this dynamic combustion model is the air transmission line, which uses a finite difference model based on the conservation laws combined with a lumped model to realize the time-domain simulation. The experimental components, such as the pressure transducers, mass flow meter, solenoid directional valve, and pneumatic cylinder etc, are connected with the designed control panel. The Microstar Laboratories DAP card is used to realize the data gathering and control signal output from the PC. Based on the certain numerical discrete method for finite difference model and lumped model, the effectiveness of the proposed model is depicted through comparisons of simulated pressure responses against pressures measured by practical experiments on various transmission lines. The simulation results match well with experimental data.

A premixed combustion model based on the conservation laws was then established. The essential features of the combustor geometry, combustion reaction rate, unsteady mixed reactants motion, and fluid dynamics in inlet pipe and tailpipe are accounted for. The governing equations presented identify key characteristic length and time scales, while the numerical simulation of the equations provides a relatively efficient prediction of the combustion pressure oscillations. This is further analysed using FFT analysis to obtain the frequency and amplitude of the pressure oscillations for comparison with experiments. Good results are generally found although the incorporation of the transmission line representation of the combustor inlet pipe reduces the accuracy of the predictions. Reasons for this are discussed as well as the possibility of using this model in conjunction with neural networks.

ACKNOWLEDGEMENTS

It's my great honour to be awarded ORS scholarship from Universities UK and 6,000 pounds scholarship from School of Engineering, Cardiff University.

I express with pleasure my sincere gratitude to my supervisors Prof. Nick Syred and Dr. Yiqin Xue for their enthusiastic support, encouragement and invaluable suggestions.

I would like to thank various members of the School of Engineering, technical staff and students who helped me in the development of my study. Particularly, I would like to express my gratitude to Dr. M. Y. M. Yusop for his kind help in transmission line experiment.

I am deeply grateful to my wife Xiaoqiu Li, my parents and my parents-in-law for their unique support and love. Especially for my parents-in-law, I am thankful for them to help me to take care of my daughter, Siding Qin, after I sent her back to China when she was six-month old. I will also thank the God to bestow me my second baby.

I am also grateful to all my friends.

Abstract ii

Acknowledgements iv

1. INTRODUCTION 1

1.1 Introduction 1
1.2 Dynamic Modelling of Low Frequency Oscillations in a Swirl Burner/Furnace System Using Artificial Neural Networks 2
1.3 Air Transmission Line 3
1.4 Transient Combustion Process 4
1.4.1 Rayleigh Criterion 5
1.4.2 Thermodynamics and Reaction Kinetics of Combustion 5
1.4.3 Thermoacoustic Instability Phenomenon during Combustion 6
1.4.4 Flame Type and Structure 7
1.4.5 Modelling Methods 10
1.5 Aims and Structure of the Thesis 11

2. A REVIEW OF THE USE OF ARTIFICIAL NEURAL NETWORK MODELS FOR COMBUSTION OSCILLATIONS AND APPLICATION TO OTHER SYSTEMS 14

Nomenclature 14
2.1 Introduction 16
2.2 Neural Network Background 19
2.2.1 Neural Networks 19
2.2.2 Learning Algorithms 20
2.2.3 Dynamic Learning Rate 22
2.3 Experiments 24
2.4 The NACO Method and Implementation 25

2.4.1 Combustion Property Modelling 25
2.4.2 The Core-stimulation Model 26
2.4.3 Combustion Dynamic Response Modelling 28
2.5 Prediction and Relevance to the Work in This Thesis 29

3. AIR TRANSMISSION LINE MODEL 40

Nomenclature 40
3.1 Introduction 42
3.2 Governing Equations 44
3.2.1 Continuity Equation 45
3.2.2 Momentum Equation 46
3.2.3 Energy Equation 50
3.2.4 State Equation 51
3.2.5 Vector Form of Equations 53
3.2.6 Coordinate Conversion and Reducing Dimension 54
3.3 Experiments 58
3.3.1 Test-rig and Its Components 58
3.3.2 Transmission Line Diameter Calibration 60
3.3.3 Kinematic Viscosity Calibration 61
3.3.4 Temperature Measurement 62
3.4 Line Simulation 62
3.4.1 Lumped Line Model 63
3.4.2 Finite Difference Model 65
3.4.3 Pressure Wave Simulation for Both-end Blocked Line Model 68
3.4.4 Pressure Wave Simulation for Charging a Large Volume Linked with a Transmission Line 71
3.5 Discussion and Conclusions 72

4. PREMIXED COMBUSTOR MODEL 92

Nomenclature 92
4.1 Introduction 99

4.2 A Premixed Combustor Model 100
4.2.1 Combustor Geometry and Experiment Results 101
4.2.2 General Assumption 102
4.2.3 Conservation Equations in Combustion Zone 102
4.2.4 Conservation Equations in Tailpipe Zone 109
4.2.5 Equation Solution and Initial Conditions 113
4.3 Simulation Results of Premixed Combustor Model 114
4.3.1 Premixed Combustor Model with Steady Supply of Reactants 115
4.3.1.1 Prediction of Pressure and Temperature 115
4.3.1.2 Wall Temperature Effects 117
4.3.1.3 Heat Transfer Coefficient Effects 118
4.3.1.4 Tailpipe Fiction Effects 119
4.3.1.5 Equivalence Ratio Effects 120
4.3.2 Premixed Combustor Model with Variable Supply of Reactants 120
4.3.2.1 Simulation with the Sinusoidal Supply Configuration 121
4.3.2.2 Simulation with a Second Sinusoidal Supply Configuration 122
4.3.3 A Simple PID Control for Steady Inlet Mass Flow 124
4.4 Discussion and Conclusions 125

5. ZERO-DIMENSIONAL PREMIXED COMBUSTION MODEL141

Nomenclature 141
5.1 Introduction 147
5.2 Combustion Model Geometry and Experiment Results 148
5.3 A Zero-dimensional Premixed Combustion Model 149
5.3.1 Conservation Equations in Combustion Zone 150
5.3.2 Conservation Equations in Inlet Pipe 156
5.3.3 Conservation Equations in Tailpipe 161
5.3.4 Equation Boundary Conditions 164
5.3.5 Equation Solution and Initial Conditions 169
5.4 Simulation Results of Zero-dimensional Premixed Combustion Model 169
5.4.1 Prediction of Pressure Oscillation in Combustor 170
5.4.2 Tailpipe Length Effects 171

5.4.3 Inlet Pipe Length Effects 171
5.5 Discussion and Conclusions 172

6. PREMIXED COMBUSTION MODEL BASED ON ONE-DIMENSIONAL TRANSMISSION LINE THEORY 179

6.1 Introduction 179
6.2 Combustion Model Geometry and Experiment Results 180
6.3 Premixed Combustion Model Incorporating One-dimensional Transmission Line Analysis for the Inlet 180
6.3.1 Conservation Equations in Combustion Region 181
6.3.2 Combustion Equations in Inlet Pipe Region 181
6.3.3 Equation Solution and Initial Conditions 183
6.4 Simulation Results of Premixed Combustion Model Incorporating One-dimensional Transmission Line Analysis for the Inlet 183
6.5 Discussion and Conclusions 184

7. CONCLUSIONS AND RECOMMENDATIONS FOR FUTURE WORK 189

7.1 Conclusions 189
7.1.1 Inlet Pipe Model for the Combustor 189
7.1.2 Premixed Combustor Model 191
7.1.3 Zero-dimensional Premixed Combustion Model 192
7.1.4 Premixed Combustion Model Incorporating One-dimensional Transmission Line Analysis for the Inlet 192
7.2 Recommendations for Future Work 193

REFERENCE 196

APPENDIX 206

1. INTRODUCTION

1.1 INTRODUCTION

Passive control of combustion processes has been widely sought to reduce pressure oscillations and pollutant formation, increasing combustion intensity and heat transfer rates, whilst operating the combustor beyond its natural flammability limits. Active control is promising due to a number of reasons: 1) it can be used to overcome some of the tradeoffs inherent in current combustion technology, such as reduced pressure oscillations accompanied by increased pollutant formation; 2) passive control has been shown to be often inadequate as the operating conditions change; 3) actuators such as acoustic drivers and dynamic fuel injectors, which provide means of modulating key variables in the combustion process, as well as fast and accurate sensors such as pressure transducers, radiometers, and photodiodes, are becoming available; and 4) active controllers consume a small fraction of the power generated in the system and hence are feasible for commercial use [1-5].

Thus, it is clear that future progress in understanding transient combustion phenomena such as swirl flows, pulse combustion, explosions, and other similar combustion instabilities is important so as to be able to realize the active control for combustion instabilities. This will require a good and flexible model for combustion and gas-dynamic interactions [6, 7].

With the development of computer technology, it has become possible to realize the time-domain simulation of large scale plant and this has recently been extended to dynamic modelling of low frequency oscillations in a swirl Burner/Furnace system using artificial neural networks [8]. A neural network aided combustor oscillator approach was used to predict combustion pressure instabilities. However it relies on a primitive core stimulation model which needs careful tuning to combustion oscillations and is not capable of covering diverse modulating oscillations. Moreover extensive

training data are needed which are rarely available from expensive (i.e. gas turbine) systems. These systems are normally operated (not unexpectedly) in operational regimes with minimal oscillations and regions of oscillation are quickly passed through. Thus this thesis develops a more generalized combustion model consisting of an inlet pipe, combustor and tailpipe which is calibrated against available pulsating combustor results, with the understanding that in the longer term it can be integrated with the neural network model when sufficient training data is available. A zero-dimension premixed combustion model is developed for a generalise combustor based on the conservation laws. The essential features of the combustor geometry, combustion reaction rate and unsteady mixed reactants motion are accounted for. The governing equations presented identify key characteristic length and time scales. The models predict development of the combustion oscillations in accord with those observed during the experiment especially with the premixed combustion. The consideration of the fluid dynamics in the inlet pipe and tailpipe of the combustion system contributes to the model accuracy. A time-domain simulation of pneumatic transmission lines is useful to capture the air transient characteristics within the pipe lines and interaction with the combustor. The aim of the study has been to provide quantitative tools, which are relatively simple to use and provide solutions in relatively short time-scales, yet are sufficiently elaborate to be of use for design purposes, and can contribute to the understanding of air transmission line interactions with transient combustion and associated tailpipe processes. Ideally it is expected that that this integrated model should be capable of being matched to a wide variety of different oscillating combustion systems, especially when some training data is available for neural network analysis. This can form the foundations for the future of both active adaptive and passive control of pressure oscillations.

1.2 ARTIFICIAL NEURAL NETWORKS FOR MODELLING COMBUSTION OSCILLATIONS

Currently neural networks are of considerable interest. They have great capability in solving complex mathematical problems since they have been proven to approximate any continuous function very accurately [9]. Hence, they have received considerable attention in the field of system identification and controller design [10-24]. In the

system identification stage, the neural network model is developed for a controlled nonlinear plant or process. This network is trained offline in single or batch mode, using data collected from the operation of the plant or process. In the control stage, the neural network identification model is used to design the controller.

Artificial neural networks have been used to model the dynamics of the combustion process in a swirl burner/furnace system which can be made to oscillate under a wide range of conditions by simple variation of geometry and flowrates of fuel gas and air [25]. The simulation using a NAR (non-linear Auto-Regressive) model usually obtains very poor validation results for unseen data and the predicted oscillation amplitude decays to a very small level or becomes far from experimental data as time passes. This is because there are no external varying inputs in the model to stimulate the oscillation, and the prediction accuracy is limited due to noise existing in the measured data used for training. Although the NARMAX (Non-linear Auto-Regressive Moving Average with eXogenous inputs) model considers the external dynamic inputs, it can not be applied until affordable, reliable, high-speed flow rate measurement devices are available.

To overcome these problems, a methodology for building models of such systems is proposed where dynamic flow rate measurement of gas and air is absent, the inputs to the models being pressure time records, measurements of mean gas and air flowrates and the geometry of the furnace. The modelling has two objectives:

- To model the oscillating properties of the system, such as fluctuating pressure frequencies and *rms* amplitude values. This can then be used to build a core-stimulation model.

- To model the time domain dynamic response to pressure oscillation.

Experiments were undertaken on a swirl burner/furnace test rig of typically 100kW thermal input. This system could be made to oscillate in a regular manner by parametric changes such as mean equivalence ratio, mean gas and air flowrates as well as by small changes in geometry [25]. Pressure fluctuations generated by low frequency oscillations were considered, with a fundamental frequency less than 70 Hz. FFT analysis of the

data was carried out to derive the dominant first and second harmonic frequencies for the various combustion conditions investigated. Multilayer perceptron neural networks are applied and a solution to enhance the training converging speed is applied. This is a rule of instant learning performance based on the dynamic learning rate. The effectiveness of the non-linear models trained is verified by prediction and comparison with experimental data. It is shown that the model can give predictions of oscillation frequency and amplitude slightly beyond that of the experimental data upon which it was based. The limitation of this technique is the core stimulation model.

1.3 TRANSMISSION LINES

Fluid power systems, which are a close parallel to some of the work described here, are most commonly simulated using networks of lumped parameter component models, that is, systems of ordinary differential equations (ODEs) and difference equations. It is therefore convenient to have lumped parameter component models for transmission lines. This requires an approximation of the governing partial differential equations (PDE). A survey of linear PDE models for fluid transmission lines has been presented by Stecki and Davis [26, 27].

Watton and Tadmori [28] compared the four most common approximations for fluids: finite differences, finite volumes, the modal method of Hullender et al [29], and the method of characteristics. They concluded that the modal approximation method is the most accurate, convenient, and numerically stable. A variant of the modal method was presented in Piche and Ellman [30].

Compressible fluid models based on the conservation laws have been well established using the Navier-Stokes equations [31]. In this study, the time domain simulation of a pneumatic transmission line is investigated and then applied to the combustion model. The three-dimensional Navier-Stokes equations are firstly reduced to one dimension and coordinate conversion is undertaken to make them be suitable for the pipe model. Then it is combined with the lumped model to simulate pressure waves travelling in the transmission line. The lumped model based on the orifice equations is mainly used to update the boundary conditions during the simulation. Two different applications are

simulated, which are the both-end blocked model and cylinder charging model. Comparisons between the simulation and experimental results indicate that the proposed combination model is an effective means to simulate the dynamics of the pneumatic lines under different conditions.

1.4 TRANSIENT COMBUSTION PROCESS

Continuous combustion processes are prominently encountered in many applications related to power generation, heating and propulsion. Examples include domestic and industrial burners, steam and gas turbines, waste incinerators, and jet and ramjet engines. The characteristics of these processes include a wide variety of dynamic behaviours [32]. Amongst these, pressure oscillations are considered the most significant in terms of their impact on system performance, although flame movement can cause considerable damage. In many applications, pressure oscillations become more severe as the operating condition of the combustors is changed to meet specific performance criteria. For example, fuel-rich or fuel-lean conditions may be desired, depending on the combustor design and whether the performance objective is an increase in the thermal output of a combustor and/or a reduction in nitric oxide emissions respectively. In most cases, pressure oscillations are undesirable since they lead to excessive vibrations resulting in mechanical failures, high levels of acoustic noise, high burn rates, and possibly component melting.

In a typical continuous combustion process, a highly flammable fuel-air mixture is ignited, and the hot gases generated due to the chemical transformation of the mixture. In its simplest form, the combustion process can be considered as a reacting mixture flowing in a constant area duct with a flame anchored at a specific location. The latter ignites the reactants, releasing their chemical energy in the form of heat, thus raising their temperature and reducing their density. Combustion chambers can be viewed as organ pipes or Helmholtz resonators in which acoustic pressure and velocity oscillations can be sustained. Flames, which are essentially surfaces across which reactants are converted into products, not only possess their own inherent instabilities, but are also known to respond readily to imposed oscillations. The potential coupling between the

unsteady components of pressure and heat release rate can lead to their resonant growth, which is referred to as thermoacoustic instability [33].

1.4.1 Rayleigh Criterion

The connection between heat release and pressure has been understood for over a century. In 1878, Rayleigh [34] described the requirements necessary for sustained combustion-driven oscillations, which is known as Rayleigh Criterion. In simplified terms, the Rayleigh Criterion states that the point of maximum energy release should ideally coincide with the point of maximum pressure such that the pressure wave will be sustained.

1.4.2 Thermodynamics and Reaction Kinetics of Combustion

Combustion involves the liberation of energy as chemical reactions proceed, which is determined from the energies of the individual reactants and products. The precise quantity of products, and hence the overall stoichiometry of the reaction, must be established by chemical analysis [33].

For the calculation of the energy released, one basic definition is made in which the energy of an individual chemical species can be given either in terms of its internal energy or its enthalpy is:

$$H = U + pV \tag{1.1}$$

where, H is the enthalpy, U is the internal energy and the product pV indicates the mechanical work done on the system.

The change of enthalpy for a general chemical reaction can be given as the difference of standard enthalpies of formation of reactants and products. To describe the quantitative behaviour of the chemical reaction considered, a rate law may be specified to account for the rate of change of concentration of chemical species, in terms of the product of

concentration terms and rate constants. A rate constant k is usually dependent on the temperature, but is independent from the concentrations. It is normally expressed in the Arrhenius form as:

$$k = Ae^{(-E/RT)} \tag{1.2}$$

where A is the Arrhenius pre-exponential factor, E is the activation energy of the reaction, R is the universal gas constant, and T is the temperature.

1.4.3 Thermoacoustic Instability Phenomenon during Combustion

Chemical-acoustic coupling is concerned with interactions between pressure waves and the chemical processes involved in reactive flows. The acoustic waves may be the natural modes of a system, generated by energy deposited in the system by an external source, or derived from by chemical reactions within the system.

Reports of thermoacoustic instability have a long history, starting in the 19th century, when a number of independent studies revealed that sound of considerable amplitude can be generated when a gas flame is placed inside a large tube, leading to what has become colloquially known as "singing" flames to Rayleigh's famous criterion [35]. Rayleigh's criterion has, over the years, served as an important analytical tool to predict potentially damaging interactions in combustor designs.

Recently, interest has been renewed in this problem [32]. This is because several modern combustion systems, such as lean premixed combustors, ramjet engines, and pulsed combustors, designed for low emissions, fast propulsion, and flexible operations respectively, exhibit this instability in a prominent way. Traditionally, past approaches have been directed toward mitigation of the instabilities, including changing the flame anchoring point, the burning mechanism, and acoustic boundary conditions, and installing baffles and acoustic damper. Interest in operating these systems over a wide range of conditions without running the risk of self-destruction, and maintaining their

NO_x emission levels within desirable limits, has leaded to the exploration of active and adaptive control as possible strategies for achieving the desired performance.

1.4.4 Flame Type and Structure

A flame can be defined as an exothermic combustion reaction, which is self-propagating through space and has a luminous reaction zone. According to whether the fuel and the oxidant have been mixed prior to combustion, flames can be classified into two categories: i) premixed flames, and ii) diffusion flames. In a premixed flame, fuel and oxidant are mixed before entering into the reaction zone, while in diffusion flames fuel and oxidant must diffuse together in order to react [36].

Further classification can be made according to the fluid mechanics of the reaction zone; a laminar flame if the gas flow is laminar and turbulent flame if the gas flow is turbulent. The threshold distinguishing the laminar and turbulent flows is expressed by the dimensionless Reynolds number, (R_e).

$$\mathrm{Re} = \frac{vL\rho}{\mu} \tag{1.3}$$

where v is the gas flow velocity, L is the distance, ρ is the density, and μ is the dynamic viscosity.

If the values of the Reynolds number are less than $2\text{x}10^3$, the flame is laminar, and if R_e is between $2\text{x}10^3$ to 10^4, the flow is at the transition regime from laminar to turbulent. For R_e greater than 10^4 the flow is turbulent [37].

Premixed flames occur in a combustion process in which the fuel and the oxidant mix together before they enter into the combustion zone or when the flame travels in a homogeneous mixture. When a fuel and oxidant mixture enters into a combustor, the reaction is initiated by an energy stimulus to produce a flame (or deflagration). Reaction is then induced in the layer of reactant mixture ahead of the flame front by heat

conduction or diffusion of reactive species from the hot burned gas or reaction zone behind the flame front.

If the premixed reactants are forced to flow towards the flame front, and their velocity is equal to the rate at which the flame would propagate into stagnant gas, i.e. the burning velocity, the flame itself would come to a standstill. This is put into practice in combustion applications involving burners, the design of the appliance being aimed at holding the flame in one position and rendering it immune to small disturbances.

The velocities of premixed flames are limited by transport processes (i.e. heat conduction and species diffusion). The velocities normally do not exceed the speed of sound in the reactant gas. However, it is often found that a flame (propagating wave or deflagration) undergoes a transition to a quite different type of wave, such as the detonation, for which the wave velocity is much higher than the speed of sound. In this type of wave, the chemical reaction is initiated by a supersonic compression, or shock wave, travelling through the reactants.

Diffusion flames occur in a combustion process in which fuel and oxidant are supplied to form a combustible mixture, which is ignited immediately upon its formation. The flame appears at the boundary between the oxidant and fuel zones. Reaction products spread to either side of this boundary, and before they reach the combustion region the oxidant and the fuel diffuse against them [32]. Diffusion flames are very important industrially because of their combustion stability, easy ignition, intense radiation (with certain fuels) and safety, although there is inadequate information about diffusion flames due to the complexities of the chemistry, thermal decomposition of the fuel in the hot oxygen-free region, soot-formation process and the radiative heat transfer.

The dominant physical process is normally the mixing of the fuel and the oxidant as chemical reactive times are very fast. So a clear distinction can be made between flames which involve two different flow regions. The first one is a slow-burning diffusion flame (e.g. candle flames). In this kind of flame, the fuel rises slowly and laminar flow ensues. The mixing process occurs solely by molecular diffusion and thus the flame properties are determined by molecular quantities. The second one is a rapid-burning diffusion flame (i.e. industrial burner, gas turbines) in which the fuel is usually

introduced in the form of discrete droplets (liquid fuel combustion). In the latter, burning is rapid, flow velocities are high and the mixing process is associated with the turbulence of the flow.

Moreover, a laminar flame propagating (and growing) freely in a homogeneous mixture of fuel and air may become turbulent due to the natural instabilities of large flames. In this situation the flame spreads through the fuel and air mixture very rapidly. The flame propagation results in the conversion of the reactants into products in the flame region.

The rate at which the burnt gases are produced depends mainly on the burning velocity. The burning velocity is a property of the mixture but it also varies with other parameters as for instance the temperature and pressure of the surrounding environment and above all with the turbulence level. Hence in laminar conditions the type of fuel together with the concentration of the fuel is the most important parameters which determine the laminar burning velocity. Gases such as acetylene and hydrogen have some of the highest burning velocities among fuels, whilst methane has one of the lowest. As a rule of thumb, it can be said that the laminar burning velocity becomes a maximum just on the rich side of the stoichiometric fuel-air ratio.

Drastic acceleration of flames of large dimensions is induced by the irregularities in the form of the flame. Large flames are naturally unstable and tend to fold and wrinkle increasing their surface area and providing in this way a self-acceleration mechanism. Similarly, congestion or bluff-bodies create turbulence in the environment in which the combustion occurs, providing a mechanism of flame acceleration. Turbulent flames magnify the rates of mass and heat transferred within the flame region, accelerating the combustion process.

1.4.5 Modelling Methods

Four modelling methods are listed by Marsano [38], which are Empirical Models, Phenomenological Models, Computational Fluid Dynamics (CFD) codes, and Phenomenological Scaling.

For empirical models, experimental correlations of a process are determined by experimental data only, which makes it easy for the user to track how the model arrived at a prediction. However, these models are not strictly valid outside the data set upon which they were built, which leads to scaling problems. For phenomenological models, the various components of a physical process are dissected and physically or empirically based sub-models derived. These sub-models are linked together to provide a fully integrated predictive model. Computational Fluid Dynamics codes aim to solve fundamental conservation equations of mass, momentum and energy by solving a complex system of equations using non-linear mathematical solvers. However simplifications are needed mainly due to the complexity of chemistry and turbulence. The codes can, in principle, cope with complex geometries and can incorporate the latest methodology for modelling the more complex aspects of combustion. For very complex physico-chemical process, the researcher sometimes resorts to appropriate scaling parameters. Scaling laws are derived and applied to data from small-scale experiments to model real scale processes. Hence, in this type of models, the geometrical features of the geometry are modelled in detail.

In this study, three premixed combustion models are established. The essential features of the combustor geometry, combustion reaction rate and unsteady mixed reactants motion are accounted for. The governing equations presented identify key characteristic length and time scales.

1.5 AIMS AND STRUCTURE OF THE THESIS

In this thesis an engineering approach to modelling typical transient combustion processes is described, being tested against available pulsating combustor data. The aim is to provide design engineers with quantitative tools, which are relatively simple to use and can provide solutions in relatively short time-scales, yet are sufficiently elaborate to be of use for design purposes. As a further refinement, model parameters are identified which can be adjusted by an available neural network model to widen the applicability of the model to different combustion systems when sufficient training data is available.

In Chapter 2, a combustion oscillation modelling method, neural aided combustion oscillator (NACO), is reviewed [8]. This consists of two stages, combustion property modelling and dynamic response modelling. In the first stage, combustion oscillation properties of dominant resonant frequencies and *rms* values are modelled using neural networks related to a variety of experimental conditions. Integrating the outputs of these trained networks into sinusoidal forms, a core-stimulation (CS) model can be built up based on the experimental condition given, although the range is inevitably limited. The simulation at this stage is usually far from acceptable, with a sustainable oscillating source being obtained at the expected dominant resonant frequencies. In the second stage, the CS model is combined with a compensation neural network (CNN), which is to be trained using sampled patterns of oscillating pressure data and the output of the CS model. The inputs to the CNN consist of steady-state experimental conditions and the history output of the overall network, predicted pressure. This method greatly eases the training time though it consists of two stages, and the effectiveness is due to the CS model with a sustainable oscillation mechanism at the conditions given whilst the CNN makes up for the non-linearity in the complex process. In addition, a dynamic learning rule is established to adjust the learning rate in the training process to appropriate values to speed up or slow down the gradient descent process at the interest of ensuring the overall changing trend is in the target direction, hence enhancing the convergence process. The limitations of the existing core stimulation model are explored and the rational refinement is developed for the dynamic combustion model of the remainder of the thesis.

In Chapter 3, the continuity, momentum and energy equations are presented including the relevant state equations to describe the behaviour of compressible fluids in transmission lines. The derivation of Navier-Stokes equations based on the conservation laws is presented. These equations are then transferred into cylindrical coordinates to make them suitable for the pipe line with circular cross-section. The lumped model is firstly used to simulate the air flow dynamics. The limitations of this method are presented. The finite difference model combined with the lumped model is then proposed to realize the time-domain simulation of an air transmission line.

In Chapter 4, a premixed combustor model is described based on the conservation laws to predict the pressure oscillations. Effects of wall temperature, heat transfer,

equivalence ratio, tailpipe friction and length are also investigated. The model is appraised against experiments. Predicted combustion oscillations are similar to those observed during the experiments. The FFT analysis is used from the Matlab Library to obtain the frequency and amplitude of the pressure oscillations.

In Chapter 5, a zero-dimension premixed combustion model is proposed. The essential features of the combustor geometry, combustion reaction rate and unsteady mixed reactants motion are accounted for. The governing equations presented identify key characteristic length and time scales. The numerical simulation of the equations provides a relatively more efficient prediction of the combustion pressure oscillations. In addition, the pressure in the inlet pipe with a value slightly above atmospheric is considered.

In Chapter 6, a premixed combustor model is combined with a one-dimensional transmission line model, in which the mass fraction equations are included for the pipe lines. The reasons why the simulations based on this model gives poorer results compared with other two models are analyzed.

Chapter 7 draws overall conclusions and recommendations from the work.

2. A REVIEW OF THE USE OF ARTIFICIAL NEURAL NETWORK MODELS FOR COMBUSTION OSCILLATIONS AND APPLICATION TO OTHER SYSTEMS

NOMENCLATURE

A_1	Pressure oscillation amplitudes
A_2	Pressure oscillation amplitudes
B	Data matrix
$e(t)$	Error in core-stimulation (CS) model
E	Error vector
E_r	Equivalence flow ratio
F_g	Flag of learning performance
K	Adaptive factor, dynamic learning
L	Air inlet pipe length
N_c	Merit number, dynamic learning
N_m	Merit threshold, dynamic learning
$p(t)$	Pressure
$p_s(t)$	Output pressure in the CS model
P	Pressure vector
Q_a	Air flow rate
Q_{ga}	Axial gas flow rate
Q_{gp}	Premixed gas flow rate
rms	Root mean squares of the pressure
R	Root of mean squares of model errors
$w(k)$	Neural network weight at instant k
x_i	Unknowns in the CS model
$y(k)$	Expected output at instant k
$y_n(k)$	Neural network output
ω_1	Oscillation frequencies

ω_2	Oscillation frequencies
β	Neural learning momentum
$\Delta w(k)$	Weight adjustment at instant k
$\varepsilon(k)$	Instantaneous sum of the square errors
ϕ_1	Phases in the CS model
ϕ_2	Phases in the CS model
$\eta(k)$	Dynamic learning rate at instant k

2.1 INTRODUCTION

Extensive research has been undertaken in the published literature [39-43] on combustion oscillations to improve the understanding of the nature of the process and to achieve stable performance, especially through passive measures. Adaptive combustion control is an attractive idea because it can be matched to many different situations, providing high performance over a wide range of the operating envelope and eliminating costly design changes typically required in passive approaches [39, 41]. Dynamic models of processes are required to accurately implement adaptive control algorithms, but they can also be useful for passive control. Dynamic modelling techniques have been carried out using various combustion theories [3-5], while application of real time adaptive control using this method is still limited due to the uncertainties in models, which are obtained from practical experiments; also most importantly the reliability of equipment.

Neural networks are increasingly employed in a wide range of applications, such as modelling, prediction, control, classification and pattern recognition, signal processing, optimisation, etc [44-48]. The theoretical justification for the application is that, provided that the network topology is sufficiently large (sufficient number of hidden neurons), any continuous function can be approximated to within an arbitrary accuracy by carefully choosing parameters in the network [49]. The most commonly used types of neural networks are feed-forward, recurrent, and self-organising; for learning algorithms they are back propagation (BP), genetic algorithms (GA), least squares (LS), and reinforcement learning rules.

Recent research [50, 51] has described the application of neural networks in the modelling of combustion dynamics with the effectiveness of neural prediction on combustion pressure oscillation in one experimental condition being shown. The prediction was undertaken in limited steps and the results show the simulation performance deteriorates as the prediction step increases. The dynamic inputs to the network are history pressure predictions; therefore it is actually a NAR (non-linear Auto-Regressive) model, which is expressed in general form as:

$$y(k) = f\left[y(k-1), \cdots, y(k-n_y)\right] \tag{2.1}$$

where $y(\cdot)$ is the output at the generic time sample, n_y is the dimension of the history $y(\cdot)$ and $f(\cdot)$ is the non-linear function, which is a neural network in the study. The prediction of an output variable using the NAR model only depends on the history of the output variable itself, with no external dynamic inputs being considered. In this case, the history prediction error effect dominates the prediction performance as time passes if the model is not trained to high enough accuracy or there is a presence of noise. In reference [18], the same problems were encountered at the early stage of the work in modelling combustion dynamics by a single neural network model using the predicted output as the dynamic inputs. The simulation is usually very poor in validation for unseen data and the predicted oscillation amplitude decays to a very small level or becomes far from experimental data as time passes. This is because there are no external varying inputs in the model to stimulate the oscillation, and the prediction accuracy is limited due to noise existing in the measured data used for training. The NAR model prediction accuracy is more sensitive to the errors in history prediction than the prediction accuracy in the case of using NARMAX (Non-linear Auto-Regressive Moving Average with eXogenous inputs) model, which is generally expressed as:

$$y(k) = f\left[y(k-1), \cdots, y(k-n_y), u(k-1), \cdots u(k-n_u)\right] \tag{2.2}$$

where $u(\cdot)$ is the external input at the generic time sample. As the process dynamic input is considered in the NARMAX model, the prediction output is expected to be more accurate. However in the combustion process modelling, the actual inputs to the burner, dynamic gas and air flow rates, are difficult to measure in practice at a speed as fast as the pressure measurement. Thus the NARMAX model can not be applied until affordable, reliable, high-speed flow rate measurement devices are available.

To overcome these problems, a combustion oscillation modelling method, neural aided combustion oscillator (NACO), was used, which consists of two stages, combustion property modelling and dynamic response modelling. In the first stage, combustion oscillation properties of dominant resonant frequencies and *rms* values were modelled

using neural networks related to a variety of experimental conditions. Integrating the outputs of these trained networks into sinusoidal forms, a core-stimulation (CS) model can be built up based on the experimental condition given, although it is acknowledged that there are frequency range limitations. The simulation at this stage was far from acceptable, with a sustainable oscillating source being obtained at the expected dominant resonant frequencies. In the second stage, the CS model is combined with a compensation neural network (CNN) as shown in Figure 2.1, which is to be trained using sampled patterns of oscillating pressure data and the output of the CS model. The inputs to the CNN consist of steady-state experimental conditions and the history output of the overall network, predicted pressure. This method greatly eases the training time though it consists of two stages, and the effectiveness is due to the CS model with a sustainable oscillation mechanism at the conditions given whilst the CNN makes up for the non-linearity in the complex process. The models of *rms* amplitude and dominant frequencies obtained at the first stage of the NACO method can also be used for steady-state property prediction for the purpose of aiding optimal design for combustion systems. Details of the NACO method are described in the following sections.

Multilayer perceptron (MLP) neural networks and Back-propagation algorithms [45, 47] were used. The weights in the neural networks are trained using the data patterns and learning algorithms. The slow learning problem often concerned is largely due to local minima encountered in the training process. The training can become stuck at a local minimum for a long time or forever due to inappropriate values of the pre-set learning rate. This problem is overcome by a solution of the dynamic learning rate, in which the learning rate is determined by a rule on instant learning performance. The learning rate in the dynamic state matches its value to the learning performance in the training process and local minima situations can be jumped over by the genetic mechanism in the solution, the training process thus being enhanced effectively.

2.2 NEURAL NETWORK BACKGROUND

2.2.1 Neural Networks

The multilayer perceptron (MLP) consists of a set of input neurons which constitute the input layer, one or more hidden layers with nonlinear activation neurons, and an output layer consisting of one or more output neurons as shown in Figure 2.2 (a). A hidden layer neuron consists of a set of synapses or weights relating to every input, an adder for linear summing the input signals weighted by the respected synapses of the neuron, and an activation function for limiting the amplitude of the output of the neuron as shown in Figure 2.2 (b). The most commonly used type of activation function is the sigmoid function as follows:

$$f(net) = \frac{1}{1+e^{-net}} \tag{2.3}$$

or

$$f(net) = \frac{e^{net} - e^{-net}}{e^{net} + e^{-net}} \tag{2.4}$$

which limits the neural output to be within a specified range (0 1) in the former or (-1 1) in the latter. The input layer neurons serve only as distribution points transferring the input signals to each neuron in hidden layer 1. The hidden layer neurons accept the signal from each neuron in the previous layer and compute the weighted summation and activation. The outputs of hidden neurons in a layer are then transferred to each neuron in the next layer as input signals. The network output neuron is usually only a linear weighted summation model, without a nonlinear activation function. Bias is considered as a special input with constant value 1.0 in each neuron. The network learns from the pre-set data, which are in the form of input and output patterns and can be handled pattern by pattern or batch handled subject to training algorithms.

2.2.2 Learning Algorithms

Network training is the process by which the weights are adjusted by algorithms to achieve a network performance, which can match the input/output mapping relations at a specific criterion. The back-propagation (BP) algorithm is commonly used based on the gradient descent method. The BP algorithm requires that the activation function be differential. The hyperbolic activation function is also used, which produces output in the range of -1 to 1. The mechanism of the BP algorithm is used to minimise the error criterion, the instantaneous value of the sum of square errors, $\varepsilon(k)$, defined as follows:

$$e(k) = y(k) - y_n(k) \tag{2.5}$$

and

$$\varepsilon(k) = \frac{1}{2}\sum_{1}^{k} e(k)^2 \tag{2.6}$$

where $y(k)$ is the expected network output and $y_n(k)$ the network output at the training iteration k (i.e., presentation of the k^{th} training pattern). In the forward pass of signals, the weights of the network are all fixed and an input vector effect propagates through the network layer by layer. Finally, a set of outputs is produced as the actual response of the network. During the backward pass, on the other hand, the weights are all adjusted in accordance with the gradient descent method as follows:

$$\Delta w_{ji}(k) = -\eta \frac{\partial \varepsilon(k)}{\partial w_{ji}(k)} + \beta \Delta w_{ji}(k-1) \tag{2.7}$$

then

$$w_{ji}(k+1) = w_{ji}(k) + \Delta w_{ji}(k) \tag{2.8}$$

where $\Delta w_{ji}(k)$ is the weight adjustment to weight $w_{ji}(k)$ connecting the j^{th} neuron in a hidden layer or output layer to the i^{th} neuron in the previous layer at the training iteration k. Thus a value $w_{ji}(k) + \Delta w_{ji}(k)$ is given to $w_{ji}(k+1)$ after this training iteration and the training in which the weights are adjusted on a pattern by pattern basis. The term $\partial\varepsilon(k)/\partial w_{ji}(k)$ is the partial derivative of the error criterion (Equation (2.7)) against the considered weight $w_{ji}(k)$, η (its value is between 0 and 1) is the learning rate and β (its value is also selected between 0 and 1) is the momentum rate. The momentum term that is considered in the gradient descent method is used to improve training time and enhance the stability of the training process. Equation (2.7) is the general form of the gradient descent algorithm, which is applied to adjust each weight, also including the bias weights, in each training iteration. In the training process, weights are of time-varying form and their values are adjusted by iteration along the error surface with the aim of moving them progressively toward the optimum solution.

At the end of each training epoch, such as a cycle of training using all patterns, the assessment of performance is undertaken by comparing the network output with the expected output over the validation patterns using the criterion of root of mean squares (R) as:

$$R = \left[\sum_{k=1}^{M} (y(k) - y_n(k))^2 / \sum_{k=1}^{M} y(k)^2 \right]^{1/2} \tag{2.9}$$

where M is the number of total validation patterns, which can be the same, partially the same or totally unseen data as the patterns used in training. The training is undertaken until the R is less than the pre-set target. Note the R differs from the *rms* amplitude as an oscillation property.

For successful training of a given system, parameters such as learning rate, momentum rate, must be chosen properly, but there is no concrete guide to determine these. Although there are techniques designed to improve the converging speed, like conjugate gradient descent, MLP networks using back-propagation are still time consuming, especially when the training data are large and noisy.

2.2.3 Dynamic Learning Rate

The ideal R curve is a sharp descent straight line to the training criterion target, however in practical training the R curve has up-and-downs, resulting in local minima. For a given network topology, the R curve resulting from training depends on: 1) the initial weights selected randomly; 2) the data used for training and validation; and 3) the learning rate and the momentum rate used. The gradient descent function in the learning algorithm is an approximate way of minimising the error criterion in discrete progressive form. The most controllable term for the R curve for efficient training is the learning rate, which is often a fixed preset value. In the training process, the weights are moving in a non-linear space guided by the learning algorithm, and the training process will frequently encounter local minima. If a large learning rate were used, it would mean fast convergence if the weights were moving in the right direction. However the convergence often can not proceed as the training is encountering a local minima. In this case the weights are swinging between two space locations and the algorithm is incapable of finding new weight moving directions if the same learning rate is kept, as shown as 1→2→1 in Figure 2.2 (c). Smaller learning rates give smaller gradient descent steps, which will lead the training toward the bottom of the valley of the R, 1→3→4 in Figure 2.2 (c). Once the R reaches the local minimum the gradient descent algorithm will search for new directions of all the weights. This will generate a new R curve for each weight until the training reaches overall minimum. The rules for the dynamic learning rate used here is as follows:

$$\eta(k)=\begin{cases}\eta(k)/K & \text{if} \quad F_g=1\\ K\times\eta(k) & \text{if} \quad F_g=-1\\ \eta(k) & \text{else}\end{cases} \tag{2.10}$$

and

$$F_g = \begin{cases} 1 & if \quad N_c > N_m \\ -1 & if \quad N_c < -N_m \\ 0 & else \end{cases} \tag{2.11}$$

where K (its value is between 0 and 1) is the adaptive factor and F_g is a flag to recognise the instant learning performance, which is determined by N_m, a merit threshold. At the end of each training epoch, i.e. a cycle of training using all patterns, a merit number N_c increases by one if the R is decreasing, otherwise N_c is zero, or the merit number N_c decreases by one if the R is not decreasing, otherwise N_c is zero. The flag F_g is set as 1 if N_c is larger than N_m, F_g is –1 if N_c is less than $-N_m$, and F_g is zero in all other cases. N_c is reset to zero after a change is made to the learning rate.

In the training process using the dynamic learning rate, the initial learning rate $\eta(k)$ (k=0) can be set to a large value decreasing to 1 for an initial fast convergence. If the R is decreasing continuously over a set number of epochs, the flag F_g will be set to '1', that means the direction of movements of the weights are correct, and thus the mechanism will accelerate the convergence by increasing the learning rate. On the other hand, if the R is not decreasing consecutively over the set number of epochs, the flag F_g will be set to '-1', the changing of weights will be constrained by reducing the learning rate to obtain opportunities of moving the weights in the correct direction. The dynamic learning rate mechanism will bring the learning rate to an appropriate value for continuing the converging process. Using the dynamic learning rate for the learning performance will be very effective in overcoming the sticking of the training process as the learning pace is regulated by the instant learning performance. The convergence will be finally limited by the complexity of the system to be learned and noise in the patterns used. However, the model trained would give a much better result than that derived from the fixed learning rate.

There are two arbitrary parameters in the dynamic learning method, the merit threshold N_m and the adaptive factor K, both of which affect the training. Use of a small value of K will result in large rate of change of the learning in a changing event. Thus too small a value of K will lead to too large changes of learning rate; this is not expected. It is thus reasonable to consider a value of K which is less than but close to 1.0. However, with a

value of K too close to 1.0, the training process would be very slow as it will need too many events of learning rate change to overcome a local minima. Thus a reasonable choice for K is around (0.8 1). There is no boundary found for the merit threshold N_m. However if it is too large, it will take too many epochs to have a change of learning rate and the training process will be very slow. On the other hand, if it is too small it will result in too frequent changes of learning rate, which is unnecessary and may interrupt the acceptable pace of the gradient descent process. A starting value of N_m as 10 was considered.

The method of dynamic learning rate converts the initialised value of learning rate to a time-varying dynamic state in the training process, and changes of the learning rate are undertaken based on the genetic reproduction conception, which awards promising seeds more space to develop and constraint growing of deteriorating seeds. The learning rate is adjusted to appropriate values to speed up or slow down the gradient descent process in the interests of maintaining the overall trend of the R in the target direction, thus enhancing the training process.

2.3 EXPERIMENTS

Reference [45] shows results of modelling experiments undertaken on a 100 kW natural gas fired swirl burner/furnace system. The schematic of the burner with two tangential air entries is shown in Figure 2.3 (a). Variation of swirl number was achieved by the use of removable inserts in the two inlets, the experiment setup being depicted in Figure 2.3 (b). The oscillation of the system could be substantially altered by variations in the length of the inlet pipe, L, to the system, Figure 2.3 (b), and this was employed to generate large quantities of oscillation data (66 sets) for a given swirl burner/furnace combination, coupled with variations in equivalence ratio *(Er)* and quantity of natural gas supplied to the premixed (Q_{gp}) and axial (Q_{ga}) inlets. Other variables included the exit pipe length (L) and total airflow (Q_a)

Typical signals obtained from the pressure transducer are shown later in this chapter with predictions in Figure 2.8. *rms* values of pressure were obtained directly from an FFT analyser. Figure 2.4 (a) shows a phase locked pressure signal of the fluctuations in

the furnace, with superimposed phase angles, used for phase locked velocity measurements, reported in [45]. Figure 2.4 (b) shows a typical output from the FFT analyser, showing the two major harmonic frequencies generally found.

2.4 THE NACO METHOD AND IMPLEMENTATION

The NACO method consists of two stages, combustion oscillation property modelling and combustion dynamic response modelling. The oscillation properties modelled were resonant pressure frequencies and *rms* amplitude values. The resonant frequencies modelled in first stage were used in the second stage for a time domain model. The *rms* values can be calculated directly using the measured pressure data. Harmonic frequencies at each experimental condition can be obtained by undertaking FFT analysis of the measured pressure data, Figure 2.4 (b). The two dominant resonant frequencies, which vary for given test conditions were only considered.

2.4.1 Combustion Property Modelling

The objective of the first stage of the NACO method was to model the combustion oscillation properties of resonant frequencies and *rms* using neural networks. Each of the properties (oscillation frequencies) of ω_1 (first harmonic), ω_2 (second harmonic) and *rms* is modelled using an independent network, the general topology being shown in Figure 2.5 (a). The training data are input-output patterns, and the inputs to the three networks are the same; these are the experimental conditions for the equivalence ratio *Er*, the premixed gas flow rate Q_{gp} and the inlet pipe length *L*. The ranges of the parameters in the 66 experiments were as follows:

$$\begin{cases} Er & 0.62 \text{ to } 0.88 \\ Q_{gp} & 100 \text{ l/min and } 120 \text{ l/min} \\ L & 1.7\text{m}, 4.3\text{m and } 7.7\text{m} \end{cases}$$

The data of each experiment were processed for the corresponding resonant frequencies and *rms* values, thus 66 patterns of *Er*, *L*, Q_{gp}, ω_1, ω_2 and *rms* are used for the subsequent data-based modelling and analysis. The patterns are numbered and odd number patterns were used in training the combustion property models; all were used for validation.

In the modelling of the frequency ω_1 as the output of the network, the number of neurons in the first layer is 10, 5 in the second layer, initial learning rate being 0.1, adaptive factor K 0.9 and the merit threshold number N_m 10. The training process at the dynamic learning rate took 25 minutes finishing at a value of R of 0.01 as shown in Figure 2.5 (b). The process for the fixed learning rate was terminated by the operator at 90 minutes as the training was stuck at a local minimum as shown in Figure 2.5 (c). The variation of learning rate in the dynamic learning process is shown in Figure 2.5 (d), learning rate fluctuating between 0.1 and $2.5\text{x}10^{-5}$. In the modelling of frequency ω_2 and *rms* as the output of the network, the topology of the network and parameters set for training are the same as in modelling ω_1. All the above training tasks were completed successfully. The value of R is 0.017 in validation of ω_1 and 0.011 for ω_2. The validation of the *rms* was carried out for a wide range of equivalence ratios, where predictions within and beyond the experimental conditions are depicted. Validations at all the conditions used in the experiments are shown in Figure 2.6.

2.4.2 The Core-stimulation Model

With the modelled resonant frequencies ω_1 and ω_2 with experimental inputs of the flow-rates of air, natural gas and the inlet duct geometry, as described in section 2.4.1, a core-stimulation (CS) model was used as follows

$$p(t) = A_1 \sin(\omega_1 t + \phi_1) + A_2 \sin(\omega_2 t + \phi_2) + e(t) \tag{2.12}$$

where A_1 and A_2 are amplitudes, ϕ_1 and ϕ_2 are phases, and $e(t)$ is the model error. The unknowns, A_1, A_2, ϕ_1 and ϕ_2 in Equation (2.12) can be determined using the process below.

Equation (2.12) can be expanded as

$$p(t) = x_1 \sin(\omega_1 t) + x_2 \cos(\omega_1 t) + x_{31} \sin(\omega_2 t) + x_4 \cos(\omega_2 t) + e(t) \tag{2.13}$$

where x_i (i=1-4) are unknowns. Using initial n data sets measured at a given experimental condition, Equation (2.13) can be written into matrix form as,

$$P=BX+E \tag{2.14}$$

where $P=[p(t_1)\ p(t_2)\ \ldots\ p(t_n)]^T$, $X=[x_1 x_2 x_3 x_4]^T$, $E=[\ e(t_1)\ e(t_2)\ \ldots\ e(t_n)]^T$ and B $(n\times4)$ is the matrix with each row as $[sin(\omega_1 t)\ cos(\omega_1 t)\ sin(\omega_2 t)\ cos(\omega_2 t)]$ at a different instant t. Minimising the error vector E, the unknown vector can be solved using the least squares algorithm as:

$$X=(B^TB)^{-1}B^TP \tag{2.15}$$

Therefore the unknowns in Equation (2.12) can be obtained as:

$$\begin{cases} A_1 = \left(x_1^2 + x_2^2\right)^{1/2} \\ \phi_1 = x_2 / x_1 \\ A_2 = \left(x_3^2 + x_3^2\right)^{1/2} \\ \phi_2 = x_4 / x_3 \end{cases} \tag{2.16}$$

The first approximation for the CS model is therefore,

$$p_s(t) = A_1 \sin(\omega_1 t + \phi_1) + A_2 \sin(\omega_2 t + \phi_2) \tag{2.17}$$

This CS model is far from satisfactory as the combustion process is much more complex than the combination of sinusoids, hence the development of more complex models. The various parameters in the equation are optimised by minimising the error $e(t)$, whilst the model provides a sustainable oscillation source at the same frequencies as the pressure response resonant frequencies for the given experimental conditions.

2.4.3 Combustion Dynamic Response Modelling

The objective of the second stage of the NACO method is to build a time domain model for the prediction of the pressure oscillation in combustion. The CS model in Equation (2.17), built by modelling the resonant frequencies at the first stage for a given experimental condition, is combined with a compensation neural network, as in the scheme shown in Figure 2.1. Details of the topology of the CNN and the NACO method are shown in Figure 2.7, where steady-state experimental conditions Er, L and Q_{gp} and the history of the predicted pressures, $Pn(k-1)$, $Pn(k-2)$, ..., $Pn(k-m)$, are used as the inputs to the CNN; there is only one hidden layer m, the history dimension of $Pn(\cdot)$ in the model; this is chosen to be 100. As the sampling frequency is 2560Hz and the maximum harmonic frequency is found to be close to 120Hz, at least 4.6 harmonic history cycles of pre-predicted data are used in the CNN model for prediction purposes. In this study the output neuron of the CNN is designed with a hyperbolic activation function. The output of the CS model Equation (2.17), which is an oscillation signal of the frequencies predicted at the given experimental condition, is added with the output of the CNN to give the prediction, $Pn[k]$. The error of this prediction, $e[k] = P[k] - Pn[k]$, and the measured data are used in the BP algorithm, back propagating through the CNN with the weights being updated.

103 inputs are provided to the CNN, 100 being history NACO output data and the other three being the experimental conditions Er, L, and Q_{gp}. The initial learning rate is set as 0.05, adaptive factor K is 0.9 and merit threshold is 10. 5000 patterns at different experimental conditions from 12 files are applied in the training, which took 130 minutes to reach R 0.05 using a relatively old computer.

Validation of the model obtained via the derived NACO method was undertaken by comparing the model simulation with the unseen data at a variety of experimental conditions, three traces being shown in Figure 2.8. The oscillation trends are followed very well in frequency and amplitude. Characterisation of the errors between prediction and measured data give the root of the mean squares of the error as 10.23% in Figure

2.8 (a), 9.35% in Figure 2.8 (b) and 8.22% in Figure 2.8 (c). These errors could have been significantly reduced by extended periods of training, or indeed via the use of a better core stimulation model.

2.5 PREDICTIONS AND RELEVANCE TO THE WORK IN THIS THESIS

The models built in the first stage of the NACO method predict the oscillation properties of *rms* amplitude and dominant resonant frequencies using the experimental conditions and the burner geometry, these being key factors which influence system instability. Therefore these models can provide a powerful tool to investigate instability in a wide range of different combustion situations. However, there are clear frequency domain limitations in the core stimulation model in that, for instance, only two dominant resonances are predicted.

The predictions and experimental results agreed well for the two dominant resonant frequencies and *rms* pressure fluctuations, for most conditions the oscillation occurs in a regular and sustained manner over a range of equivalence ratios from 0.62 to 0.88. Several interesting phenomena were also predicted, including a peak in *rms* pressure at an equivalence ratio of around 0.8, also at an inlet pipe length of 7.7 *m* significant frequency jumps at equivalence ratios around 0.8, Figure 2.6. The effectiveness of the steady-state prediction techniques is also illustrated by Figure 2.8 where predictions of the actual pressure dynamics are made. However prediction of another 256Hz oscillation [25] was not possible at the same time, showing up the limitations of the method at the moment.

The review of the use of neural networks for combustion oscillation and instability prediction has clearly shown the possibilities of the method. However, the technique will always be limited by a lack of training data, except that from small scale systems, as it is not possible to run, for instance, gas turbine systems in operational ranges where serious oscillations can occur. Any training data is likely to be sparse and of limited extent.

For this reason it is clear that better models of oscillating and unstable combustion systems are needed that can better represent processes occurring in such systems and form the basis of the Core Stimulation model, whereby the neural network is used to adjust a variety of model parameters to better fit any training data that is available. Naturally the advance of computer power makes such approaches possible. These models can also be clearly used as a first stage predictor without neural network assistance.

The other problem with the work reviewed in this chapter is that the extensive training data comes from a very complex combustion aerodynamic system, a swirl burner furnace. In order to develop a general purpose combustion model, which can be used to represent a range of systems, very detailed data available from a pulsating combustion system have been used for validation. This has allowed a model to be developed incorporating an inlet pipe, combustor and tailpipe, as discussed in the rest of this thesis.

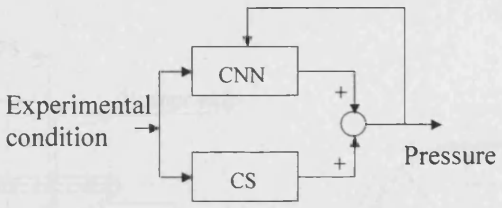

Figure 2.1: Neural aided combustion oscillator (NACO) scheme

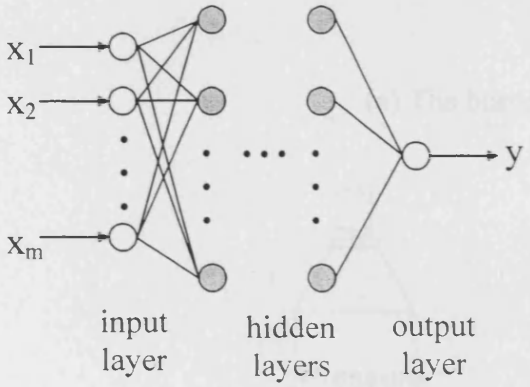

(a) A MLP network

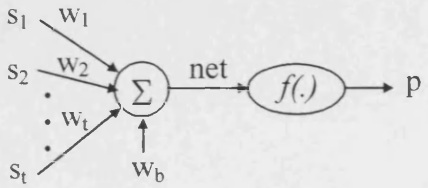

$$net = \Sigma\, w_i\, s_i + w_b$$

output $p = f(net)$

(b) A neural model

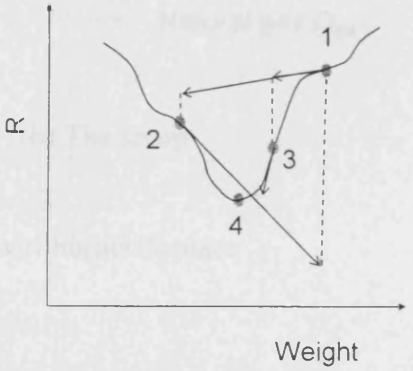

(c) A local minimum

Figure 2.2: A typical neural network

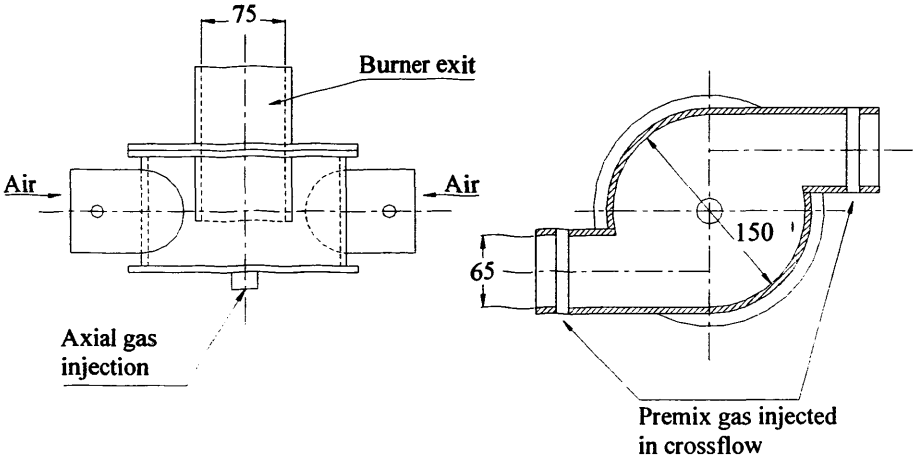

(a) The burner

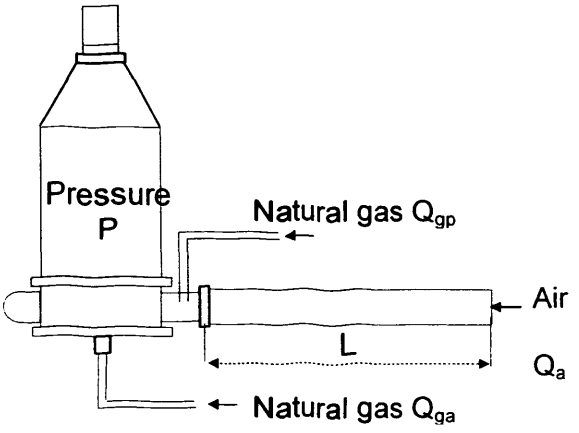

(b) The setup

Figure 2.3: Schematic of a swirl burner/furnace

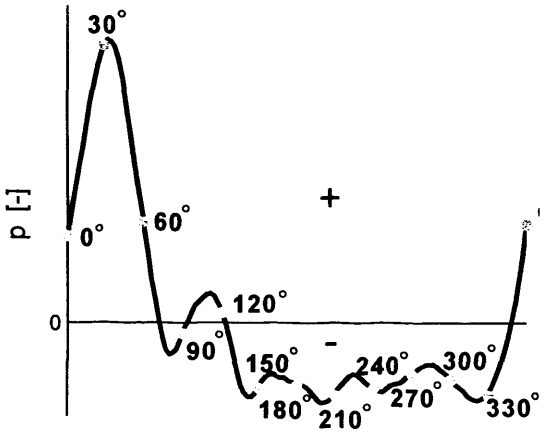

(a) Typical trace of a Phase Locked Pressure Oscillation recorded on the side of the furnace

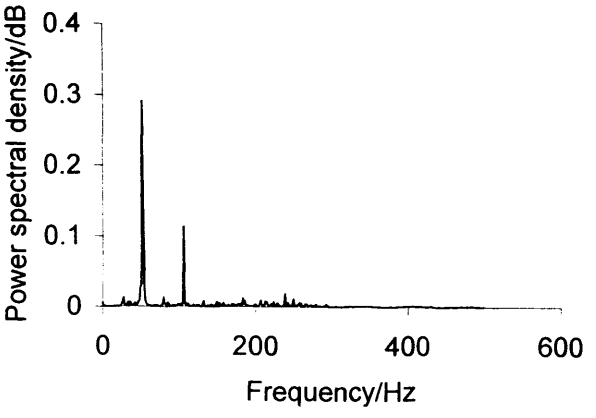

E_r=0.86, Q_{gp}=100 *l/min*, L=1.7*m*

(b). A FFT result

Figure 2.4: Combustion oscillation

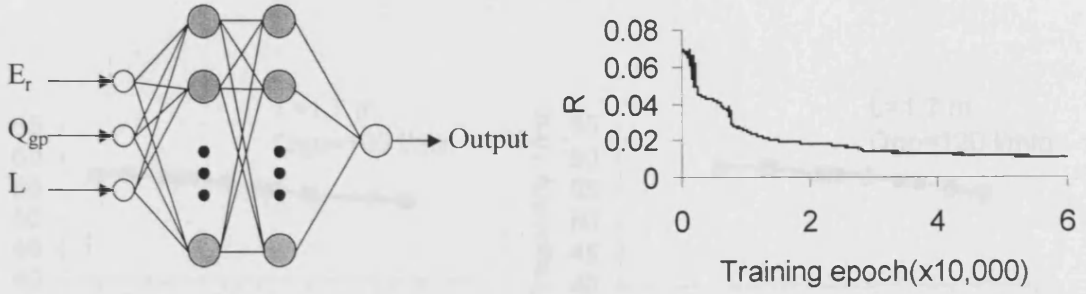

(a) Topology (b) R in the training, dynamic learning rate

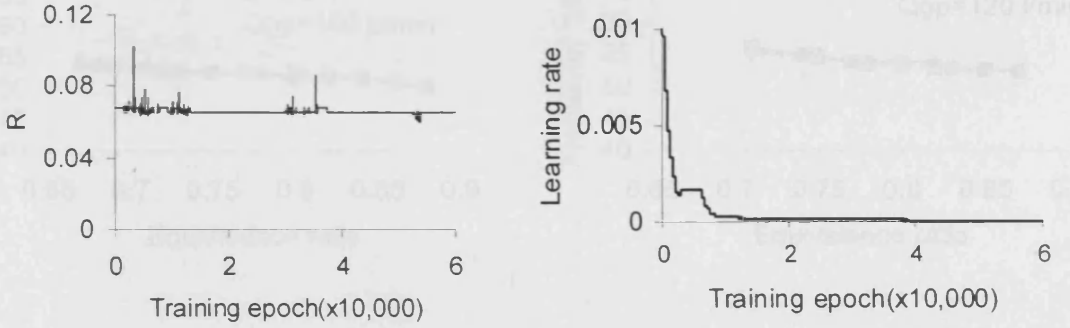

(c) R in the training, fixed learning rate (d) Dynamic learning rate

Figure 2.5: Combustion properties modelling using neural networks

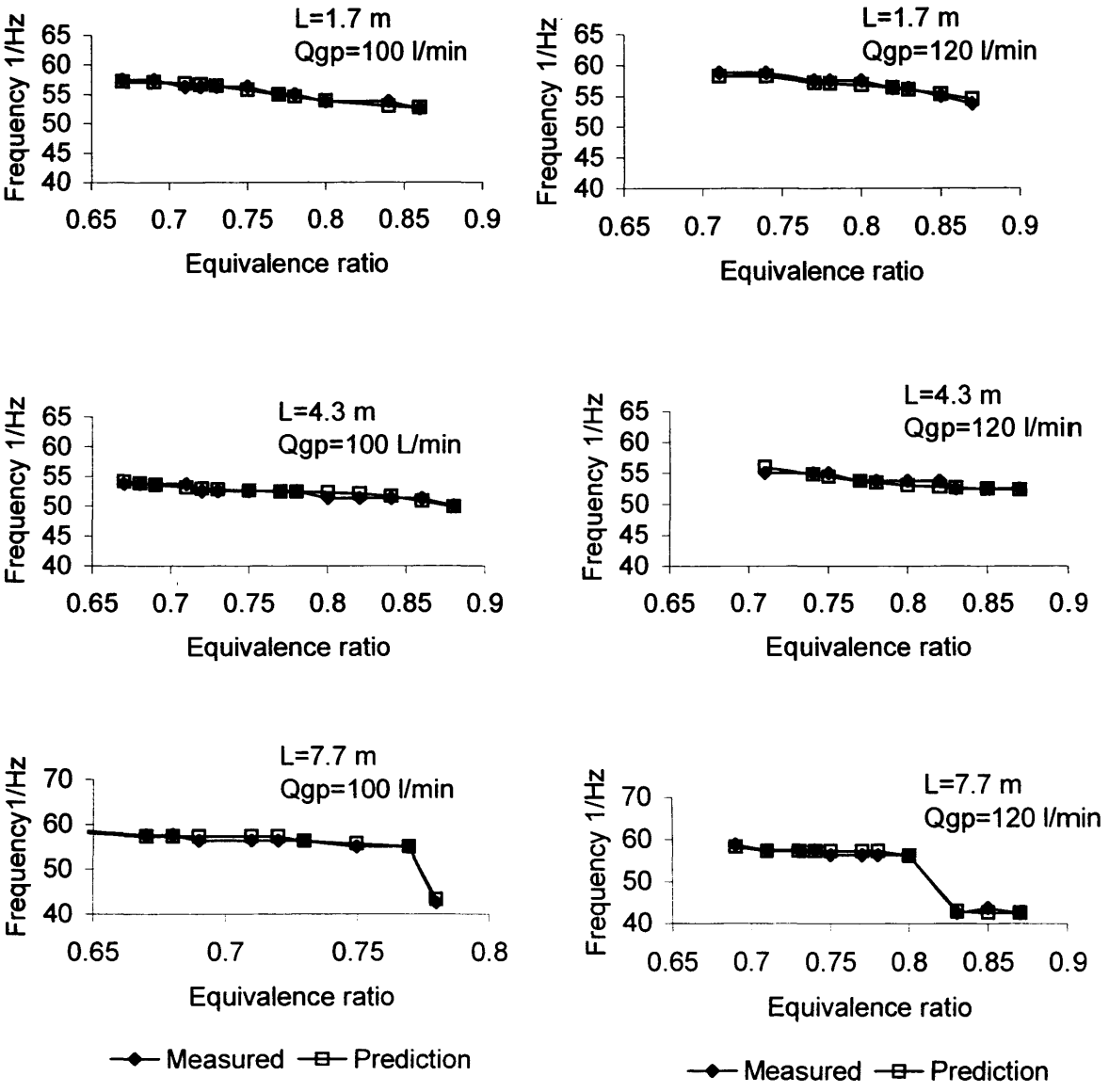

(a) Validation of modelling of resonant frequency ω_1

[continued]

Figure 2.6: Validation of neural networks modelling of combustion properties

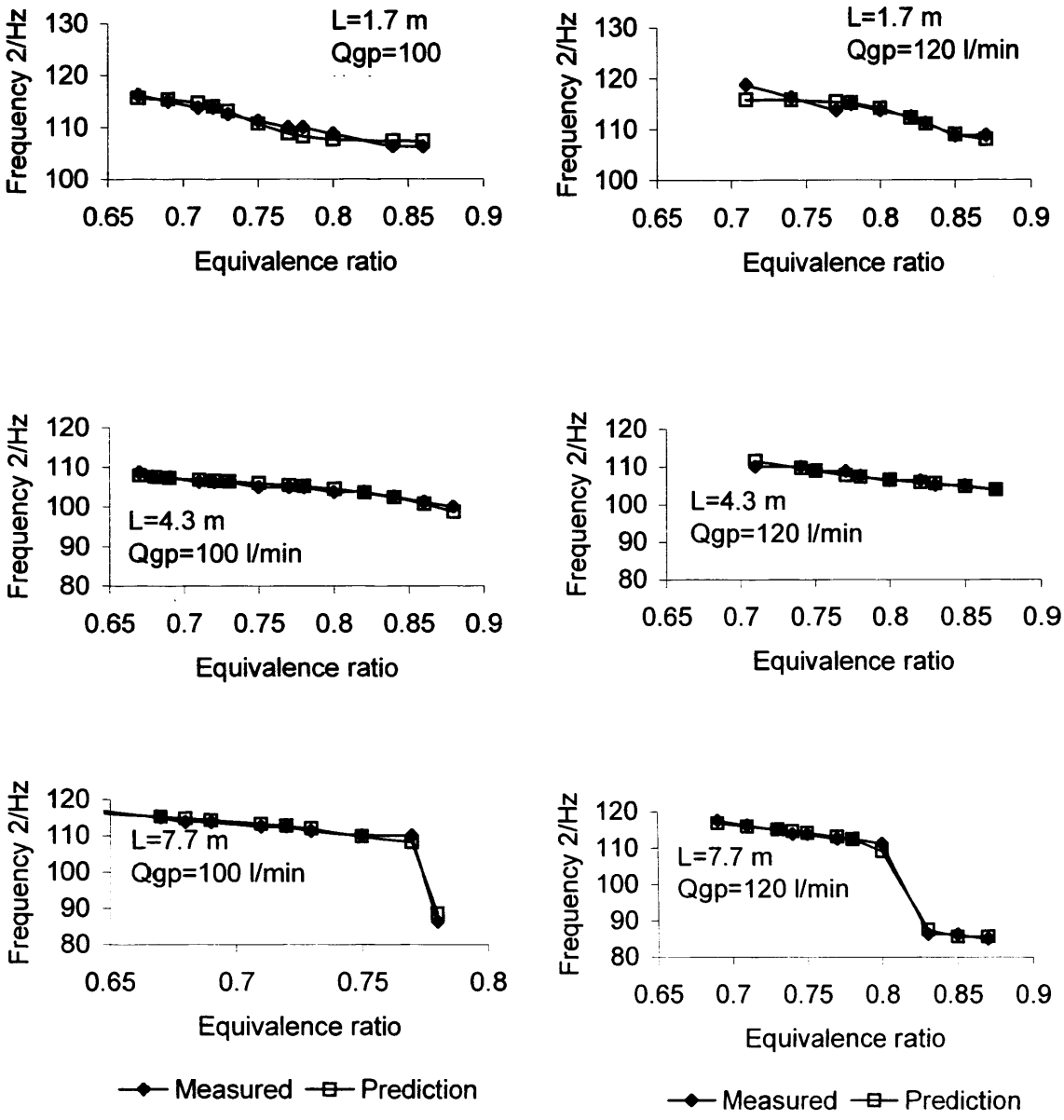

(b) Validation of modelling of resonant frequency ω_2

[continued]

Figure 2.6: Validation of neural networks modelling of combustion properties

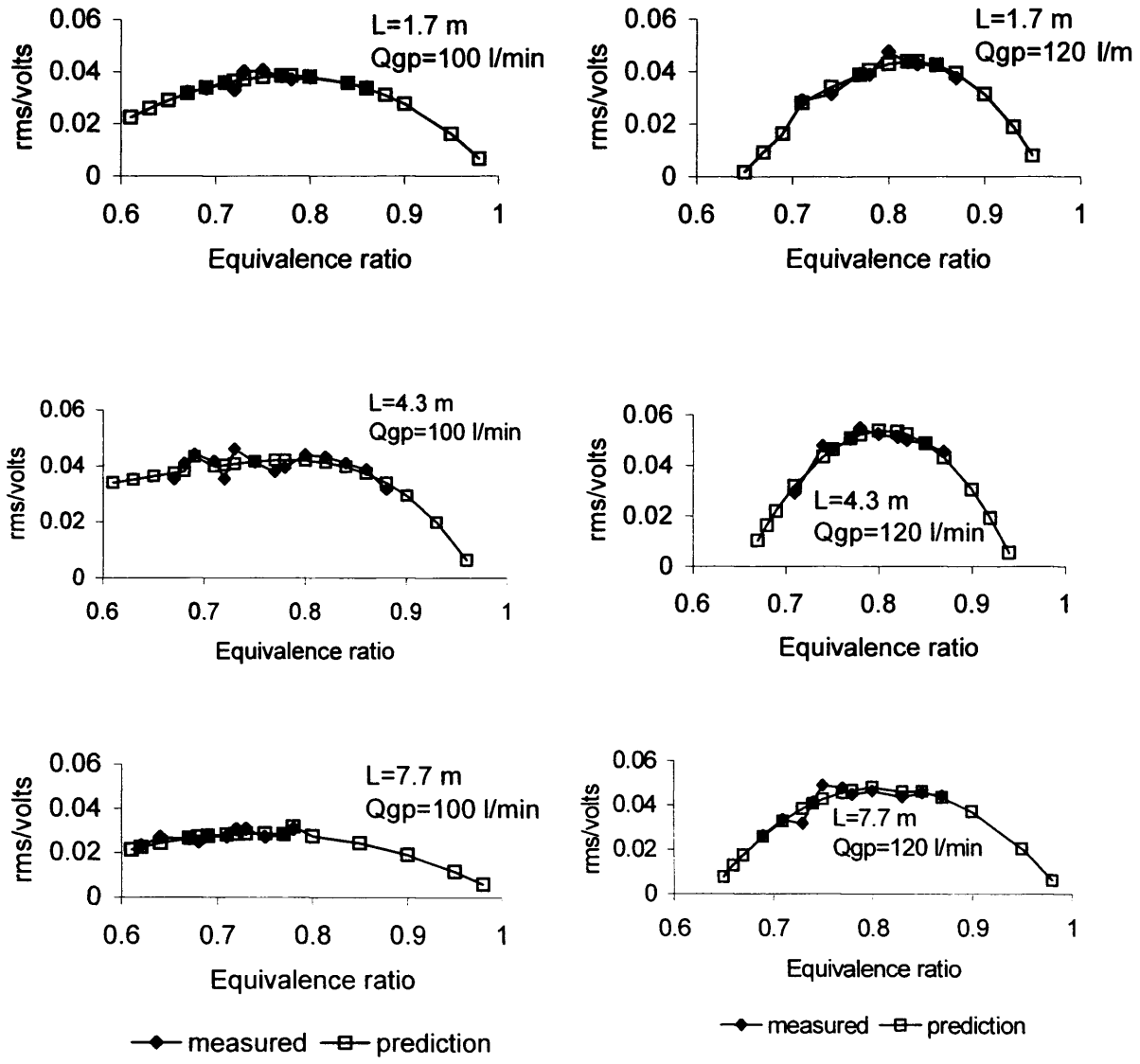

(c) Validation of *rms* modelling

Figure 2.6: Validation of neural networks modelling of combustion properties

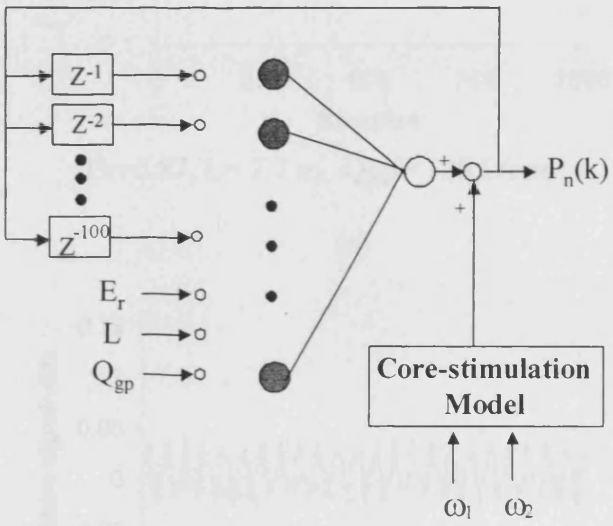

Figure 2.7: Topology of the NACO modelling method

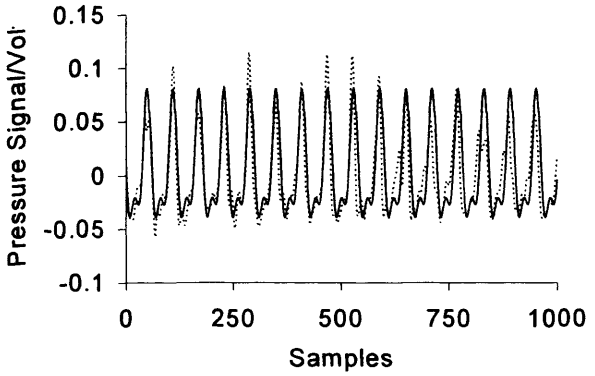

Er=0.87, L= 7.7 m, Qgp= 120 L/min

(a)

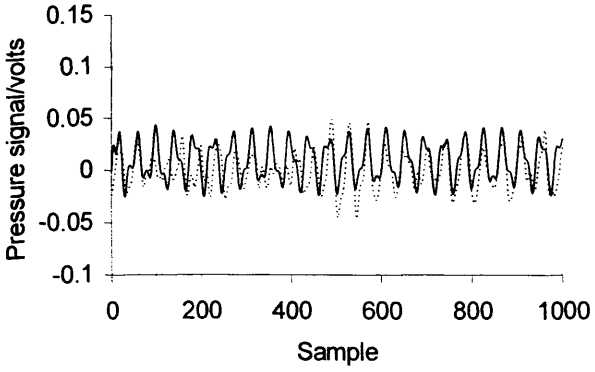

Er=0.67, L=7.7 m, Qgp=120 L/min

(b)

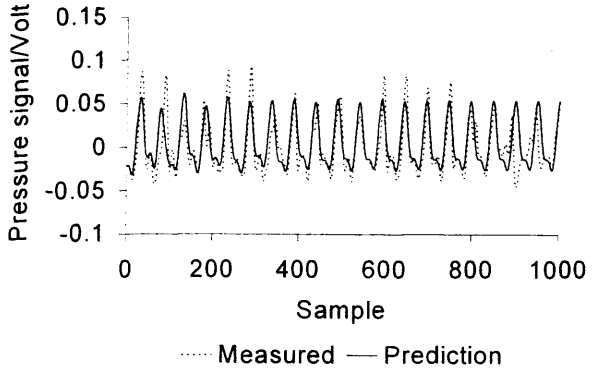

Er=0.88, L=4.3 m, Qgp=100 L/min

(c)

Figure 2.8: Validation of the NACO modelling method

3. INLET PIPE MODEL FOR THE COMBUSTOR

NOMENCLATURE

A	Orifice area or cross-section area of the transmission line
C_d	Discharge coefficient
C_m	Mass flow parameter
C_p	Specific heat at constant pressure
C_v	Specific heat at constant volume
d	Inner diameter of the transmission line
e	Internal energy per unit mass
E_t	Total energy per unit volume
F	Total force vector
f	Body force vector per unit volume
f_x	x components of the body force vector per unit volume
f_y	y components of the body force vector per unit volume
f_z	z components of the body force vector per unit volume
g	Acceleration of gravity vector
k	Coefficient of thermal conductivity
l	Segment length
M_d	Mass flow rate
m_i	Mass in segment i
p	Pressure
P_s	Pressure from the air supply
P_u	Upstream stagnation pressure (absolute)
P_{vc}	Static pressure at the vena contracta or throat
q	Rate of heat lost by conduction (vector)
q_x	x components of heat lost rate by conduction

q_y	y components of heat lost rate by conduction
q_z	z components of heat lost rate by conduction
Q	Heat produced per unit volume by external agencies
R	Gas constant
T	Temperature
T_u	Upstream stagnation temperature (absolute)
u	x components of the velocity vector
V	Fluid velocity vector
V_i	Volume of segment i
v	y components of the velocity vector
w	z components of the velocity vector

GREEK LETTERS

Δp	Pressure drop along a pipe segment
Δt	Time interval for finite difference model
Δx	Spatial interval in x direction for finite difference model
ρ	Density
μ	Dynamic viscosity
μ'	Second viscosity coefficient
ν	Kinematic viscosity
κ	Bulk viscosity coefficient
γ	Ratio of the specific heat
τ_{ij}	Viscous stress tensor
δ_{ij}	Kronecker delta function
$\prod_{ij}$	Stress tensor

3.1 INTRODUCTION

In recent decades, there has been great development and interest in utilising pneumatic systems as a transmission medium. The earlier systems used air as the working medium, but nowadays inert gases are used in some applications. Inefficiency of compression of gases and the dangers involved with storing high pressure gases limit that the working pressure are being designed normally for 10 bar operation. This means however there is extensive theory in this area enabling models to be developed for the inlet pipe section of combustors, especially relevant with gas turbines, where operating combustor pressures can be 20 bar or more.

There are several mature theories on steady state analysis of pneumatic systems, especially in the frequency domain [52-54]. However the dynamic analysis of pneumatic systems in the time domain is still not well developed.

Courant and Friedrichs [55] show how the notion of characteristic directions can be extended to n quasi-linear partial differential equations in two independent variables. Again, characteristic directions are sought. For n equations, there are n characteristic directions through each point. Some may be coincident. With this extension, the size of the computation is greatly increased and not too many problems have been solved for $n>2$. Further generalizations can be made when more than two independent variables are involved. Courant also outlines possible procedures. Based on these, Lister [56] analyzes the computational procedures of the numerical solution of hyperbolic partial differential equations by the method of characteristics, in which the basic technique is related to the case of two equations in two unknown variables.

Hartree [57] develops the mathematical foundations of a theory for a method of characteristics approach to one-spatial-dimensional, unsteady gas flow organized on a rectangular grid of predetermined dimensions. Streeter and Wylie [58] discuss a rectangular grid scheme for hydraulic transient analysis by the method of characteristics in detail. A simple bulk modulus treatment of compressibility is, however, inadequate for a pneumatic line. An equation of state is used instead, Manning [59]. Manning used

the method of characteristics for pneumatic line flows with a rectangular grid scheme. The perfect gas equation and the isentropic relations, together with the perfect gas relation for sonic velocity are used to replace the density and pressure in the continuity and momentum equations to make these two equations only contain the velocity terms. For simplicity, the heat transfer, viscosity, three-dimensional effects and local changes in entropy across travelling pressure waves are neglected in Manning's analysis. The correct determination of characteristic lines directions is the key point for this method. To some extent, previous computations, experimental results, or educated guess might be used to estimate the probable range of those two replaced variables in the pneumatic line being analyzed.

Ikeo et al [60] use the bond graph approach for systematic modelling of pneumatic systems. Krus [61, 62] uses an alternative approach, distributed modelling, for pneumatic system. In distributed modelling, the wave propagation effects are modelled, which introduces physically motivated time delays that can be used to isolate different parts of the system from each other numerically in each time step. One of the interesting properties of distributed modelling shown in those two papers is that it is possible to solve the equations of a subsystem or components independently from other subsystems or components. Hence it can be used for large-scale systems.

Bao et al [63] use a SIMPLE algorithm with domain decomposition to calculate the two-dimensional viscous flow field of tube. The decomposition method is mainly to dispose of the boundary condition. Bao finds that the pressure pulse in the tube is relevant to the ratio of length to diameter. The higher of the ratio, the lower the pressure pulse. Hence, the ratio is an important factor in reaching the orifice characteristics of a tube.

Xue and Yusop [64] separate the transmission line into different segments and treats each of them as a lumped volume. The equations of the fluid passing through an orifice are then utilized to calculate the mass flow rate, which is then used to update other primitive variables related with the transmission line dynamics. The time-domain simulation of the air charging the pneumatic systems is investigated.

Frequency-domain modelling of a transmission line with compressible fluid is addressed in [65], and the influence of wall viscoelasticity on line dynamic behaviour is expressed

in [66]. Based on this, Franco and Sorli [67] implement a line model as described in [30] in the Matlab-Simulink environment in the time domain. Franco separates the transmission line with different segments, each of which is considered as an electric circuit. The pneumatic lines under different operating conditions are then simulated in the time domain.

Compressible fluid models based on the conservation laws have been well established, [31, 68-75]. Here, the time domain simulation of a transmission line is investigated relevant to inlet pipes on combustors. The three-dimensional Navier-Stokes equations are firstly reduced to one dimension and then the coordinate conversion is undertaken to make them suitable for the pipe model. Then it is combined with a lumped model to simulate the pressure wave travelling in the transmission line. The lumped model [64] is mainly used to update the boundary conditions during the simulation. Two different applications are simulated, which are both-end blocked model and cylinder charging model. Comparisons between the simulation and experimental results indicate that the proposed combination model is an effective means to simulate the dynamics of the pneumatic lines under different conditions [76].

3.2 GOVERNING EQUATIONS

The fundamental equations of fluid dynamics are based on the following universal conservation laws [31, 68-75], which are:

1) Mass Conservation

2) Momentum Conservation

3) Energy Conservation

The equation that results from applying the mass conversation law to a fluid is called the continuity equation. The momentum conservation law is nothing more than Newton's Second Law. When this law is applied to a fluid flow, it yields a vector equation known as the momentum equation. The energy conservation law is identical to the First Law of

equation. In addition to the equations developed from these universal laws, it is necessary to establish relationships between fluid properties in order to close the system of equations.

In the next section the compressible Navier-Stokes equations are modified to make them suitable for the transmission line/inlet pipe analysis.

3.2.1 Continuity Equation

The mass conservation mass law applied to a fluid passing through a control volume yields the following equation of continuity:

$$\frac{\partial \rho}{\partial t} + \nabla \cdot \left(\rho \vec{V}\right) = 0 \tag{3.1}$$

where ρ is the fluid density and $\vec{V}$ is the fluid velocity vector. The first term in this equation represents the rate of increase of the density in the control volume, and the second term represents the rate of mass flux passing out of the control surface (which surrounds the control volume) per unit volume. The dot product operator $\nabla \cdot (\cdot)$ is the divergence and expressed as:

$$\nabla \cdot (\cdot) = \frac{\partial}{\partial x}(\cdot) + \frac{\partial}{\partial y}(\cdot) + \frac{\partial}{\partial z}(\cdot)$$

For a Cartesian coordinate system, where u, v, w represent the x, y, z components of the velocity vector, Equation (3.1) becomes:

$$\frac{\partial \rho}{\partial t} + \frac{\partial}{\partial x}(\rho u) + \frac{\partial}{\partial y}(\rho v) + \frac{\partial}{\partial z}(\rho w) = 0 \tag{3.2}$$

Note that this equation is in conservation law (divergence) form.

3.2.2 Momentum Equation

Newton's second law applied to a fluid passing through a control volume yields the following momentum equation:

$$\frac{\partial}{\partial t}(\rho\vec{V})+\nabla\cdot\rho\vec{V}\vec{V}=\sum\vec{F} \tag{3.3}$$

The first term on the left side in this equation represents the rate of increase of momentum per unit volume in the control volume. The second term represents the rate of momentum lost by convection (per unit volume) through the control surface. Note that $\rho\vec{V}\vec{V}$ is a tensor, so that $\nabla\cdot\rho\vec{V}\vec{V}$ is not a simple divergence. This term can be expanded, however, as:

$$\nabla\cdot\rho\vec{V}\vec{V}=\rho\vec{V}\cdot\nabla\vec{V}+\vec{V}(\nabla\cdot\rho\vec{V}) \tag{3.4}$$

The term on the right side of the Equation (3.3) means the sum of all forces acting in a given direction ($\vec{V}$ direction) on a control volume, which includes the body and surface forces on the fluid element. Then it is:

$$\sum\vec{F}=\rho\vec{f}+\nabla\cdot\prod_{ij} \tag{3.5}$$

The first term in right side of the Equation (3.5) is the body force vector per unit volume. Body forces act at a distance and apply to the entire mass of the fluid. The most common body force is the gravitational force. In the case, the force per unit mass ($\vec{f}$) equals the acceleration of gravity vector $\vec{g}$:

$$\rho\vec{f}=\rho\vec{g} \tag{3.6}$$

The second term on the right side of the Equation (3.5) represents the surface forces per unit volume. These forces are applied by the external stresses on the fluid element. The

stresses consist of normal stresses and shearing stresses and are represented by the components of the stress tensor $\prod_{ij}$.

When the Equations (3.4) and (3.5) are substituted into Equation (3.3), and the resulting equation is simplified using the continuity equation, the momentum equation reduces to:

$$\rho\frac{D\vec{V}}{Dt} = \rho\vec{f} + \nabla\cdot\prod_{ij} \tag{3.7}$$

Here, the substantial derivative is defined as:

$$\frac{D(\ )}{Dt} \equiv \frac{\partial(\ )}{\partial t} + \vec{V}\cdot\nabla(\ ) \tag{3.8}$$

The momentum equation given above is quite general and is applicable to both continuum and noncontinuum flows. If it is assumed that the stress at a point is linearly dependent on the rates of strain (deformation) of the fluid, which is called a Newtonian fluid, then a general deformation law that relates the stress tensor to the pressure and velocity components. In compact tensor notation, this relation becomes:

$$\prod_{ij} = -p\delta_{ij} + \mu\left(\frac{\partial u_i}{\partial x_j} + \frac{\partial u_j}{\partial x_i}\right) + \delta_{ij}\mu'\frac{\partial u_k}{\partial x_k} \quad i,j,k=1,2,3 \tag{3.9}$$

where δ_{ij} is the Kronecker delta function (δ_{ij}=1 if i=j and δ_{ij}=0 if $i\neq j$); u_1, u_2 and u_3 represent the three components of the velocity vector $\vec{V}$; x_1, x_2 and x_3 represent the three components of the position vector; μ is the coefficient of viscosity (dynamic viscosity), and μ' is the second coefficient of viscosity. The two coefficients of viscosity are related to the coefficient of bulk viscosity κ by the expression:

$$\kappa = \frac{2}{3}\mu + \mu' \tag{3.10}$$

If we ignore bulk viscosity and let κ is zero, the second coefficient of viscosity becomes:

$$\mu' = -\frac{2}{3}\mu \tag{3.11}$$

and the stress tensor may be written as:

$$\prod_{ij} = -p\delta_{ij} + \mu\left[\left(\frac{\partial u_i}{\partial x_j} + \frac{\partial u_j}{\partial x_i}\right) - \frac{2}{3}\delta_{ij}\frac{\partial u_k}{\partial x_k}\right] \quad i,j,k=1,2,3 \tag{3.12}$$

The stress tensor is frequently separated in the following manner:

$$\prod_{ij} = -p\delta_{ij} + \tau_{ij} \quad i,j,k=1,2,3 \tag{3.13}$$

where τ_{ij} represents the viscous stress tensor given by:

$$\tau_{ij} = \mu\left[\left(\frac{\partial u_i}{\partial x_j} + \frac{\partial u_j}{\partial x_i}\right) - \frac{2}{3}\delta_{ij}\frac{\partial u_k}{\partial x_k}\right] \quad i,j,k=1,2,3 \tag{3.14}$$

The suffices i and j in τ_{ij} indicate that the stress component acts in the j direction on a surface normal to the i direction, as shown in Figure 3.1.

Upon substituting Equation (3.12) into Equation (3.7), it is obtained:

$$\rho\frac{D\vec{V}}{Dt} = \rho\vec{f} - \nabla p + \frac{\partial}{\partial x_j}\left[\mu\left(\frac{\partial u_i}{\partial x_j} + \frac{\partial u_j}{\partial x_i}\right) - \frac{2}{3}\delta_{ij}\mu\frac{\partial u_k}{\partial x_k}\right] \tag{3.15}$$

For a Cartesian coordinate system, Equation (3.15) can be separated into the following three scalar Navier-Stokes equations:

$$\begin{cases} \rho\dfrac{Du}{dt} = \rho f_x - \dfrac{\partial p}{\partial x} + \dfrac{\partial}{\partial x}\left[\dfrac{2}{3}\mu\left(2\dfrac{\partial u}{\partial x} - \dfrac{\partial v}{\partial y} - \dfrac{\partial w}{\partial z}\right)\right] + \dfrac{\partial}{\partial y}\left[\mu\left(\dfrac{\partial u}{\partial y} + \dfrac{\partial v}{\partial x}\right)\right] + \dfrac{\partial}{\partial z}\left[\mu\left(\dfrac{\partial w}{\partial x} + \dfrac{\partial u}{\partial z}\right)\right] \\ \rho\dfrac{Dv}{dt} = \rho f_y - \dfrac{\partial p}{\partial y} + \dfrac{\partial}{\partial x}\left[\mu\left(\dfrac{\partial v}{\partial x} + \dfrac{\partial u}{\partial y}\right)\right] + \dfrac{\partial}{\partial y}\left[\dfrac{2}{3}\mu\left(2\dfrac{\partial v}{\partial y} - \dfrac{\partial u}{\partial x} - \dfrac{\partial w}{\partial z}\right)\right] + \dfrac{\partial}{\partial z}\left[\mu\left(\dfrac{\partial v}{\partial z} + \dfrac{\partial w}{\partial y}\right)\right] \\ \rho\dfrac{Dw}{dt} = \rho f_z - \dfrac{\partial p}{\partial z} + \dfrac{\partial}{\partial x}\left[\mu\left(\dfrac{\partial w}{\partial x} + \dfrac{\partial u}{\partial y}\right)\right] + \dfrac{\partial}{\partial y}\left[\mu\left(\dfrac{\partial v}{\partial z} + \dfrac{\partial w}{\partial y}\right)\right] + \dfrac{\partial}{\partial z}\left[\dfrac{2}{3}\mu\left(2\dfrac{\partial w}{\partial z} - \dfrac{\partial u}{\partial x} - \dfrac{\partial v}{\partial y}\right)\right] \end{cases} \tag{3.16}$$

Utilizing Equation (3.3), these equations can be rewritten in conservation law form as:

$$\begin{cases} \dfrac{\partial \rho u}{\partial t} + \dfrac{\partial}{\partial x}\left(\rho u^2 + p - \tau_{xx}\right) + \dfrac{\partial}{\partial y}\left(\rho uv - \tau_{xy}\right) + \dfrac{\partial}{\partial z}\left(\rho uw - \tau_{xz}\right) = \rho f_x \\ \dfrac{\partial \rho v}{\partial t} + \dfrac{\partial}{\partial x}\left(\rho uv - \tau_{xy}\right) + \dfrac{\partial}{\partial y}\left(\rho v^2 + p - \tau_{yy}\right) + \dfrac{\partial}{\partial z}\left(\rho vw - \tau_{yz}\right) = \rho f_y \\ \dfrac{\partial \rho w}{\partial t} + \dfrac{\partial}{\partial x}\left(\rho uw - \tau_{xz}\right) + \dfrac{\partial}{\partial y}\left(\rho uw - \tau_{yz}\right) + \dfrac{\partial}{\partial z}\left(\rho w^2 + p - \tau_{zz}\right) = \rho f_z \end{cases} \tag{3.17}$$

where the components of the viscous stress tensor τ_{ij} are given by:

$$\begin{cases} \tau_{xx} = \dfrac{2}{3}\mu\left(2\dfrac{\partial u}{\partial x} - \dfrac{\partial v}{\partial y} - \dfrac{\partial w}{\partial z}\right) \\ \tau_{yy} = \dfrac{2}{3}\mu\left(2\dfrac{\partial v}{\partial y} - \dfrac{\partial u}{\partial x} - \dfrac{\partial w}{\partial z}\right) \\ \tau_{zz} = \dfrac{2}{3}\mu\left(2\dfrac{\partial w}{\partial z} - \dfrac{\partial u}{\partial x} - \dfrac{\partial v}{\partial y}\right) \\ \tau_{xy} = \mu\left(\dfrac{\partial u}{\partial y} + \dfrac{\partial v}{\partial x}\right) = \tau_{yx} \\ \tau_{xz} = \mu\left(\dfrac{\partial w}{\partial x} + \dfrac{\partial u}{\partial z}\right) = \tau_{zx} \\ \tau_{yz} = \mu\left(\dfrac{\partial v}{\partial z} + \dfrac{\partial w}{\partial y}\right) = \tau_{zy} \end{cases} \tag{3.18}$$

Strictly speaking, the term Navier-Stokes equations refers to the components of the viscous momentum equation (Equation (3.15)). However, it is common practice to include the continuity equation and the energy equation in the set of equations referred to as the Navier-Stokes equations.

3.2.3 Energy Equation

The first law of thermodynamics applied to a fluid passing through a control volume yields the following energy equation:

$$\frac{\partial E_t}{\partial t} + \nabla \cdot E_t \vec{V} = \frac{\partial Q}{\partial t} - \nabla \cdot \vec{q} + \rho \vec{f} \cdot \vec{V} + \nabla \cdot \left(\prod_{ij} \cdot \vec{V} \right) \tag{3.19}$$

where E_t is the total energy per unit volume given by:

$$E_t = \rho \left(e + \frac{V^2}{2} + potential \quad energy + \cdots \right) \tag{3.20}$$

and e is the internal energy per unit mass. The first term on the left side of the Equation (3.19) represents the change rate of energy E_t in the control volume; while, the second term represents the rate of total energy lost by convection (per unit volume) through the control surface. The first term on the right side in the Equation (3.19) is the rate of heat produced per unit volume by external agencies; while the second term ($\nabla \cdot \vec{q}$) is the rate of heat lost by conduction (per unit volume) through the control surface. Fourier's law for heat transfer by conduction will be assumed, so that the heat transfer q can be expressed as:

$$\vec{q} = -k \nabla T \tag{3.21}$$

where k is the coefficient of thermal conductivity and T is the temperature. The third term on the right side in the Equation (3.19) represents the work done on the control volume (per unit volume) by the body forces; while the fourth term represents the work done on the control volume (per unit volume) by the surface forces. It should be obvious that Equation (3.19) is simply the First Law of Thermodynamics applied to the control volume. That is, the increase of energy in the system is equal to heat added to the system plus the work done on the system.

For a Cartesian coordinate system, Equation (3.19) becomes:

$$\frac{\partial E_t}{\partial t} - \frac{\partial Q}{\partial t} - \rho\left(f_x u + f_y v + f_z w\right) + \frac{\partial}{\partial x}\left(E_t u + pu - u\tau_{xx} - v\tau_{xy} - w\tau_{xz} + q_x\right) +$$
$$\frac{\partial}{\partial y}\left(E_t v + pv - u\tau_{xy} - v\tau_{yy} - w\tau_{yz} + q_y\right) + \frac{\partial}{\partial z}\left(E_t w + pw - u\tau_{xz} - v\tau_{yz} - w\tau_{zz} + q_z\right) = 0 \tag{3.22}$$

which is in conservation law form. Using the continuity equation, the left side in Equation (3.19) can be replaced by the following expression:

$$\rho \frac{D(E_t/\rho)}{Dt} = \frac{\partial E_t}{\partial t} + \nabla \cdot E_t \vec{V} \tag{3.23}$$

which is equivalent to:

$$\rho \frac{D(E_t/\rho)}{Dt} = \rho \frac{De}{Dt} + \rho \frac{D(V^2/2)}{Dt} \tag{3.24}$$

if only internal energy and kinetic energy are considered significant in Equation (3.20).

3.2.4 State Equation

In order to close the system of fluid dynamic equations, it is necessary to establish relations between the thermodynamic variables (p, ρ, T, and e). For example, consider a compressible flow without external heat addition or body forces and use Equation (3.2) for the continuity equation, Equation (3.17) for the three momentum equations, and Equation (3.22) for the energy equation. These five scalar equations contain seven unknown variables, p, ρ, T, e, u, v *and* w. It is obvious that two additional equations are required to close the system. These two additional equations can be obtained by determining relations that exist between the thermodynamic variables. Relations of this type are known as equations of state. The local thermodynamic state is fixed by any two

independent thermodynamic variables, provided that the chemical composition of the fluid is not changing owing to diffusion or finite-rate chemical reactions. Thus for the present example, if we choose e and ρ as the two independent variables, then the required state equations are:

$$\begin{cases} p = p(e, \rho) \\ T = T(e, \rho) \end{cases} \tag{3.25}$$

For most problems in gas dynamics, it is possible to assume a perfect gas. A perfect gas is defined as a gas whose intermolecular forces and there occupied volumes are negligible. A perfect gas obeys the perfect gas equation of state:

$$p = \rho RT \tag{3.26}$$

where R is the gas constant.

For problems involving a perfect gas at relatively low temperatures, it is possible to also assume a calorically perfect gas. A calorically perfect gas is defined as a perfect gas with constant specific heats. In a calorically perfect gas, the specific heat at constant volume C_v, the specific heat at constant pressure C_p, and the ratio of specific heats γ all remain constant, and the following relations exist:

$$\begin{cases} e = C_v T \\ \gamma = \dfrac{C_p}{C_v} \\ C_v = \dfrac{R}{\gamma - 1} \\ C_p = \dfrac{\gamma R}{\gamma - 1} \end{cases} \tag{3.27}$$

For air at standard conditions, R=287 $m^2/(s^2 \cdot K)$, C_p=1005.1 J/(Kg·K), C_v=717.9 J/(Kg·K), and γ=1.4 [71]. If it is assumed that the fluid in our example is a calorically perfect gas, then Equation (3.26) becomes:

$$\begin{cases} p = (\gamma - 1)\rho e \\ T = \dfrac{(\gamma - 1)e}{R} \end{cases} \tag{3.28}$$

3.2.5 Vector Form of Equations

Before applying a numerical algorithm to the governing fluid dynamic equations, it is often convenient to combine the equations into a compact vector form. For example, the compressible Navier-Stokes equations in Cartesian coordinates without body forces, mass diffusion, finite-rate chemical reaction, or external heat addition can be written as:

$$\frac{\partial \vec{U}}{\partial t} + \frac{\partial \vec{E}}{\partial x} + \frac{\partial \vec{F}}{\partial y} + \frac{\partial \vec{G}}{\partial z} = 0 \tag{3.29}$$

where $\vec{U}$, $\vec{E}$, $\vec{F}$, and $\vec{G}$ are vectors given by:

$$\vec{U} = \begin{bmatrix} \rho \\ \rho u \\ \rho v \\ \rho w \\ E_t \end{bmatrix}$$

$$\vec{E} = \begin{bmatrix} \rho u \\ \rho u^2 + p - \tau_{xx} \\ \rho uv - \tau_{xy} \\ \rho uw - \tau_{xz} \\ (E_t + p)u - u\tau_{xx} - v\tau_{xy} - w\tau_{xz} + q_x \end{bmatrix}$$

$$\vec{F} = \begin{bmatrix} \rho v \\ \rho uv - \tau_{xy} \\ \rho v^2 + p - \tau_{yy} \\ \rho vw - \tau_{yz} \\ (E_t + p)v - u\tau_{xy} - v\tau_{yy} - w\tau_{yz} + q_y \end{bmatrix}$$

$$\bar{G}=\begin{bmatrix} \rho w \\ \rho uw-\tau_{xz} \\ \rho vw-\tau_{yz} \\ \rho w^2+p-\tau_{zz} \\ (E_t+p)w-u\tau_{xz}-v\tau_{yz}-w\tau_{zz}+q_z \end{bmatrix} \tag{3.30}$$

The first row of the vector Equation (3.29) corresponds to the continuity equation as given by Equation (3.2). Likewise, the second, third, and fourth rows are the momentum equations, Equation (3.17), while the fifth row is the energy equation, Equation (3.22). In addition, the components of the shear-stress tensor and heat flux vector are given by Equations (3.18) and (3.21). With the Navier-Stokes equations written in this form, it is often easier to code the desired numerical algorithm.

3.2.6 Coordinate Conversion and Reducing Dimension

Here the inlet air flows in inlet pipes/transmission lines with circular cross-section are studied. It is necessary to convert the three-dimensional Navier-Stokes equations from Cartesian coordinates to cylindrical coordinates, in which the x, y and z components in Cartesian coordinates are replaced by r (radial), θ (circumferential) and z.

From the experiment (Figure 3.5), it is noticed that the change of the temperature for the pneumatic transmission line system is small enough to be omitted. The temperature is then assumed to be constant, although later when integrated with the combustion model this can leads to errors. Hence, the following coordinate conversion only focuses on the continuity and momentum equations.

In cylindrical coordinates, for continuity equation (Equation (3.2)), it becomes:

$$\frac{\partial \rho}{\partial t}+\frac{1}{r}\left[\frac{\partial}{\partial r}(r\rho u_r)+\frac{\partial}{\partial \theta}(\rho u_\theta)+\frac{\partial}{\partial z}(r\rho u_z)\right]=0 \tag{3.31}$$

and for momentum equations (Equation (3.17)), it is:

$$\begin{cases} \dfrac{\partial}{\partial t}(\rho u_r)+\rho\left(u_r\dfrac{\partial u_r}{\partial r}+\dfrac{u_\theta}{r}\dfrac{\partial u_r}{\partial \theta}+u_z\dfrac{\partial u_r}{\partial z}\right)+\dfrac{u_r}{r}\left[\dfrac{\partial}{\partial r}(r\rho u_r)+\dfrac{\partial}{\partial \theta}(\rho u_\theta)+\dfrac{\partial}{\partial z}(r\rho u_z)\right] \\ =\dfrac{1}{r}\left[\dfrac{\partial}{\partial r}(r\Pi_{rr})+\dfrac{\partial}{\partial \theta}(\Pi_{r\theta})+\dfrac{\partial}{\partial z}(r\Pi_{rz})\right] \\ \dfrac{\partial}{\partial t}(\rho u_\theta)+\rho\left(u_r\dfrac{\partial u_\theta}{\partial r}+\dfrac{u_\theta}{r}\dfrac{\partial u_\theta}{\partial \theta}+u_z\dfrac{\partial u_\theta}{\partial z}\right)+\dfrac{u_\theta}{r}\left[\dfrac{\partial}{\partial r}(r\rho u_r)+\dfrac{\partial}{\partial \theta}(\rho u_\theta)+\dfrac{\partial}{\partial z}(r\rho u_z)\right] \\ =\dfrac{1}{r}\left[\dfrac{\partial}{\partial r}(r\Pi_{r\theta})+\dfrac{\partial}{\partial \theta}(\Pi_{\theta\theta})+\dfrac{\partial}{\partial z}(r\Pi_{\theta z})\right] \\ \dfrac{\partial}{\partial t}(\rho u_z)+\rho\left(u_r\dfrac{\partial u_z}{\partial r}+\dfrac{u_\theta}{r}\dfrac{\partial u_z}{\partial \theta}+u_z\dfrac{\partial u_z}{\partial z}\right)+\dfrac{u_z}{r}\left[\dfrac{\partial}{\partial r}(r\rho u_r)+\dfrac{\partial}{\partial \theta}(\rho u_\theta)+\dfrac{\partial}{\partial z}(r\rho u_z)\right] \\ =\dfrac{1}{r}\left[\dfrac{\partial}{\partial r}(r\Pi_{rz})+\dfrac{\partial}{\partial \theta}(\Pi_{\theta z})+\dfrac{\partial}{\partial z}(r\Pi_{zz})\right] \end{cases} \tag{3.32}$$

where the stress tensor is given by:

$$\begin{cases} \Pi_{rr}=-p+\dfrac{2}{3}\mu(2e_{rr}-e_{\theta\theta}-e_{zz}) \\ \Pi_{\theta\theta}=-p+\dfrac{2}{3}\mu(2e_{\theta\theta}-e_{rr}-e_{zz}) \\ \Pi_{zz}=-p+\dfrac{2}{3}\mu(2e_{zz}-e_{rr}-e_{\theta\theta}) \\ \Pi_{\theta z}=\Pi_{z\theta}=\mu e_{\theta z} \\ \Pi_{rz}=\Pi_{zr}=\mu e_{rz} \\ \Pi_{r\theta}=\Pi_{\theta r}=\mu e_{r\theta} \end{cases} \tag{3.33}$$

and

$$\begin{cases} e_{rr}=\dfrac{\partial u_r}{\partial r} \\ e_{\theta\theta}=\dfrac{1}{r}\dfrac{\partial u_\theta}{\partial \theta} \\ e_{zz}=\dfrac{\partial u_z}{\partial z} \\ e_{\theta z}=\dfrac{1}{r}\dfrac{\partial u_z}{\partial \theta}+r\dfrac{\partial}{\partial z}\left(\dfrac{u_\theta}{r}\right) \\ e_{rz}=\dfrac{\partial u_r}{\partial z}+\dfrac{\partial u_z}{\partial r} \\ e_{r\theta}=r\dfrac{\partial}{\partial r}\left(\dfrac{u_\theta}{r}\right)+\dfrac{1}{r}\dfrac{\partial u_r}{\partial \theta} \end{cases} \tag{3.34}$$

The following then reduces the three-dimensional Navier-Stokes equations in cylindrical coordinate to one-dimension.

The first assumption is that the swirl of the fluid in each cross section is to be omitted. Then for continuity equation (Equation (3.31)) becomes:

$$\frac{\partial \rho}{\partial t}+\frac{1}{r}\left[\frac{\partial}{\partial r}(r\rho u_r)+\frac{\partial}{\partial z}(r\rho u_z)\right]=0 \tag{3.35}$$

and for momentum equations (Equation (3.32)), it is:

$$\begin{cases}\dfrac{\partial}{\partial t}(\rho u_r)+\rho\left(u_r\dfrac{\partial u_r}{\partial r}+u_z\dfrac{\partial u_r}{\partial z}\right)+\dfrac{u_r}{r}\left[\dfrac{\partial}{\partial r}(r\rho u_r)+\dfrac{\partial}{\partial z}(r\rho u_z)\right] \\ =\dfrac{1}{r}\left[\dfrac{\partial}{\partial r}(r\Pi_{rr})+\dfrac{\partial}{\partial z}(r\Pi_{rz})\right] \\ \dfrac{\partial}{\partial t}(\rho u_z)+\rho\left(u_r\dfrac{\partial u_z}{\partial r}+u_z\dfrac{\partial u_z}{\partial z}\right)+\dfrac{u_z}{r}\left[\dfrac{\partial}{\partial r}(r\rho u_r)+\dfrac{\partial}{\partial z}(r\rho u_z)\right] \\ =\dfrac{1}{r}\left[\dfrac{\partial}{\partial r}(r\Pi_{rz})+\dfrac{\partial}{\partial z}(r\Pi_{zz})\right]\end{cases} \tag{3.36}$$

where the stress tensor (Equations (3.33) and (3.34)) is given by:

$$\begin{cases}\Pi_{rr}=-p+\dfrac{2}{3}\mu(2e_{rr}-e_{zz}) \\ \Pi_{zz}=-p+\dfrac{2}{3}\mu(2e_{zz}-e_{rr}) \\ \Pi_{rz}=\Pi_{zr}=\mu e_{rz}\end{cases} \tag{3.37}$$

and

$$\begin{cases}e_{rr}=\dfrac{\partial u_r}{\partial r} \\ e_{zz}=\dfrac{\partial u_z}{\partial z} \\ e_{rz}=\dfrac{\partial u_r}{\partial z}+\dfrac{\partial u_z}{\partial r}\end{cases} \tag{3.38}$$

Further assumption is that the fluid along the radial direction is of uniform profile. Then for continuity equation (Equation (3.35)), it is:

$$\frac{\partial \rho}{\partial t}+\frac{\partial}{\partial z}(\rho u_z)=0 \tag{3.39}$$

and for momentum equations (Equation (3.36)), it is:

$$\frac{\partial}{\partial t}(\rho u_z)+\rho u_z \frac{\partial u_z}{\partial z}+u_z \frac{\partial}{\partial z}(\rho u_z)=\frac{\partial}{\partial z}(\Pi_{zz}) \tag{3.40}$$

where the stress tensor (Equations (3.37) and (3.38)) is given by:

$$\Pi_{zz}=-p+\frac{4}{3}\mu e_{zz} \tag{3.41}$$

and

$$e_{zz}=\frac{\partial u_z}{\partial z} \tag{3.42}$$

Up to here, the one-dimensional partial differential equations for the inlet pipe/transmission line with circular cross-section have been derived. They will then be used in the following simulations to capture the dynamics of pressure waves inside the transmission line. Two applications are considered: 1) both-end blocked model; and 2) volume charging. Before staring the simulation, the relevant experiments are needed firstly to calibrate some parameters. In the following sessions, the available test-rigs used for obtaining required experimental data are described.

3.3 EXPERIMENTS

In this section, the experimental setup is described. Real time experimental data is captured. Several parameters are calibrated which will be used in the following simulations.

3.3.1 Test Rig and Its Components

In this study, two experimental setups are configured. The first one is for the completely blocked model, and the second one is for the model of volume air charging linked with a transmission line/inlet pipe.

Figure 3.2 shows the experimental setup for the both-end blocked configuration. The tube from the compressed air supply is linked with a solenoid directional valve, which is then connected with one end of the polyurethane line. The other end of this transmission line is linked back to the directional valve and then exhausted to the atmosphere. During the experiment, the directional valve is opened to make the air flow through the line. When the steady state is reached, the valve is closed to make the air trapped within the transmission line. The pressure transducers are embedded into the transmission line to measure the pressure during the whole process. One mass flow meter is put between the air supply and the valve to obtain the steady state mass flow rate. All these data are recorded by a data acquisition card, which is incorporated into a PC.

Figure 3.3 shows the experiment setup for volume charging with a transmission line/inlet pipe. The pipe from the compressed air supply is still linked with a solenoid directional valve, which is then connected with one end of the line. The other end of this line is linked with a large volume. Here this large volume is a cylinder. When the valve is opened, the compressed air will start to charge the cylinder through the line, which will be completed when the pressure of the whole system uniform. The pressure transducers are used to capture the pressure signals.

Summarizing the experimental setups above, the following components are used in this study, which are:

1) *Valve.* An SMC 3-position-closed-centre solenoid directional valve (SY7340-5DZ-Q) is used to regulate the air flow. This valve has an operating voltage of 24 Volts DC and has a maximum operating pressure of 7 bar.

2) *Pressure Transducer.* Festo pressure transducers (PENV-A-PS/O-LCD) are used to capture the instantaneous pressure signal within the different positions of the transmission line, which have a measuring range of 0-12 bar with operating voltage of 24 Volts DC.

3) *Mass Flow Meter.* IFM mass flow meter (SD6000) is used to measure the steady state mass flow rate for the first experimental setup (Figure 3.2). This flow meter has a maximum operating pressure of 16 bar with operating voltage of 24 Volts DC. From the IFM manual, the actual mass flow rate is equal to the recorded (displayed) flow meter value multiplied by the air density at zero sea-level.

4) *Cylinder.* A double-rod-double-acting pneumatic cylinder (C92SB-125-180W) with a bore of 125 mm and a stroke of 180 mm is used as the large volume at the end to let the compressed air charge it through the transmission line. The calculated inner volume of this cylinder is about 0.002 m^3.

5) *Data Acquisition Card.* The Microstar Laboratories DAP 4200a is used to sample measured data from the transducers, flow meter, etc, and send the relevant control signals to valve, pressure regulator, etc. This DAP has a high sampling time of 100 ns with both input and output range of ±10 Volts DC.

Other components used in this study are:

1) *Pressure Regulator.* SMC pressure regulator (ITV2030-31) is used to regulate the supplied air pressure from the main line. It has a maximum working pressure 5 bar with operating voltage of 24 Volts DC.

2) *Thermocouple*. Rod type-T thermocouples are used to measure the temperature inside of the transmission line.

Firstly, these components will be used to calibrate the line diameter. Then the temperature is measured inside of the transmission line with the thermocouples to give evidence why the following simulation assumes that temperature is constant for the whole system.

3.3.2 Transmission Line Diameter Calibration

The polyurethane pneumatic tube with inner diameter 5 mm and wall thickness 1.5 mm is used as the transmission line. Due to the compressible characteristics of this polyurethane tube, the diameter meter needs to be first calibrated by experiment to determine the influence of the system pressure on the changes in its radial dimension. Highly incompressible liquid (such as water) is injected into a polyurethane transmission line which is blocked at one end. Different pressures are then applied to the other end. By recording the liquid height, the transmission line diameter changes can be determined. Experiment results are listed in Table 1.

It is assumed that the high pressure applied only expands the transmission line along the radial direction and do not influence the dimension along the axial direction. The initial volume occupied by the water is $1.88\times10^{-6}\,\mathrm{m}^3$. Based on the assumption above, the relationship between the applied pressure and the expanded internal diameter of the transmission line is shown in Figure 3.4.

The relationship between the transmission line diameter and the applied pressure is shown in Equation (3.43).

$$d = 3\times10^{-5}\,p + 0.005 \tag{3.43}$$

Equation (3.43) expresses the static relationship between the inner diameter of the polyurethane pneumatic transmission line and the corresponding pressure. This equation

will be used in the following simulation to consider the inner diameter changes of the tube due to the high pressure. However, since the polyurethane tube is elastic material, it can not immediately follow the changes of the pressure. Dynamics may need to be considered later.

3.3.3 Kinematic Viscosity Calibration

Viscosity is a measure of a fluid's resistance to flow. Low viscosity fluids such as the air used in this study tend to promote high levels of leakage loss in equipment. On the other hand, high viscosity fluids result in more sluggish operation and power wastage due to excessive pressure loss through pipe lines and components [77].

The dynamic viscosity (μ Ns/m^2) of a fluid is defined as [52]:

$$\mu = \frac{shear \quad stress}{shear \quad rate} = \rho v \tag{3.44}$$

where v is the kinematic viscosity (v m^2/s) and it is the ratio of the dynamic viscosity to the fluid density. The typical value of the kinematic viscosity for air is 1.5×10^{-5} m^2/s at 1 bar and 20 degree C, which expresses the resistance between air and air.

Before the simulation is conducted, the average kinematic viscosity between air and the polyurethane tube needs to be firstly determined and this is done by utilising the equation of the pressure drop along a pipe segment, which is shown as [54]:

$$\Delta p = \frac{128 \dot{M}_d l v}{\pi d^4} \tag{3.45}$$

Note that Δp is the pressure drop along a pipe segment, l is the segment length, and $\dot{M}_d$ is the mass flow rate.

As shown in Figure 3.2, the valve is opened until the steady state is reached. The pressure signals and mass flow rate are recorded by the DAP card, Table 3.2. Based on these measured data and using Equation (3.45), the kinematic viscosity v is identified as 0.00011 m^2/s.

3.3.4 Temperature Measurement

The experimental setup shown in Figure 3.2 is used for temperature measurement of the line, where the pressure transducers are replaced by rod type-T thermocouples.

The valve is first opened until the line reaches a steady state. Then it is closed to block both end of the line. Five type-T thermocouples are used to record the temperature corresponding to the five different positions until the fluid trapped inside reaches a new steady state. The experimental results are shown in Figure 3.5, from which it is noticed that there are no significant temperature variations during this period. Hence, it is assumed the temperature is constant for the following simulation, although later this becomes subject to doubt in this thesis.

3.4 LINE SIMULATION

Here, the dynamics of the air flow in the polyurethane line are simulated. The lumped line model [52, 64] is firstly analyzed to prove its practibility for expressing the pressure wave dynamics in the pipe. The numerical discretisation method is then selected to obtain the finite difference formation for the continuity and momentum equations (Equations (3.39) and (3.40)). Two experimental setups are designed. The relevant pressure and mass flow rate are captured by the DAP card, which is then stored in the PC. The method of combining the finite difference model with the lumped model is proposed. The simulation results show the validity of this combined model for the experimental results obtained.

3.4.1 Lumped Line Model

The variable orifice is the most popular device for controlling fluid flow, which is the fluid equivalence of the electrical resistor. Andersen [78] and Blackburn et al [79] give a detailed description of the flow of gases through orifices. For air as a working fluid, compressibility is an important factor. Mass rather than volume flow rate is generally used, since in the case of compressible flow, volume and pressure are interdependent. The mass flow rate $\dot{M}_d$ through an orifice can be written as [52]:

$$\dot{M}_d = C_d \cdot C_m \cdot A \cdot P_u / \sqrt{T_u} \tag{3.46}$$

where C_d is the discharge coefficient, P_u is the upstream stagnation pressure (absolute), A is the orifice area, and T_u is the upstream stagnation temperature (absolute).

The mass flow parameter C_m is shown below in Equation (3.47).

$$C_m = \sqrt{\frac{2\gamma}{R(\gamma-1)}\left[\left(\frac{P_{vc}}{P_u}\right)^{2/\gamma} - \left(\frac{P_{vc}}{P_u}\right)^{(\gamma+1)/\gamma}\right]} \tag{3.47}$$

where P_{vc} is the static pressure at the vena contracta or throat, R is the gas constant (287 $m^2/(s^2 \cdot K)$ for air), and γ is the ratio of the specific heat (1.4 for air).

Equation (3.47) applies only when:

$$\frac{P_{vc}}{P_u} > \left(\frac{2}{\gamma+1}\right)^{\lambda/(\gamma-1)} = 0.528 \quad \text{for air.}$$

When P_{vc}/P_u is less than this value, the flow is to be choked and C_m becomes:

$$C_m = \left(\frac{2}{\gamma+1}\right)^{1/(\gamma-1)} \sqrt{\frac{2\gamma}{R(\gamma+1)}} = 0.0405 \qquad \text{for air.} \tag{3.48}$$

The variation of C_m with pressure ration is shown in Figure 3.6.

It is impossible with the current experimental components to measure the pressure value at the vena contracta, which is assumed to be the one downstream of the orifice. In addition, the discharge coefficient C_d is a function of Reynolds number and orifice geometry. In general, the discharge coefficient of an orifice is determined experimentally.

For the line shown in Figure 3.2 or Figure 3.3, if it is equally divided into N segments and the orifice equation (Equation (3.46)) is used to calculated the mass flow rates at the inlet and outlet of each segment, then it forms the foundation of a lumped model. In this study, the transmission line has a cross-sectional diameter 5 mm with 1.5 mm wall thickness. Using the test rig in Figure 3.3, the lumped analogy of the system is presented in Figure 3.7. The valve is initially closed, and then the pressures within the transmission line and the last large volume are all ambient. Once the valve is opened, the compressed air from the air supply with constant pressure P_s is used to charge this line and the large volume through the orifices with the same diameters until the pressures in each segment are same as the one from the air supply. The validation of this lumped model had been demonstrated by Xue and Yusop [64].

Equation (3.46) is firstly used to calculate the mass flow rate through an orifice, which is then used in the following two differential equations to update the mass and pressure in each segment. Here, the temperature is assumed to be constant.

For continuity equation, it is:

$$\frac{dm_i}{dt} = \dot{M}_i - \dot{M}_{i+1} \tag{3.49}$$

and for state equation, it is:

$$\frac{dp_i}{dt} = \frac{RT}{V_i}\left(\dot{M}_i - \dot{M}_{i+1}\right) \tag{3.50}$$

where the m_i is the mass in segment i, $\dot{M}_i$ is the mass flow rate flowing into the segment i, $\dot{M}_{i+1}$ is the mass flow rate flowing out of the segment i (which is equal to the mass flow rate flowing into the next segment $i+1$), p_i is the pressure at the segment i, and the V_i is the volume of the segment i.

3.4.2 Finite Difference Model

In the finite difference approach, the continuous problem domain is "discretized", so that the dependent variables are considered to exist only at discrete points. Derivatives are approximated by differences, resulting in an algebraic representation of the partial differential equation. Thus a problem involving calculus has been transformed into an algebraic problem [80].

There are many numerical discrete methods, which include Upwind Method [31], Lax-Wendroff Method [81, 82], MacCormack Method [83, 84], etc. According to the analysis of inviscid Burgers' Equation, the Upwind Method is used to discrete the continuity equation (Equation (3.39)) and momentum equation (Equation (3.40)) in this study.

When the velocity of the main flow is positive, the backward upwind differencing formation is as follows:

for continuity equation:

$$\rho_i^{n+1} = \rho_i^n - \frac{\Delta t}{\Delta x}\left((\rho u_x)_i^n - (\rho u_x)_{i-1}^n\right) \tag{3.51}$$

and for momentum equation:

$$(\rho u_x)_i^{n+1} = (\rho u_x)_i^n - \frac{\Delta t}{\Delta x}\left((\rho u_x^2 + p)_i^n - (\rho u_x^2 + p)_{i-1}^n - \frac{1}{\Delta x}\left(\frac{4}{3}\mu_i^n\left(\frac{u_{i+1}^n - u_i^n}{\Delta x}\right) - \frac{4}{3}\mu_{i-1}^n\left(\frac{u_i^n - u_{i-1}^n}{\Delta x}\right)\right)\right) \quad (3.52)$$

When the velocity of the main flow is negative, the forward upwind differencing formation is as follows:

for continuity equation:

$$\rho_i^{n+1} = \rho_i^n - \frac{\Delta t}{\Delta x}\left((\rho u_x)_{i+1}^n - (\rho u_x)_i^n\right) \quad (3.53)$$

and for momentum equation:

$$(\rho u_x)_i^{n+1} = (\rho u_x)_i^n - \frac{\Delta t}{\Delta x}\left((\rho u_x^2 + p)_{i+1}^n - (\rho u_x^2 + p)_i^n - \frac{1}{\Delta x}\left(\frac{4}{3}\mu_{i+1}^n\left(\frac{u_{i+1}^n - u_i^n}{\Delta x}\right) - \frac{4}{3}\mu_i^n\left(\frac{u_i^n - u_{i-1}^n}{\Delta x}\right)\right)\right) \quad (3.54)$$

where the prefix n is the time level, the suffix i is the spatial level in x direction, Δt is the time interval, and Δx is the spatial interval in x direction.

The Upwind Method gives second order accuracy. The different difference formations are applied to ensure a stable numerical scheme due to the main flow velocity, which means that the errors from any source (truncation, round-off and discretization errors) are not permitted to grow in the sequence of numerical procedures as the calculation proceeds from one marching step to the next.

If the Equations (3.39) and (3.40) are combined into a compact vector form, then it is:

$$\frac{\partial \vec{U}}{\partial t}+\frac{\partial \vec{E}}{\partial t}=0 \tag{3.55}$$

where $\vec{U}$ and $\vec{E}$ are vectors given by:

$$\vec{U}=\begin{bmatrix}\rho\\ \rho u\end{bmatrix} \tag{3.56}$$

$$\vec{E}=\begin{bmatrix}\rho u\\ \rho u^2+p-\tau_{xx}\end{bmatrix} \tag{3.57}$$

and the components of the shear-stress τ_{xx} is given by:

$$\tau_{xx}=\frac{4}{3}\mu\frac{\partial u}{\partial x} \tag{3.58}$$

After each iteration, the primitive variables, which are density ρ, velocity u, mass flow rate $\dot{M}$, dynamics viscosity μ, and pressure p, can be found be "decoding" the $\vec{U}$ vector,

$$\vec{U}=\begin{bmatrix}\rho\\ \rho u\end{bmatrix}=\begin{bmatrix}U_1\\ U_2\end{bmatrix} \tag{3.59}$$

in the following manner:

$$\begin{cases}\rho=U_1\\ u=\dfrac{U_2}{U_1}\\ \dot{M}=U_2A\\ \mu=U_1\nu\end{cases} \tag{3.60}$$

where A is the cross-section area of the transmission line. The last primitive variable p is calculated by Equation (3.50), which is to eliminate the bias due to the one-sided differencing. In addition, the prefect gas law and constant temperature are assumed.

3.4.3 Pressure Wave Simulation for Both-end Blocked Line Model

Figure 3.2 shows the experimental setup for both-end blocked polyurethane air transmission line, which has the internal diameter of 5mm and a wall thickness 1.5mm. An IFM flow meter is installed in front of a SMC 3-position-closed-center solenoid directional valve. Five Festo pressure transducers are equally spaced within the transmission line to measure dynamic pressure signals during the experiment. The compressed air is supplied from a central air station, which is far away from the experimental setup. Its steady state pressure is around 7 bar.

During the experiment, the valve is first opened to allow the air flow into the transmission line. The other end of the transmission line is linked back to the valve and then exhausts to the atmosphere. When the air flow in the transmission line reaches the steady state, the valve is discharged and the spool moves to the closed-centre to block both ends of the transmission line. Then the trapped air inside of the line will travel back and forth due to the different pressure and momentum in each position. Through the mass mixture of the air, the collision between the atoms or molecules, and the friction due to the viscosity etc, the flow within the line will reach a new steady state, in which the flow is static (actually the velocity of flow is zero) and the pressure is the same for different positions. Five pressure transducers are used to record pressures corresponding to the four segments during the whole process, and a mass flow meter is used to record air mass flow rate under the steady state condition before the valve is discharged. The recorded steady state values from these experimental components are then used as the initial conditions for the simulation. The transient pressure values are recorded to compare with the simulation results.

Figure 3.8 shows the measured experimental data. The line is equally divided into four segments with 1 m each. When the air flow reaches the steady state after the valve is

opened, the recorded pressure and mass flow rate are listed in Table 3.3, which will be used as the initial conditions for the following simulation.

The lumped model is firstly used to simulate the pressure wave shown in Figure 3.8. From the description in Section 3.4.1, it is obvious that the computation time for lumped model must be quick due to the simple equations used. Hence, the lumped model is less sensitive to the sampling time and spatial distribution. Figure 3.9 shows the simulation results from the lumped model. It is obvious that the lumped model is failing to simulate the travelling pressure wave inside of the transmission line. However, the steady state valve is coincident with the measured data, which is about 4.5 bar (absolute).

The orifice equation (Equation (3.46)) is the foundation of the lumped model, from which it is noticed that the mass flow is forced to flow in one direction. It means that only when the value P_{vc}/P_u is less than 1, the calculated mass flow $\dot{M}_d$ rate is not zero. Otherwise, the value of $\dot{M}_d$ would be zero, which gives no changes for continuity and state equations (Equation (3.49) and (3.50)). Due to this, all simulated pressure will directly converge to steady state values and it is impossible to capture the pressure wave ripples.

One-dimensional compressible Navier-Stokes equations (Equations (3.39) and (3.40)) are then selected to simulate this pressure wave ripple. The primitive variables at the first and last segments, which are density ρ, velocity u, mass flow rate $\dot{M}$, dynamic viscosity μ, and pressure p, are the boundary conditions for the finite difference equations (Equations (3.51)-(3.54)), which are known parameters before each iteration. However, the primitive variables for these two segments are variant. Hence the relevant methods must be considered to update the boundary conditions. Since the lumped model has the capability to simulate the steady state pressure values of the experimental setup Figure 3.2, the combination of the finite difference model with the lumped model is proposed in this study. The lumped model is used to update the primitive variables in the first and the last segments, while the finite difference model is used to simulate the primitive variables in the other segments.

The change of temperature is not considered in this study and the temperature is assumed to be constant at an ambient temperature of 20°C. The influence of the high pressure on the transmission line diameter (Equation (3.43)) is included in the simulation.

The simulation is described by the flow chart, Figure 3.10. When starting the simulation, the steady state pressures and mass flow rate recorded by pressure transducers and mass flow meter before the valve is closed to block both end of the polyurethane transmission line are used as the initial conditions. The orifice equation (Equation (3.46)) firstly calculates the mass flow rate passing the first segment. Then the main flow velocity is assessed. When it is positive, the backward upwind differencing formulations (Equations (3.51) and (3.52)) are used to calculate the density and velocity in segment i; when it is negative, the forward upwind differencing formations (Equation (3.53) and (3.54)) are used. After that, the orifice equation (3.46) is used again to calculate the mass flow rate entering into the last segment. After updating the parameters in all segments, the condition to reach the new steady state is judged to determine whether the simulation is completed or not.

Based on this combined model, comparisons between simulation and experiment results are as shown in Figure 3.11. Note that the pressure travelling waves are correctly present in the computer simulation results. Especially, the simulation results matches well for the pressure ripple frequency compared with the experimental data. However, the simulation shows the longer transient state process, which might be because a perfect gas is assumed during the simulation. For the real gas, the existence of the atoms and molecules will induce extra the kinetic energy loss due to the collision between these substances and the energy loss due to the friction between them. The direct result of energy loss is to diminish the pressure ripples quicker than the simulation results. Figure 3.12 shows the comparison of one pressure ripple between the experimental and simulation results.

3.4.4 Pressure Wave Simulation for Charging a Large Volume Linked with a Transmission Line

Figure 3.3 shows the experimental setup for charging a large volume linked with a polyurethane air transmission line. The internal diameter is still 5mm with a wall thickness 1.5mm. One end of the transmission line is connected with a SMC 3-position-closed-center solenoid directional valve connects. The other end is linked with a large volume, which is the pneumatic cylinder in this study. Three Festo pressure transducers are used to measure dynamic pressure signals during the experiment, one of which is located just before the inlet port of the pneumatic cylinder to approximately measure the pressure inside of the cylinder.

A large volume is linked with a 2.8 m polyurethane pneumatic transmission line. Before the valve is opened, the pressure in the transmission line and the large volume is ambient. After the valve is opened, the compressed air from the air supply will charge the transmission line and large volume until the whole system reaches the steady state. Then the pressure in each position of the whole system is equal to the one from the air supply, which is about 7.25 bar. Pressure transducers in positions i, j and k were used to record the pressure during this process. Here, the temperature for the whole system was assumed to be constant and the change of the transmission line diameter due to the high pressure is still considered during the simulation as before.

Figure 3.13 shows the measured experimental data. The transmission line is equally divided into four segments with 0.7 m each. Once the valve is opened, the pressure at different positions is captured to record the process of charging the large volume.

The lumped model is firstly used to simulate the air charging the large volume with the line in Figure 3.13. Figure 3.14 shows the simulation results from the lumped model. Compared with the simulation results in Figure 3.9, the lumped model here shows better simulation when the main fluid only goes in one direction.

The proposed finite difference model combined with lumped model is now used for the

model of air charging a large volume linked with an inlet pipe/transmission line. The simulation results in Figure 3.15 show that the proposed combination model gives better matching with the experimental data. It gives more accurate transient state and smaller transient errors than those from the lumped model simulation.

3.5 DISCUSSION AND CONCLUSIONS

The transmission line diameter calibration experiment shows that the relationship between the diameter and the exerted pressure is close to linear, which is then applied to the simulation algorithm to derive the influence of the working pressure on the transmission line diameter expansion as shown in Figure 3.4.

Figure 3.8 shows the pressure response in the transmission line after the valve blocks both end of the transmission line. When the valve is fully closed, the air will continue to flow downstream within the transmission line due to the presence of higher pressure and momentum at the upstream. Therefore the pressure downstream of the transmission line will continue to increase until it reaches a peak value at which the velocity downstream is close to zero. The fluid then starts to flow in the opposite direction in the transmission line since the pressure downstream is larger than the pressure upstream. When the upstream pressure reaches a new peak value, the fluid flows downstream again. This process repeats itself though the peak pressure values reached at different transmission line positions with passage of time will gradually decreases due to the viscosity effect imposed on the travelling air and the mixing of the fluid. The system finally reaches a new steady state in which all the pressures along the transmission line arrive at the same constant value.

A combined transmission line model is proposed and developed. The simulation is based on the combination of a finite difference model (Equations (3.49) and (3.50)) and a lumped model (Equation (3.46)). The lumped model is used to update the boundary conditions, which is then applied to the first and the last segments. For the completely blocked line simulation, this last segment is part of the polyurethane pneumatic tube itself (Figure 3.2); while for the simulation of charging a large volume with transmission line, this last segment is the cylinder (Figure 3.3). The parameters for the other segments are updated by means of finite difference model in the simulation algorithm.

Simulation results based on the proposed combination model show good consistency compared with the experiment data especially in the pressure frequency response.

1) For both-end blocked model, the lumped model fails to represent the pressure travelling along the transmission line. As the foundation of the lumped model, the orifice equation (Equation (3.46)) always forces the mass flow along one direction. The calculated mass flow $\dot{M}_d$ rate would be zero if the value P_{vc}/P_u is larger than 1, which means that there are no changes for continuity and state equations (Equation (3.49) and (3.50)). Due to this, all simulated pressures will directly converge to steady state values and it will be impossible to capture the pressure wave ripples. However, the lumped model gives the right steady state pressure values, which indicates that the lumped model could be used as one part of the total model. The finite difference model eliminates this limitation and is able to model the pressure wave for different directions. For both-end blocked models, the boundary conditions are variant, hence certain methodologies must be taken to update them before each iteration. In this study, the combined model is proposed, in which the lumped model is used to update boundary conditions and the finite difference model is used to update the primitive variables for the rest of the segments. The simulation results show good consistency compared with the experiment data, especially in the pressure frequency response. It is also noticed that the air in the transmission line takes a longer time to reach a new steady state compared with the experiment results as shown in Figure 3.11. This is due to the fact that perfect gas is assumed. Perfect gas assumes that the force between the atoms or molecules and the volume occupied by them in the gas are negligible. Under real gas conditions, due to the existence of the aforementioned factors, the influence of friction on the working fluid must be greater. This affects the gas kinetic energy and results in an earlier dissipation of the pressure wave in the captured data compared to the simulated results.

2) For the model of charging a cylinder with the transmission line, both lumped model and the proposed combination model are as shown in Figures 3.14 and Figures 3.15. They all give good representations of the trends of the pressure wave. The proposed combination model gives more accurate transient state and smaller transient errors than that from the lumped model simulation. In addition, due to the limitation of the test rig

itself, it is impossible to directly measure the pressure inside of the cylinder. The pressure transducer (P_k in Figure 3.3) is directly linked with the cylinder inlet port by a short polyurethane pneumatic tube. When the compressed air with high pressure reaches this short tube and then starts to charge the cylinder, the velocity of the fluid within this short tube will suddenly be changed from zero to a large value, the fluid then being released into the large volume cylinder. This short tube will act like a vena contracta to stop the fluid entering into the cylinder when the velocity inside of it is suddenly changes. Hence, there is a small bumped part in experimental curve as shown in Figure 3.15 (c).

From the experiment, it is shown that the transmission line has a very significant influence on the whole system dynamics in these experiments. Hence, a valid mathematical model and method should be considered to represent the pressure wave in it. Here a time domain model describing the dynamics of air in an inlet pipe/transmission line is presented by considering changes in air density, pressure and mass flow rate and assuming the temperature to be constant. A combined model is proposed to simulate the dynamics of trapped air in a blocked line and the charging of a large volume with the transmission line. In order to update the boundary conditions, the first and the last segments are considered as two lumped volumes and these are then connected to the transmission line segments using a lumped model. The rest of the line segments are expressed by means of a finite difference model. The effectiveness of the proposed model is depicted through comparisons of simulated pressure responses against pressures measured by practical experiments. The simulated results can thus be considered to be successful since it does match well with the captured experimental data though the simulated results show longer system transient state for both-end blocked model. In terms of application to the combustor model some further problems are thrown up for discussion later. In addition, it is found that variations of the kinematic viscosity scarcely affect the simulation results. Hence, the kinematic viscosity is assumed to be constant in the following research.

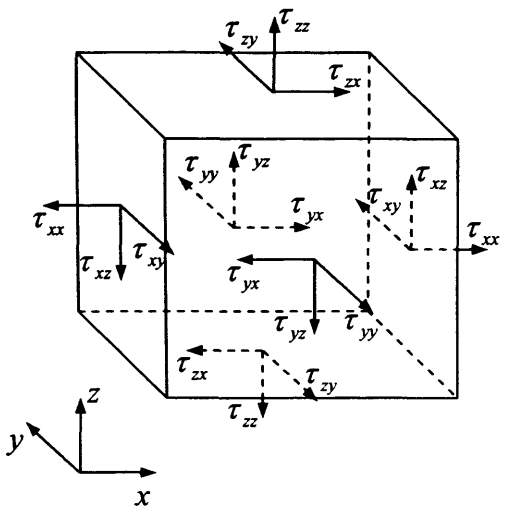

Figure 3.1: Stress Components on Three Faces of Fluid Element

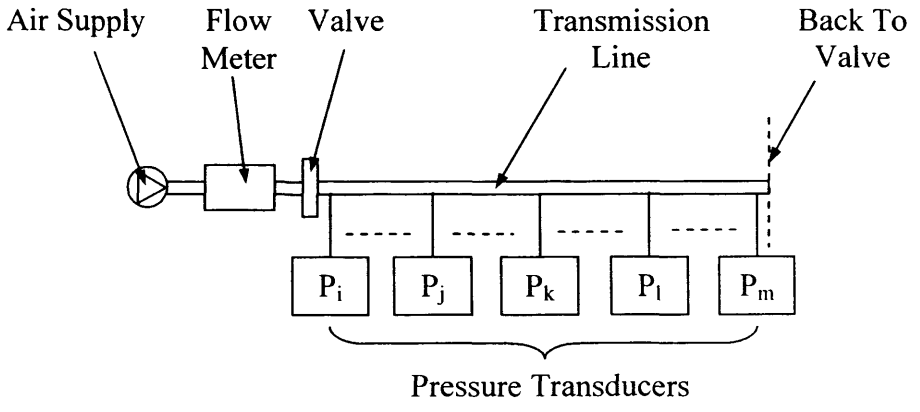

Figure 3.2: Experiment Setup for Both-end Blocked Air Transmission Line

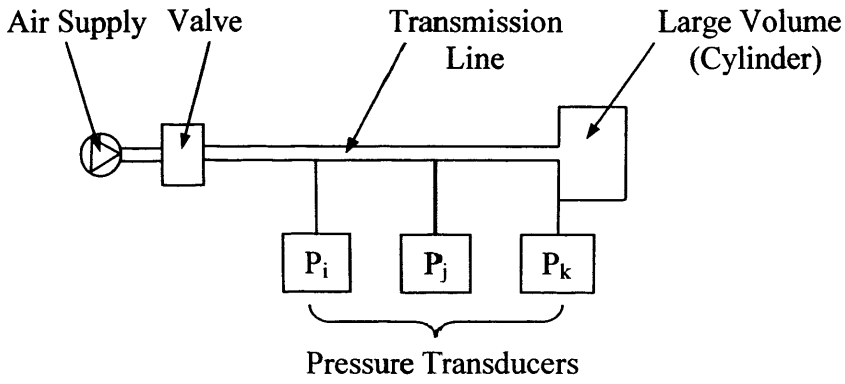

Figure 3.3: Experiment Setup for Air Charging a Large Volume (Cylinder) with Transmission Line

Table 3.1: Transmission Line Diameter Calibrations

Pressure [bar]	Liquid Height[mm]
0	95.82
1	94.46
2	93.72
3	92.32
4	91.59
5	90.85
6	89.27
7	88.37

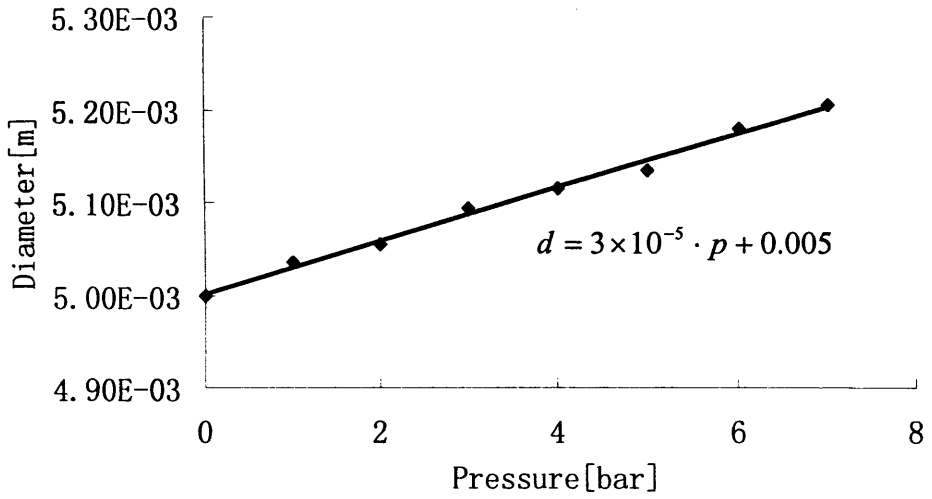

Figure 3.4: Transmission Line Diameter Calibrations

Table 3.2: Recorded Values by DAP Card for Kinematic Viscosity Calibration

Components		Values
Pressure Transducer (Absolute) [bar]	P_i	2.44
	P_j	2.27
	P_k	2.09
	P_l	1.86
	P_m	1.68
Mass Flow Meter [Kg/s]		0.0065
Segment Length [m]		0.34

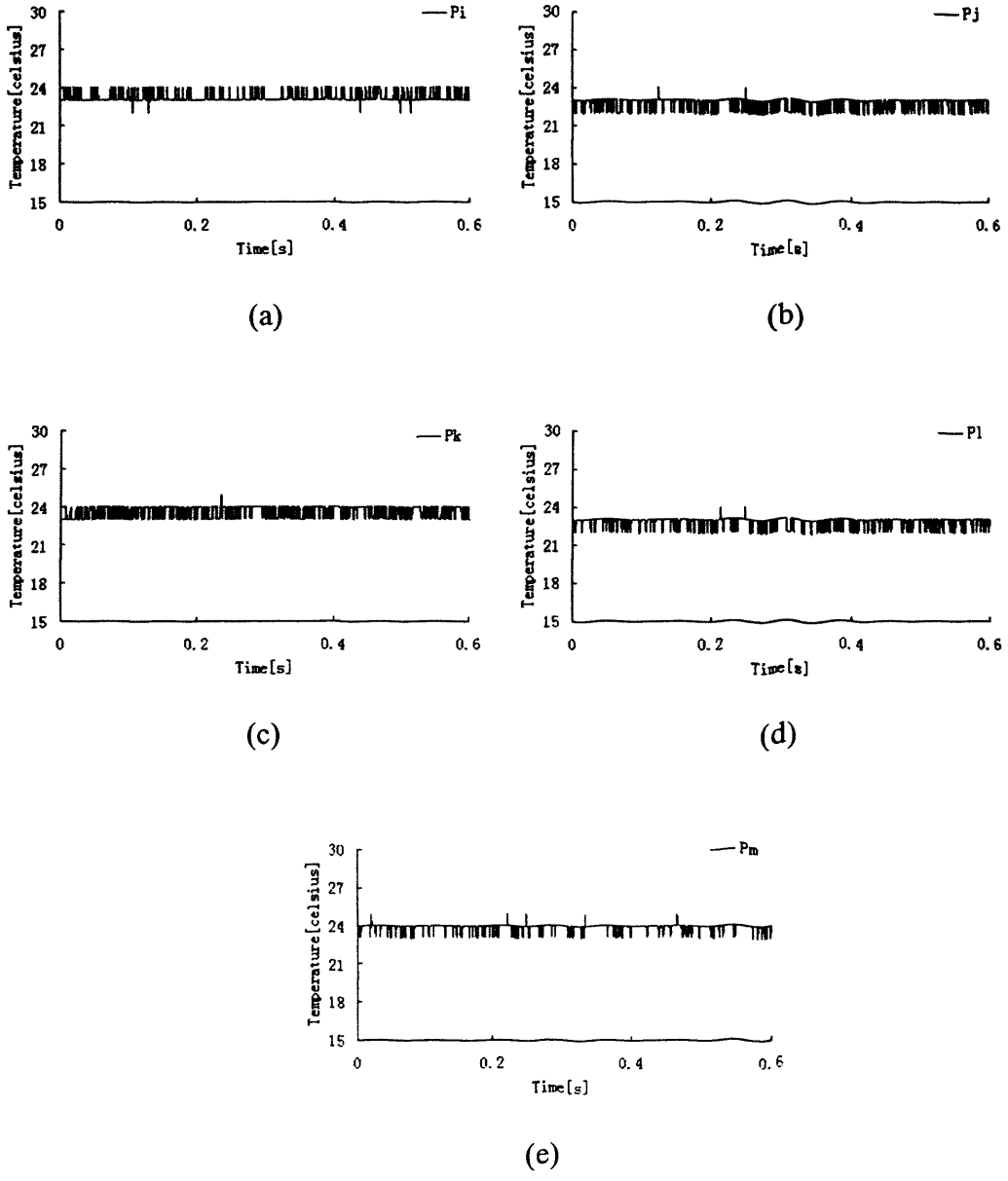

Figure 3.5: Temperature Measurement of Transmission Line

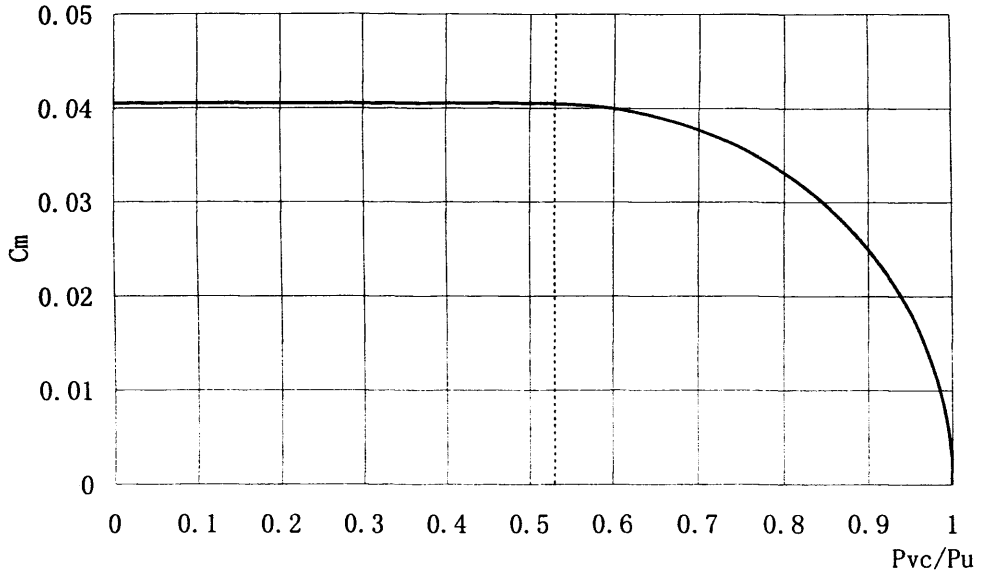

Figure 3.6: Variation of C_m with Pressure Ratio

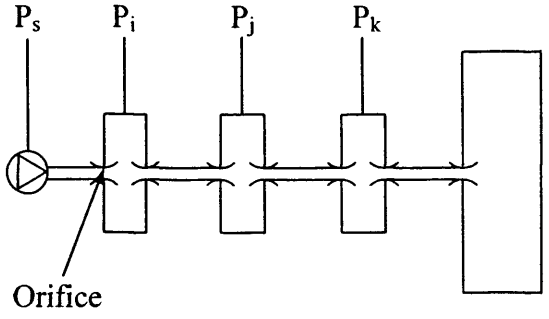

Figure 3.7: Lumped Analogy Corresponding to Figure 3.3

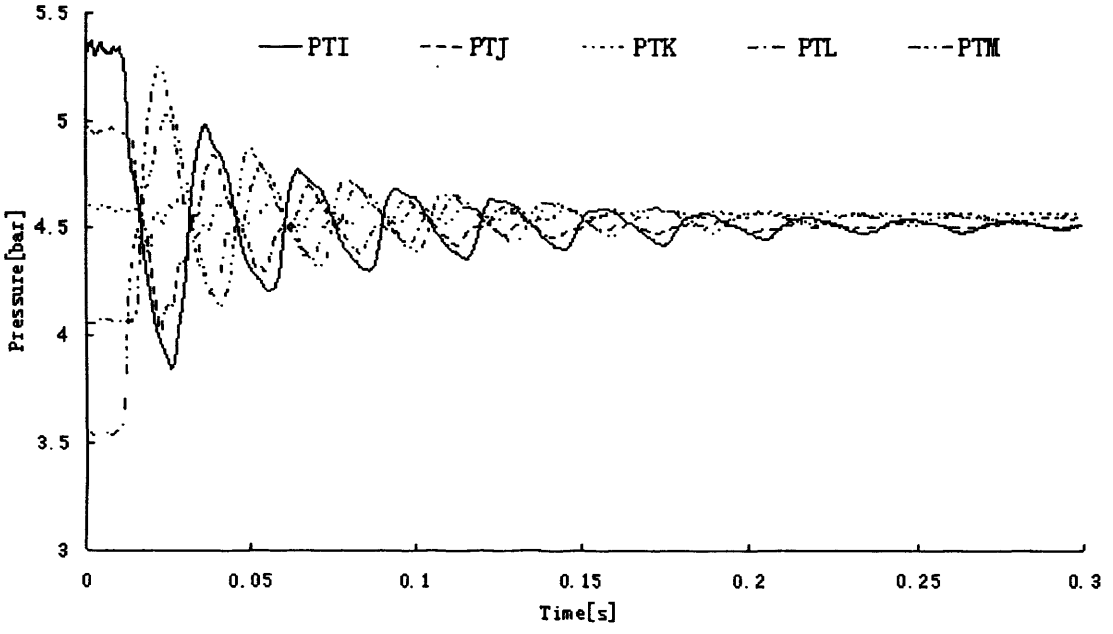

Figure 3.8: Measured Pressure Wave for Both-end Blocked Experimental Setup (PTI=Measured Pressure Signal in Position *i*)

Table 3.3: Initial Conditions Measured by Pressure Transducers and Mass Flow Meter

Components		Values
Pressure Transducer (Absolute) [bar]	P_i	5.34
	P_j	4.96
	P_k	4.59
	P_l	4.06
	P_m	3.55
Mass Flow Meter [Kg/s]		0.0109

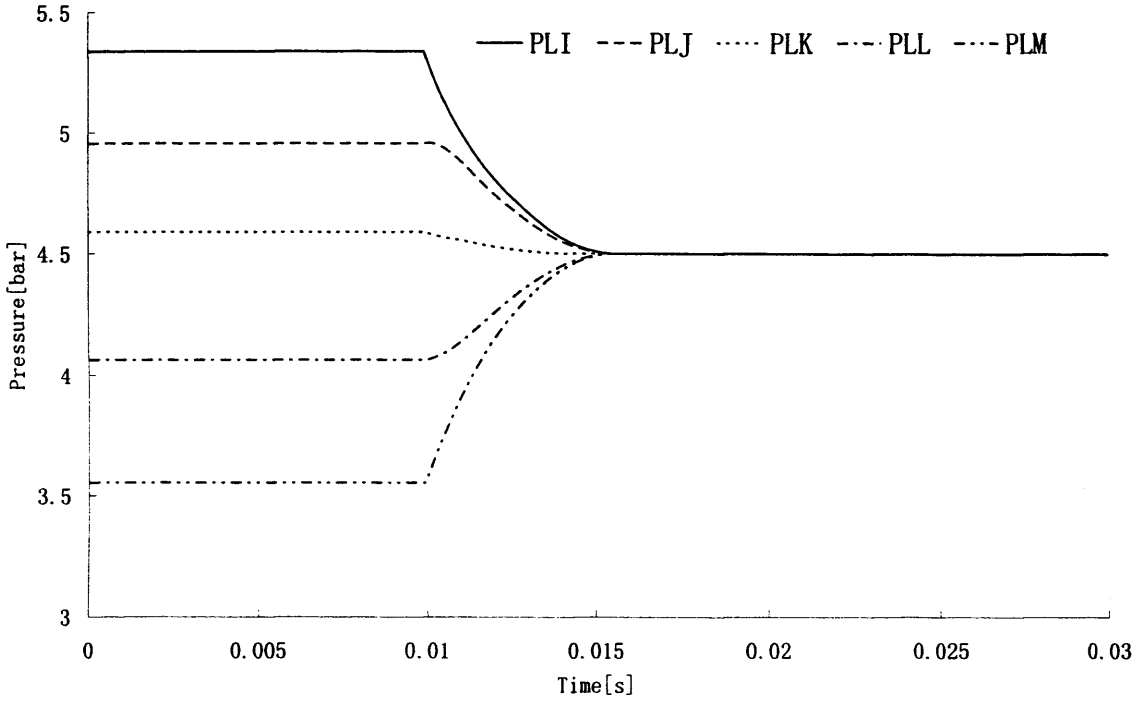

Figure 3.9: Simulated Pressure Wave for Both-end Blocked Experimental Setup (PLI=Simulated Pressure Signal in Position *i* by Lumped Model)

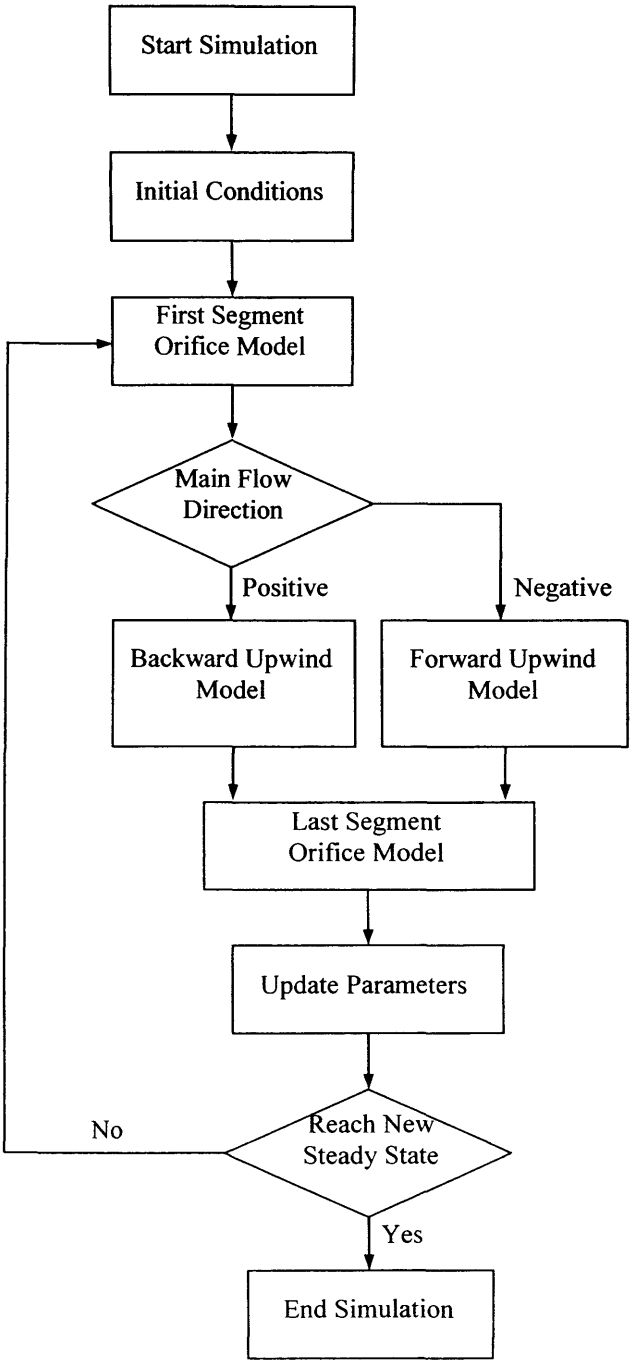

Figure 3.10: Simulation Flow Chart of Combined Model

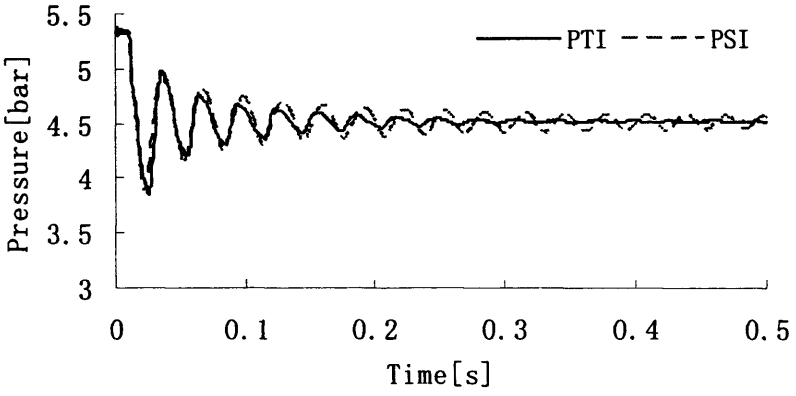

(a)

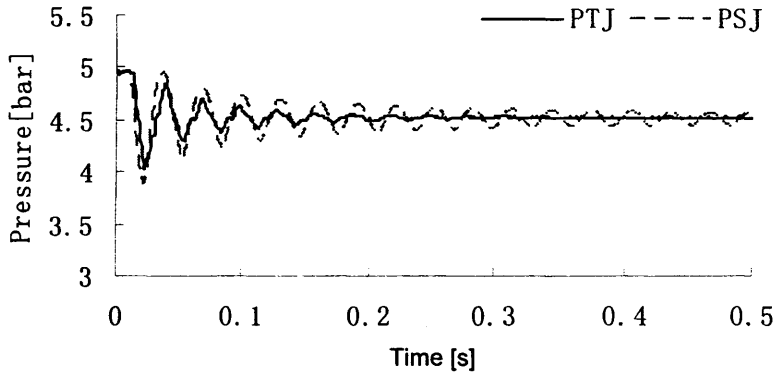

(b)

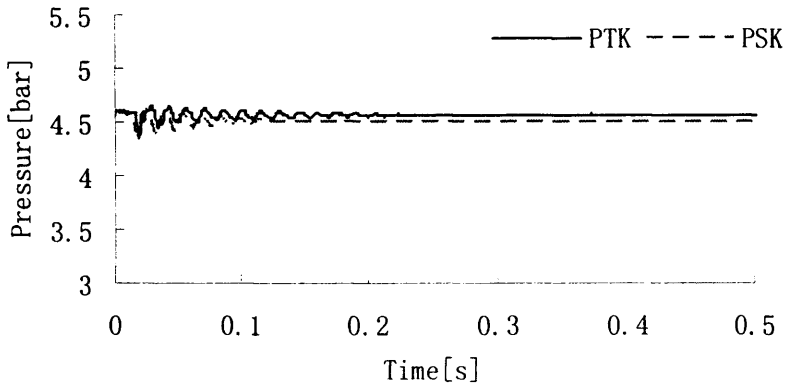

(c)

[continued]

Figure 3.11: Comparisons between Simulation and Experiment Results for Both-end Blocked Model (PT=Experimental Pressure; PS=Simulated Pressure)

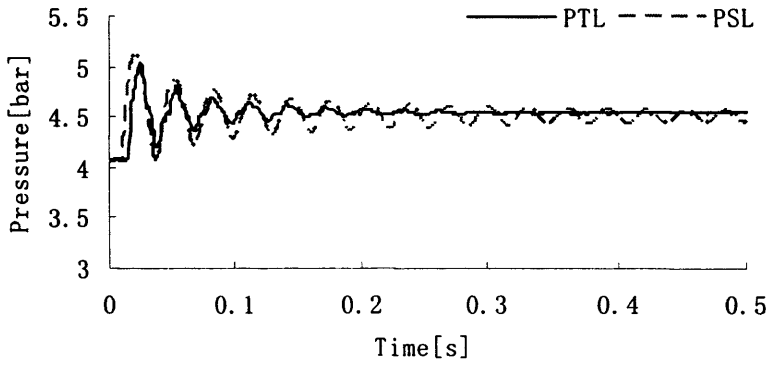

(d)

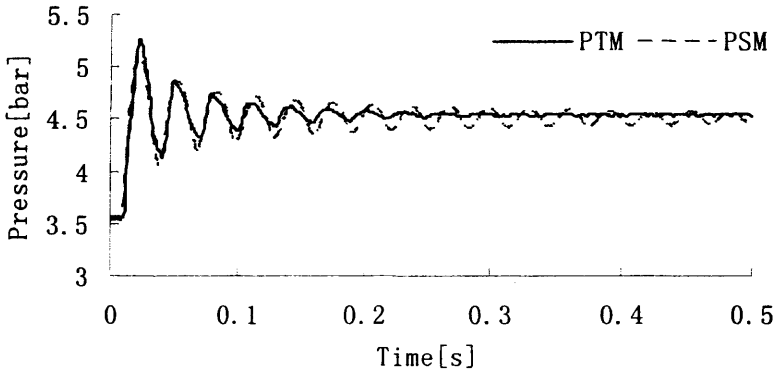

(e)

Figure 3.11: Comparisons between Simulation and Experiment Results for Both-end Blocked Model (PT=Experimental Pressure; PS=Simulated Pressure)

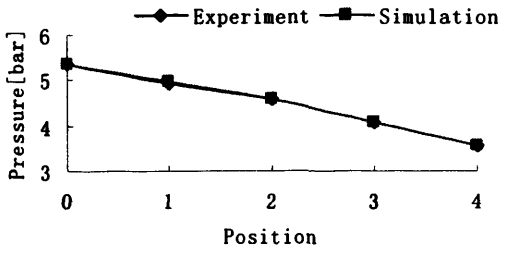

t=0.01 s

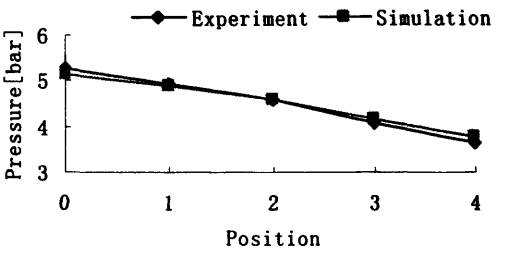

t=0.011 s

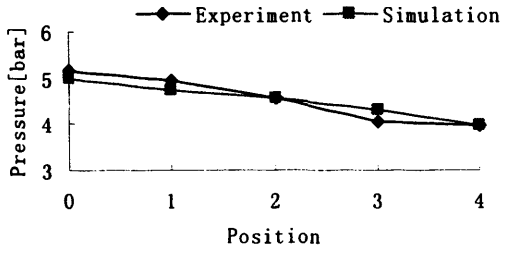

t=0.012 s

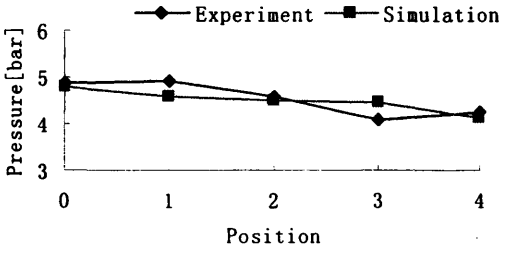

t=0.013 s

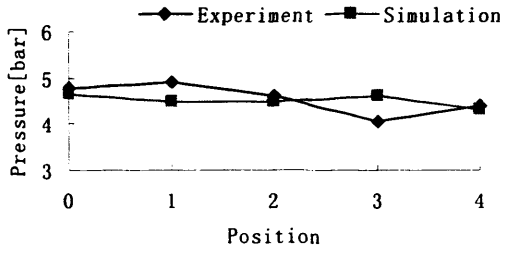

t=0.014 s

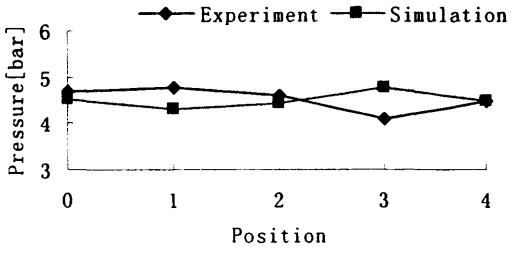

t=0.015 s

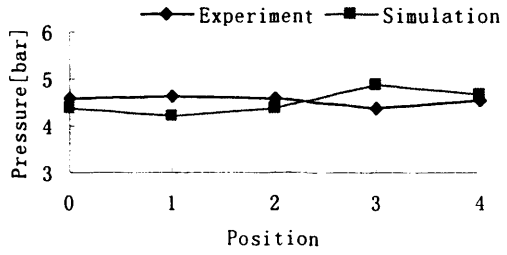

t=0.016 s

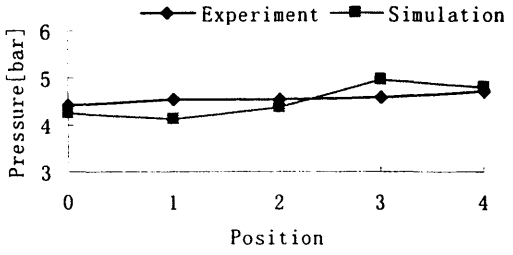

t=0.017 s

[continued]

Figure 3.12: Comparison of One Pressure Ripple between Experimental and Simulation Results for Both-end Block Transmission Line Model

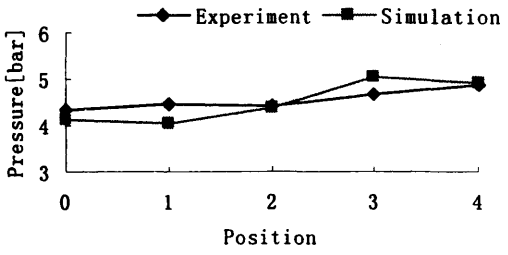

t=0.018 s

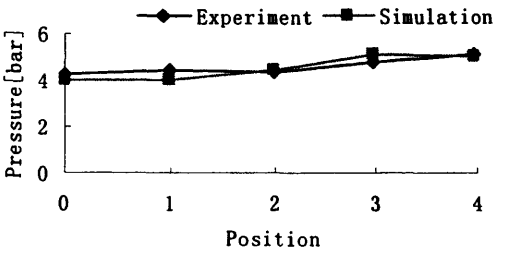

t=0.019 s

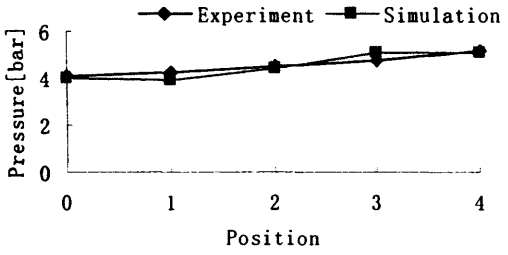

t=0.020 s

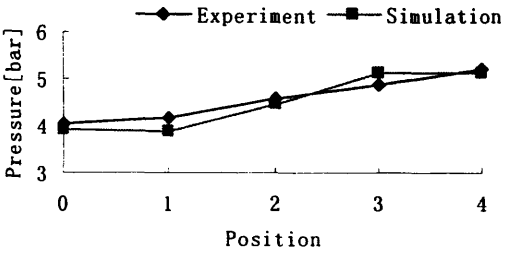

t=0.021 s

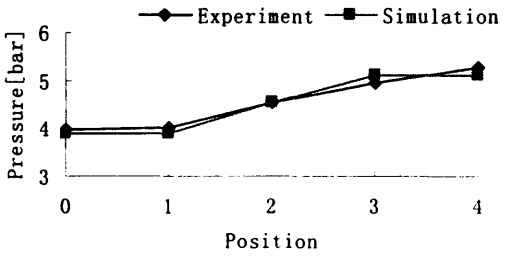

t=0.022 s

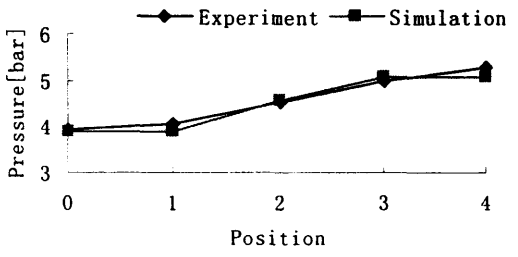

t=0.023 s

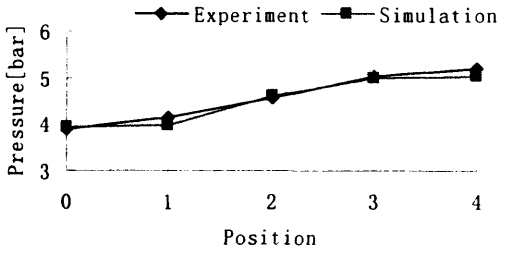

t=0.024 s

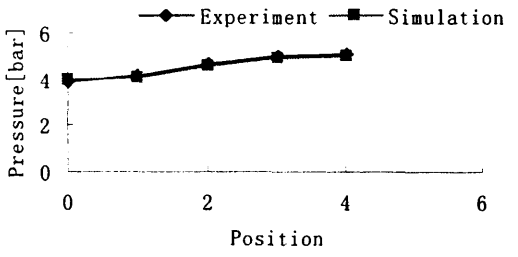

t=0.025 s

[continued]

Figure 3.12: Comparison of One Pressure Ripple between Experimental and Simulation Results for Both-end Block Transmission Line Model

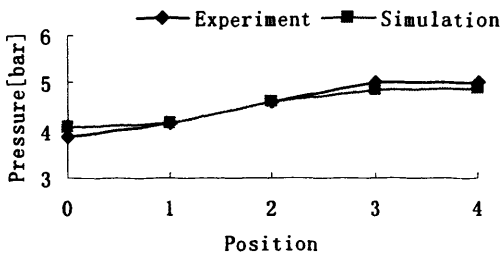

t=0.026 s

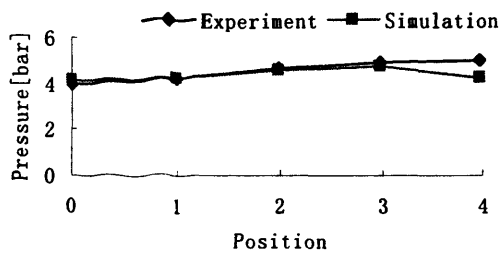

t=0.027 s

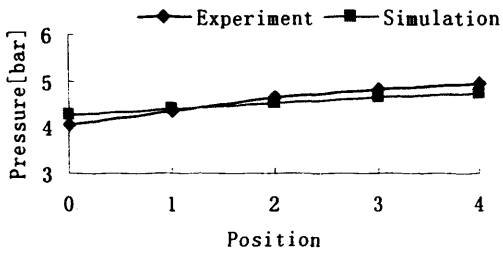

t=0.028 s

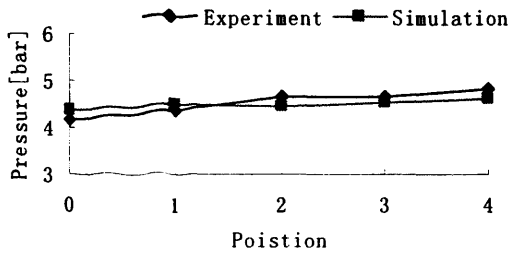

t=0.029 s

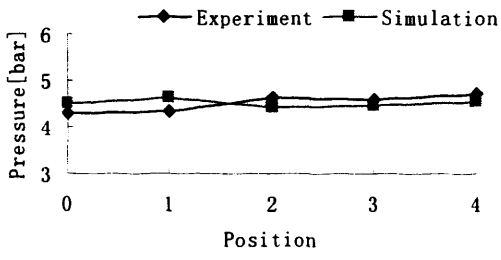

t=0.030 s

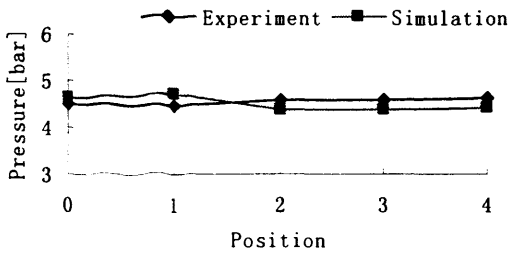

t=0.031 s

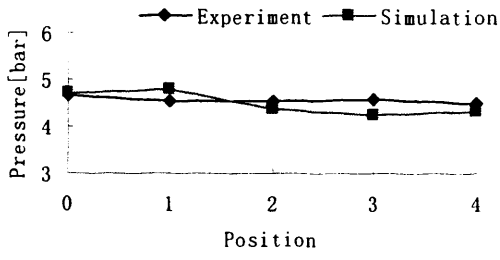

t=0.032 s

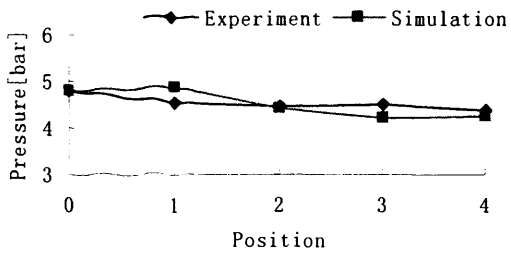

t=0.033 s

[continued]

Figure 3.12: Comparison of One Pressure Ripple between Experimental and Simulation Results for Both-end Block Transmission Line Model

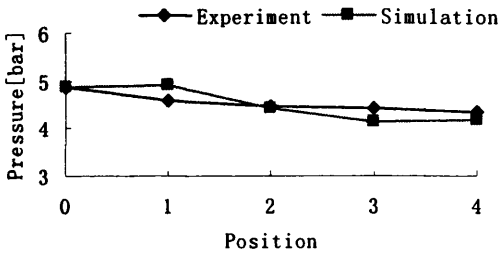

t=0.034 s

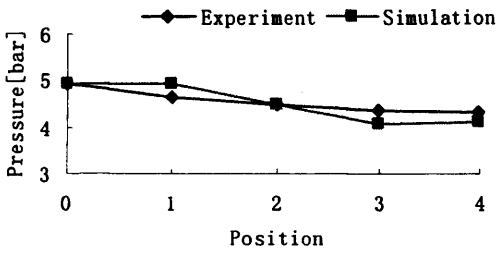

t=0.035 s

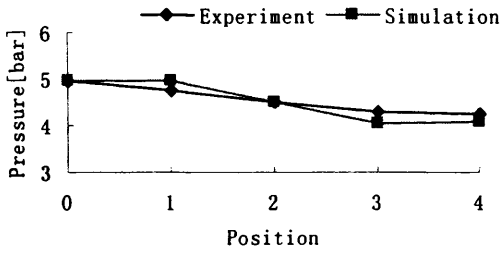

t=0.036 s

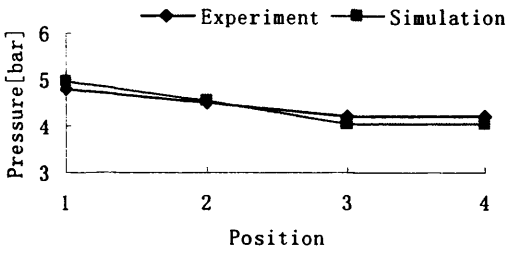

t=0.037 s

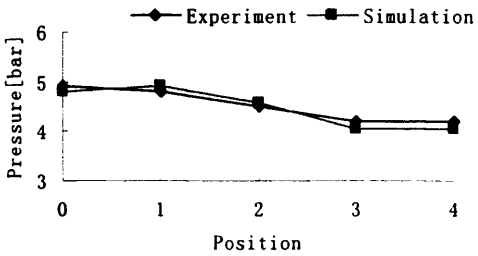

t=0.038 s

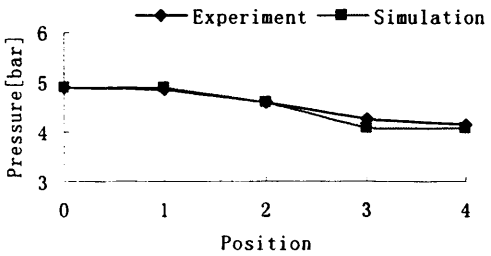

t=0.039 s

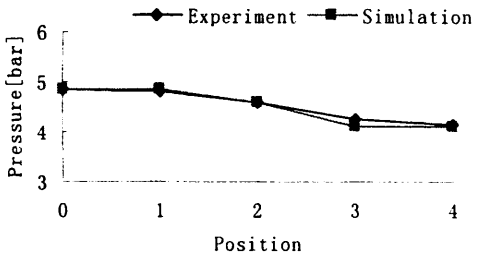

t=0.040 s

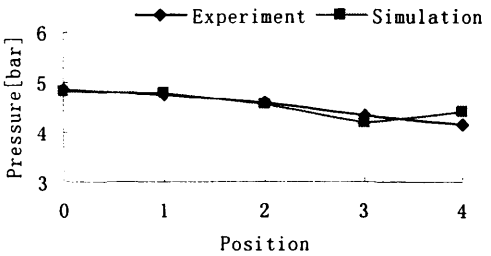

t=0.041 s

[end]

Figure 3.12: Comparison of One Pressure Ripple between Experimental and Simulation Results for Both-end Block Transmission Line Model

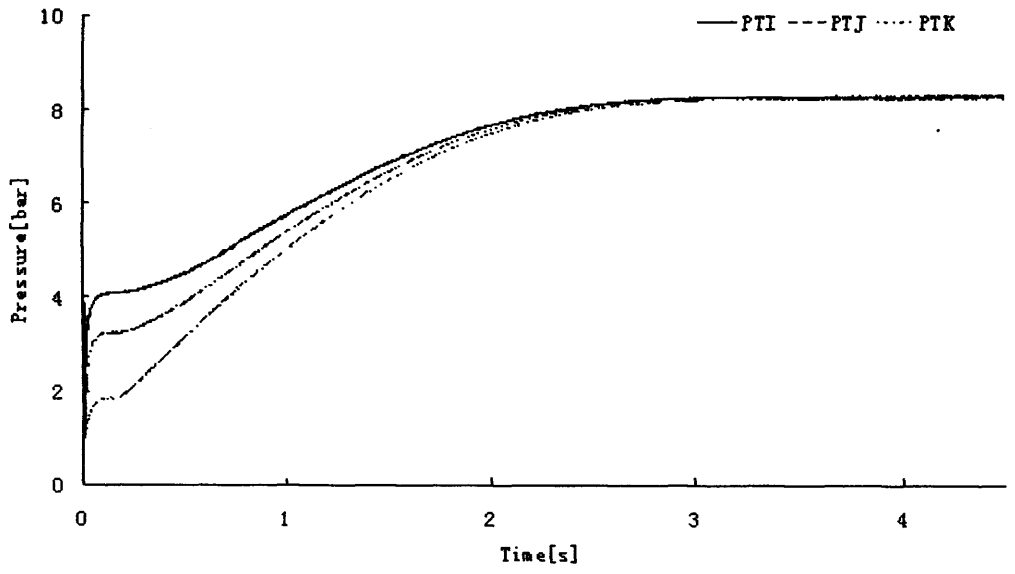

Figure 3.13: Measured Pressure Wave for Air Charging a Large Volume Linked with a 2.8 Meters Transmission Line (PTI=Measured Pressure Signal in Position *i*)

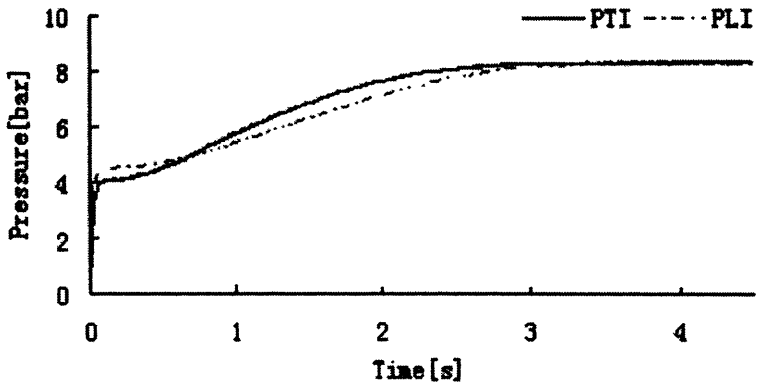

(a)

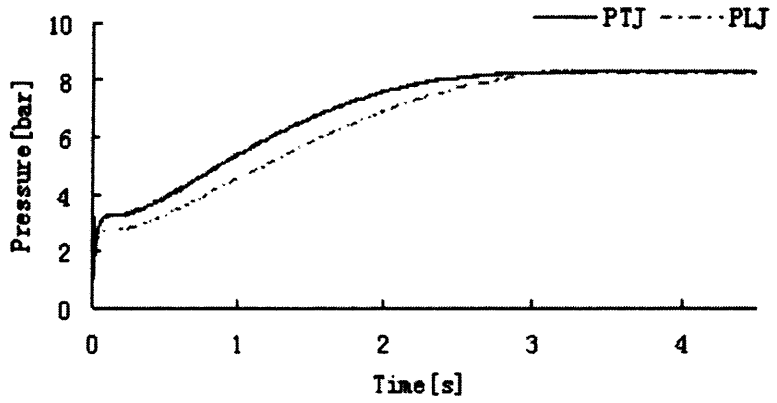

(b)

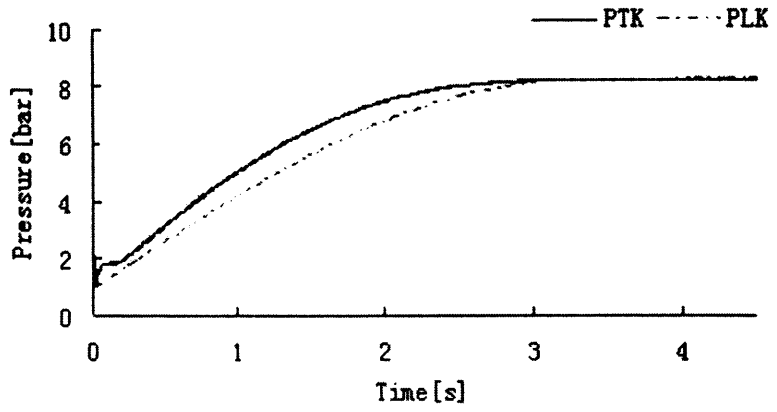

(c)

Figure 3.14: Comparisons between Simulation and Experiment Results for the Model of Air Charging a Large Volume Linked with a 2.8 Meters Transmission Line (PT=Experimental Pressure; PL=Simulated Pressure by Lumped Model)

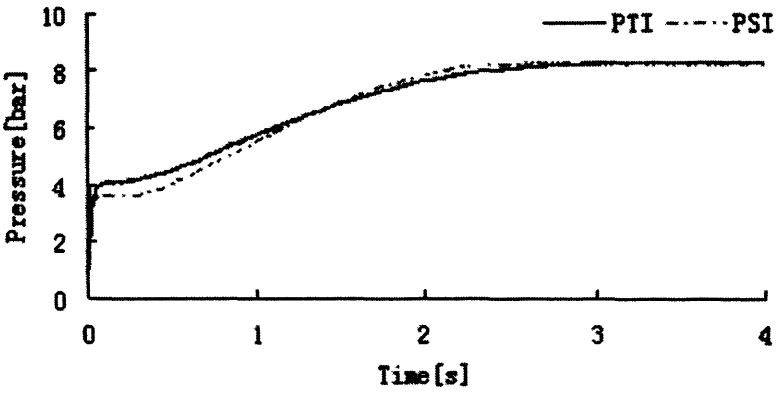

(a)

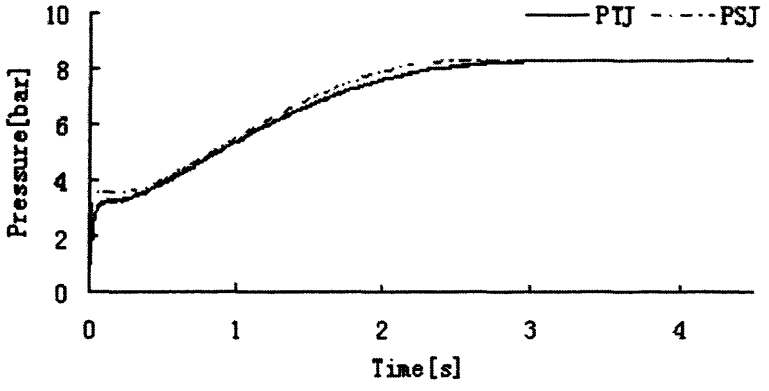

(b)

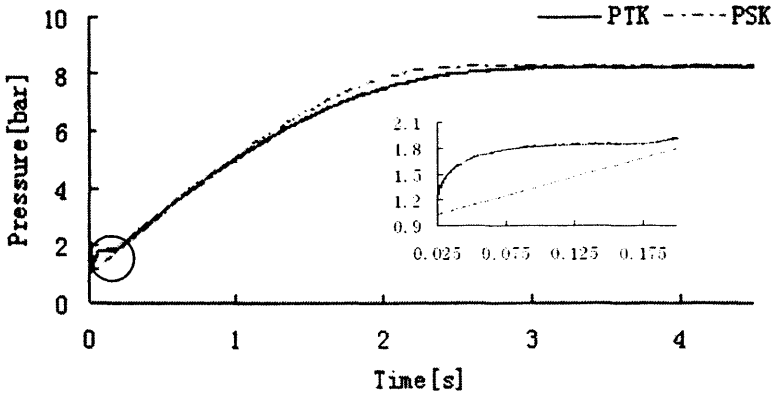

(c)

Figure 3.15: Comparisons between Simulation and Experiment Results for the Model of Air Charging a Large Volume Linked with a 2.8 Meters Transmission Line (PT=Experimental Pressure; PS=Simulated Pressure)

4. PREMIXED COMBUSTOR MODEL

NOMENCLATURE

A	Kinetic constant ($(m^3)^{n-1}/(\sqrt{K} \cdot Kg^{n-1} \cdot s)$)
A_e	Tailpipe cross-section area (m^2)
A_s	Surface area of the combustion zone (m^2)
C_1	Average value for the sinusoidal inlet mass flow (Kg/s)
C_2	Amplitude value for the sinusoidal inlet mass flow (Kg/s)
C_p	Constant pressure specific heat ($J/(Kg \cdot K)$)
C_v	Constant volume specific heat ($J/(Kg \cdot K)$)
D_{tp}	Diameter of the tailpipe (m)
e	Specific internal energy (J/Kg)
E	Activation energy (J/Kg or cal/mol)
F_{ft}	Friction force on the contact surface between the flow and the tailpipe (N)
F_x	Force along x-direction (N)
f	Friction coefficient
h	Heat transfer coefficient ($W/(m^2 \cdot K)$)
L_{c1}	First characteristic length (ratio of combustion zone volume V_c to surface area A_s) (m)
L_{c2}	Second characteristic length (ratio of combustion zone volume to tailpipe cross-section area A_e) (m)
L_{tp}	Length of the tailpipe (m)
$\dot{m}_e$	Exit mass flow rate from the combustion zone (Kg/s)
$\dot{m}_i$	Inlet mass flow rate to the combustion zone (Kg/s)
P	Pressure in combustion zone (bar)

$\tilde{P}$	Pressure in the combustion zone normalized with the ambient pressure
P_0	Ambient pressure (*bar*)
P_e	Pressure at tailpipe entrance (*bar*)
$\tilde{P}_e$	Pressure at the tailpipe entrance normalized with the ambient pressure
P_i	Inlet pressure to combustion zone (*bar*)
$\dot{Q}$	Heat release per unit volume ($J/(m^3 \cdot s)$)
R	Gas constant ($J/(Kg \cdot K)$)
$\dot{R}_f$	Fuel reaction rate (per unit volume) ($Kg/(m^3 \cdot s)$)
S_r	Stoichiometric mass ratio between fuel and oxygen
T	Temperature in combustion zone (K)
$\tilde{T}_a$	Dimensionless activation temperature
$\tilde{T}$	Temperature normalized with the ambient temperature
T_0	Ambient temperature (K)
T_e	Temperature at tailpipe entrance (K)
$\tilde{T}_e$	Temperature at the tailpipe entrance normalized with the ambient temperature
T_i	Inlet temperature to combustion zone (K)
T_w	Wall temperature (K)
u	Velocity of reactant products in the tailpipe (*m/s*)
V_c	Combustion zone volume (m^3)
Y_f	Fuel mass fraction in the combustion zone
$Y_{f,i}$	Inlet fuel mass fraction
Y_o	Oxygen mass fraction in the combustion zone
Z_e	Exit mass flow per combustion zone volume ($Kg/(m^3 \cdot s)$)
Z_i	Inlet mass flow per combustion zone volume ($Kg/(m^3 \cdot s)$)

GREEK LETTERS

ΔH_f	Heat of reaction (per unit fuel mass) (J/Kg)
ϕ	Equivalence ratio
ρ	Density in the combustion zone (Kg/m^3)
ρ_0	Ambient density (Kg/m^3)
ρ_e	Density at the tailpipe entrance (Kg/m^3)
γ	Ratio of specific heat
τ_0	Shear stress of the reactant products along the tailpipe wall (N/m^2)
τ_c	Combustion time (s)
τ_f	Flow time (s)
τ_{HT}	Heat transfer time (s)
ω	Angular frequency for the sinusoidal inlet mass flow (rad/s)
θ	Initial phase for the sinusoidal inlet mass flow (rad)

SUFFIXES

cv	Control volume for combustion zone
f	Fuel
o	Oxygen
s	Control surface of the combustion zone
tpv	Control volume for tailpipe zone

4.1 INTRODUCTION

The work carried out in the first part of this thesis lead onto the consideration of models for the complex oscillations which occur in certain types of combustor.

Combustion can be described most simply as an exothermic reaction of a fuel and an oxidant. The fuel may be gaseous or liquid, but the oxidant is always air. The basic requirements of all combustors may be listed as follows [85-91]:

1) High combustion efficiency (i.e., the fuel should be completely burned so that all its chemical energy is liberated as heat).

2) Reliable and smooth ignition.

3) Wide Stability limits (i.e., the flame should stay alight over wide ranges of pressure, velocity, and air/fuel ratio.).

4) Freedom from pressure pulsations and other manifestations of combustion-induced instability.

5) Low pressure loss.

6) An outlet temperature distribution (pattern factor) that is tailored to maximize the life of the combustor blades and guide vanes.

7) Low emissions of smoke, unburned fuel, and gaseous pollutant species.

8) Design for minimum cost and ease of maintenance.

9) Size and shape compatible with engine envelope.

10) Durability.

11) Multifuel capability.

During the combustion process, oscillatory phenomenon can occur, in which the state variables (such as pressure, temperature, velocity, etc) that describe the conditions in the combustion zone will vary periodically with time. A simple example for combustion oscillation is the "singing flame" phenomenon [92]. If a gas flame is placed in a round vertical tube, it can cause the spontaneous excitation of the natural acoustic modes of the tube. The resulting oscillation is controlled by the location of the flame within the tube, the dimensions of the tube and the characteristics of the gas feeding the tube. Flames are sensitive to excitation from sound, and their response depends on the amplitude and frequency of the sound wave, and the part of the flame on which the sound impinges, for instance Blonbou et al [93] used loudspeakers as the actuator to attenuate the pressure oscillations for a Rijke tube. A neural network model is firstly used to model the nonlinear response of flames to the acoustic disturbances. During the control sequence, this neural network identification model is placed in parallel with the system. The error signal to be minimized may be the difference between the desired and the neural network output due to the pressure oscillation, which is then back-propagated through the neural network identification model to adjust the controller's weights during the control sequence. The output of the controller is amplified to the loudspeakers, with which pressure level attenuation up to 40 dB/Hz is obtained.

The combustion process involves the coupling of a complicated three-dimensional transient chemical flow field, generated by a transient energy release, with a resonant acoustic pressure wave. Variables of pressure, temperature and velocity vary periodically during the cycle of operation, which is characterized by the frequency of oscillation. The basic operation cycle for combustion can be described in a similar way to that of a conventional Otto cycle, as shown in Figure 4.1. The mixed gas and air in the combustion chamber are firstly ignited by a spark plug or other ways (Figure 4.1 (a)). The consequent rise of the pressure will then drive the combustion products out to the exhaust and inlet pipes (Figure 4.1 (b)). Due to the inertia of the moving gas column in the exhaust pipe, which will create the negative pressure (the ambient pressure is treated as 0 bar) in the combustion chamber, the fresh gas and air are drawn in through the inlet pipe (Figure 4.1 (c)). Some exhaust reactive products are also recycled and then the re-

ignition occurs when hot reactive products from the previous cycle mix with the fresh reactants. This process repeats to form one operation cycle (Figure 4.1 (d)).

The acoustic and flame interaction was studied first by Higgins, and then by Rayleigh [34], who stated the importance of the phase-lag between energy release and acoustic pressure wave for sustained combustion-driven oscillations. Rayleigh [35] further explained that both these oscillations are amplified when a phase coupling occurs between the flame front and the acoustic field inside the tube. The Rayleigh criterion states that if the local unsteady heat release is in-phase with the local pressure fluctuation, the pressure wave associated with the fluctuation will be locally amplified. Thermo-acoustic combustion instabilities represent one of the main threats for modern combustors, as they involve pressure and heat release fluctuations characterised by large amplitudes and low frequencies. The coupling mechanism self-sustains oscillations and causes the combustion process to become unstable, exciting the resonant acoustic modes of the combustion chamber. These combustion instabilities induce non-uniformity of exhausted gas thermal distribution, the growth of thermal-NO_x production, structure vibrations, increased heat transfer, roll torque, and sometimes, destruction of the burner.

For development and understanding of the fundamental fluid dynamics, combustion, heat transfer processes occurring during the combustion and the corresponding instabilities, mathematical models are needed. A number of theoretical models have been developed for the simulation of combustion instabilities. Due to the complexity of the operating process of the combustion system, models are always based on a certain amount of empiricism. Although such models do not allow the complete design of a whole combustion system, they do provide insights into operating mechanisms and the effects of design changes.

Fureby [94] develops a simulation technique, founded on a physical model based on continuum mechanics mixture theories, which employs the LES (Large Eddy Simulation) technique. In LES, it is assumed that the variables describing the spatial and temporal evolution of the flow can be decomposed into two components; the "Grid Scale" (GS) part and the "Sub Grid Scale" (SGS) part. The GS component of the variables describes the evolution of the GS eddies, whose motions depend on the geometry of the flow domain and the imposed boundary conditions. Furthermore, the

GS eddies contain a significant part of the kinetic energy. The SGS components describe the evolution of the SGS eddies, whose motions are assumed to be of a more isotropic nature than the GS eddies. The agreement of the LES model with the experimental observation is acceptable apart from the region around the inlet.

Benelli et al [95] present preliminary 2D simulations of the Lennox Warm Air Furnace using the commercially available computer code "FLUENT" running on VAX 8530 and Cray X-MP/14 hardware. Benelli stated: "while acoustic vibrations were always easily captured, tuning of the combustion with them was more difficult to reproduce". It was suggested that the problem could be alleviated with more detailed modelling of the way that reactants mix together. In fact, the simplification from a three-dimensional furnace geometry to a two-dimensional simulation could be a source of error as the near inlet geometry was found to play an important role in determining both the mixing and the combustion rate. To establish the appropriate corrective factors to simplify the analysis is not straightforward.

Annaswmy and Ghoniem [96], Culick [97] and Krstic et al [98] address the definition of the model exploiting the system dynamics by means of the analytical transfer functions or sets of ordinary differential equations derived by modal decomposition of the equations expressing the balances of mass, energy and momentum. One of the main problems that can affect mathematical models is the sensitivity of the performances on their parameters. In fact, when non linear couplings play a strong influence on combustion dynamics, such as those between rapid chemical reactions, turbulent flow and acoustic phenomena, uncertainty on the parameters must be carefully considered as it can determine the model failure. Moreover, the model parameters may change abruptly and in an unpredictable fashion during the operation of the combustion system, determining a drastic decay of the model performance.

The identification of the system dynamics by means of input-output experimental measurements provides a useful solution to the definition of a reliable model. This approach allows one to bypass both the exact determination of model parameters and of their unpredictable variations and achieve a deep physical knowledge of the process and of its governing equations, which can be achieved via artificial neural networks. The derived model can predict the evolution of the oscillations of the acoustic field inside

the combustion chamber due to thermo-acoustic instability, as described by Xue et al [8], Cammarata et al [99] and Christo et al [100]. This identification neural network model can be further used to realize online adaptive pressure oscillation control. During the control sequence, the identification model is placed in parallel with the system. The error signal (rms value of the pressure oscillations) to be minimized may be different between the desired and the identified model output, which is then back propagated through the identification model and then through the controller to update the weights of the controller to minimize the rms value of the pressure oscillations, as described by Blonbou et al [1, 93], Gutmark et al [101], McManus et al [102], Liu and Daley [103], and Docquier and Candel [104].

Based on the work by Peters [105] who analyzed the spectral behaviour of turbulent premixed combustion and the combustion heat release model by Schmid et al [106], Hirsch et al [107] presents a model for the spectral distribution of heat release in turbulent premixed combustion and shows that it can be applied to calculate the sound pressure. Hirsch uses a simultaneous PIV-LIF technique to determine the spatial spectra of the progress variable variance and the turbulence kinetic energy. The spectra of progress variable correspond well with model spectra derived from the homogeneous turbulence. Mapping these Eulerian spatial spectra to Lagrangian time spectra, it is shown that the integral frequency spectrum of heat release fluctuation can be computed using local values of time averaged heat release rate density, turbulence kinetic energy and turbulence length scale.

In this study, a premixed combustion model is designed based on the conservation laws to predict the pressure oscillations. The effects of friction in the combustor tailpipe, heat loss from the combustion zone and mass flow rate are investigated as well. With different operating parameters, oscillating combustion, steady flames and blow-out are all predicted. The predicted simulation results are compared with the experimental data. The laboratory observations confirm that the premixed combustor model can predict the pressure instabilities, which is the foundation for the establishment of a more complicated model and for the future pressure oscillation control purposes.

4.2 A PREMIXED COMBUSTOR MODEL

A theoretical model for combustion in a system comprised of a combustor and tailpipe is firstly provided. Characteristic geometric and operational parameters for the combustor are identified in the dimensionless form of the governing equations. It is shown that the solution of conservation equations for mass, species, momentum and energy will lead to oscillating combustion, producing relatively large amplitude pressure pulses. Results of the simulation are then favourably compared to laboratory observations of a combustor operating with parameters similar to those used in the numerical model.

The designed zero-dimensional model takes the form of a thermal combustion model and was initially proposed by Richards et al [108] at the Energy & Technology Center of Morgantown WV, and then developed by Marsano [38, 109] and Hamid [110] at Cardiff University. Richards's model considers oscillations produced with a steady supply of fuel and air; while Marsano gives a sinusoidal inlet mass flow into the combustor, and Hamid includes the oscillatory heat transfer coefficient into the model. The designed model is simple enough to run on a standard PC with relatively short CPU times, which allows investigation of the influence of simple design changes and an insight into the governing processes of this developing combustion technology.

Indeed the pure fuel and open air inlet of the combustion system will generate irregularities in the oscillations, such as the amplitude modulation and running phase shift between pressure and temperature [111]. The non-premixed inlet affects the mixing of reactants and hence the onset of the combustion, which in turn changes the Rayleigh phase. In addition, because the fuel inlet is driven by the high upstream pressure, the pressure in the single inlet should fluctuate around a value a slightly above the atmosphere. The first step to adapt the model is to introduce a non-steady supply of premixed fuel and air. In next chapter, the conservation laws will be applied to inlet pipe and tailpipe respectively, hence a more accurate combustion model will be designed.

4.2.1 Combustor Geometry and Experiment Results

The schematic layout of the experimental combustor is shown in Figure 4.2, which consists of an inlet pipe, combustion chamber and tailpipe. The combustor was of the Helmholtz type. In these types of combustors, the cold air and fuel in the inlet restriction act as a resistance for the gases attempting to exit the combustion chamber through the inlet. Nevertheless in practice a considerable amount of gas flows through the inlet during the positive pressure part of the cycle. This back-flow complicates the process further.

In this chapter, only the combustor and the tailpipe are considered. Hence, the simplified combustor model geometry is shown in Figure 4.3. In Figure 4.3 (a), the shaded region represents a control volume for the combustion zone. The premixed fuel and air enter through the inlet port, at inlet temperature T_i, and fuel mass fraction $Y_{f,i}$. In Figure 4.3 (b), the tailpipe control volume is again identified by the shaded region. The ambient pressure at the combustor exit is P_0. A constant friction factor f is specified along the tailpipe length.

The pressure wave is measured using a fast responding piezo-electric pressure transducer, and the temperature is measured with fine wire thermocouples. The temperature measurements are corrected because of the slow thermocouple response compared to the cycle time; these corrections depend on the mass of the junction and on the local heat transfer from the gas to the junction. Velocity measurements are carried out using Laser Doppler Anemometry [111].

The most important measurement to compare different operating conditions and burner configurations is the pressure measurement. The evaluation of the frequency and the pressure amplitudes shows an important feature of the Helmholtz type combustor. Figure 4.4 (a) shows the instantaneous experimental data of pressure in the combustion chamber. Figure 4.4 (b) shows the FFT analysis result for measured pressure oscillations via Matlab software.

4.2.2 General Assumptions

The model development employs conservation equations for mass, species, momentum and energy in the combustion zone. A bi-molecular reaction rate law is used to describe the fuel reaction rate with rate constant obtained from the propane combustion data. These equations are coupled to a combined expression for mass and momentum conservation in the tailpipe, where the effect of friction is considered.

Due to the zero-dimensional model, the pressure, temperature and other physical variables are assumed to be space-constant. Therefore the combustion chamber is treated as a well-mixed region. Hence, within the combustion chamber, the unknown functions are the pressure *P(t)*, the temperature *T(t)* and the mass fraction *Y(t)*, which are functions of time only. The combustor walls are maintained at a constant temperature T_w with a specified convection coefficient h.

It is assumed that the instantaneous values of the pressure P and the temperature T in the combustion zone are related to the tailpipe entrance pressure P_e and temperature T_e via isentropic acceleration from the combustion zone [112, 113]. The friction in the tailpipe is accounted for via a conventional friction factor f, as defined by Schlichting and Klaus [114], in which the friction force is developed from the wall shear stress in terms of the friction coefficient. Finally the tailpipe velocity is readily related to the exit mass flow rate $\dot{m}_e(t)$.

4.2.3 Conservation Equations in Combustion Zone

The conservation equations in the combustion zone and tailpipe zone are written as in standard texts [115-121]. Firstly, the conservation laws of mass, species and energy are used for the combustion chamber.

Based on the first law of thermodynamics, a control volume equation for energy conservation in the combustion zone is written as:

$$\frac{d}{dt}\int_{cv}\rho\left(e+\frac{1}{2}\upsilon^2\right)dV=\int_{cv}\dot{Q}dV-\oint_s\rho\left(e+\frac{1}{2}\upsilon^2\right)\bar{\upsilon}\cdot\bar{n}ds-\oint_s\bar{q}\cdot\bar{n}ds-\oint_sP\bar{\upsilon}\cdot\bar{n}ds \qquad (4.1)$$

The left side of this equation represents the change rate of energy of the system; while, the first item in the right side is the heat release rate (per unit volume) from the combustion, the second is the net flow energy rate through the combustor surface, the third is the heat transfer rate with control volume interface, and the last is the rate of the net pressure work through the combustor surface. In Equation (4.1), $\upsilon^2/2$ is the specific kinetic energy, $\bar{\upsilon}$ is the velocity vector, $\bar{n}$ is the unit vector, and $\bar{q}$ is the heat transfer rate vector. The suffixes of the integral symbol *cv* and *s* represent the control volume and the control surface of the combustion zone respectively.

To solve the Equation (4.1), the following assumptions are employed:

1) The combustion volume is considered as a homogeneous and isochoric zone, and ideal gas properties are used: $e=C_vT$, $C_p=C_v+R$, and $\gamma=\frac{C_p}{C_v}$.

2) Compared with the specific internal energy e, the contributions of the specific kinetic energy $\upsilon^2/2$ to the energy change are negligible.

3) The exit temperature T_e and the exit pressure P_e are assumed to be related to the combustion temperature T and pressure P by adiabatic isentropic acceleration to the exit Mach number M_e, which means that we change process variables from P and T to P_e and T_e in an adiabatic reversible process.

The inlet pressure and temperature into the combustion volume are P_i and T_i, which are assumed to be equal to ambient pressure P_0 and temperature T_0. The pressure and temperature in the combustion zone are P and T, whilst, the exit pressure and temperature in the combustion volume are expressed as P_e and T_e.

The following variables are used:

1) Inlet mass flow per combustion zone volume

$$Z_i = \frac{\dot{m}_i}{V_c} \tag{4.2}$$

2) Exit mass flow per combustion zone volume

$$Z_e = \frac{\dot{m}_e}{V_c} \tag{4.3}$$

3) The first characteristic length (ratio of combustion zone volume V_c to surface area A_s)

$$L_{c1} = \frac{V_c}{A_s} \tag{4.4}$$

where V_c is the combustion zone volume and A_s is the combustor surface area.

With the assumptions and definitions above, Equation (4.1) becomes:

$$\frac{1}{\gamma - 1}\frac{dP}{dt} = C_p\left(T_i Z_i - T Z_e\right) + \dot{Q} + \frac{h}{L_{c1}}\left(T_w - T\right) \tag{4.5}$$

The conservation of mass for the combustion zone is:

$$\frac{\partial}{\partial t}\int_{cv} \rho dV = -\oint_s \rho \bar{v} \cdot \bar{n} ds \tag{4.6}$$

which states that the mass changes in combustion zone are derived from the difference between inlet and outlet flows.

Employing similar assumptions as in Equation (4.5), Equation (4.6) becomes:

$$\frac{d\rho}{dt} = Z_i - Z_e \tag{4.7}$$

By means of the perfect gas law $\rho = \frac{P}{RT}$, Equations (4.7) becomes:

$$\frac{1}{RT}\frac{dP}{dt} - \frac{P}{RT^2}\frac{dT}{dt} = Z_i - Z_e \tag{4.8}$$

To simplify the resulting expression, the following variables are defined:

1) Flow Time

$$\tau_f = \frac{\rho_0}{Z_i} \tag{4.9}$$

2) Heat transfer time

$$\tau_{HT} = \frac{L_{c1}\rho_0 C_p T_0}{hT_w} \tag{4.10}$$

3) Combustion time

$$\tau_c = \frac{\rho_0 C_p T_0}{\dot{Q}} \tag{4.11}$$

Referring to the definition of Z_i (Equation (4.2)), the flow time τ_f is the mean residence time for non-reactive isothermal gas to pass through the combustion volume (the "cold" residence time). The flow time is thus a constant determined from the steady mass flow rate entering the combustor. τ_f does not correspond to a residence time in the reactive pulsating case, hence the expression flow time is appropriately called "cold residence time" or "non-reactive residence time". For constant heat transfer coefficient and wall

temperature, the heat transfer time is constant. However, the combustion time is not constant: it varies with the instantaneous value of the heat release rate, as to be expected and as described as follows.

Normalizing the temperature and pressure with the ambient temperature and pressure and denoting them with a tilde, Equations (4.5) and (4.7) are combined to give:

$$\frac{d\tilde{T}}{dt}=\left(\frac{1}{\tau_f}+\frac{1}{\tau_{HT}}+\frac{1}{\tau_c}\right)\frac{\gamma\tilde{T}}{\tilde{P}}-\left((\gamma-1)\frac{Z_e}{\rho_0}+\frac{1}{\tau_f}+\frac{\gamma T_0}{\tau_{HT}T_w}\right)\frac{\tilde{T}^2}{\tilde{P}} \tag{4.12}$$

Here, the inlet temperature T_i is regarded as the ambient temperature T_0. Equation (4.12) is an expression representing conservation of thermal energy in the combustion zone. An equation to describe the pressure variation is easily developed by combining Equation (4.12) and a version of conservation of mass (Equation (4.7)). Expressing density from the perfect gas law as a function of the normalized pressure and temperature, the result is:

$$\frac{d\tilde{P}}{dt}=\left(\frac{1}{\tau_f}+\frac{1}{\tau_{HT}}+\frac{1}{\tau_c}-\left(\frac{Z_e}{\rho_0}-\frac{T_0}{\tau_{HT}T_w}\right)\tilde{T}\right)\gamma \tag{4.13}$$

For solving Equations (4.12) and (4.13), the expression for combustion time τ_c needs to be developed. The instantaneous heat release (per unit volume) $\dot{Q}$ is the product of the heat of reaction (per unit fuel mass) ΔH_f and the fuel reaction rate (per unit volume) $\dot{R}_f$, which is:

$$\dot{Q}=\Delta H_f \dot{R}_f \tag{4.14}$$

The fuel used in the combustor is propane. Its ΔH_f value could be found in Rose's or Perry's Chemical Tables [122, 123].

A bi-molecular rate law between fuel (subscript *f*) and oxygen (subscript *o*) is used to describe the fuel reaction rate, which is:

$$C_3H_8 + 5O_2 = 3CO_2 + 4H_2O$$

Then the fuel reaction rate is given by:

$$\dot{R}_f = AT^{1/2}\rho^2 Y_o Y_f e^{-E/RT} \tag{4.15}$$

where A is the kinetic constant, Y_0 is the instantaneous oxygen mass fraction in the combustion zone, Y_f is the instantaneous fuel mass fraction in combustion zone, and E is the activation energy.

The mass fractions of fuel and oxygen are determined from the conservation of species in combustion zone. For fuel, it is:

$$\frac{d}{dt}\int_v \rho Y_f dV = -\oint_s \rho Y_f \bar{v}\cdot\bar{n}ds - \int_v \dot{R}_f dV \tag{4.16}$$

which means that the change rate of fuel mass is equal to the rate of the net fuel mass flow through the combustor surface subtracting the parts consumed in the combustion process.

With the same assumptions for deriving the Equation (4.5) from Equation (4.1), the resulted fuel mass fraction is:

$$\frac{dY_f}{dt} = \left(Y_{f,i} - Y_f\right)\frac{\tilde{T}}{\tilde{P}}\frac{1}{\tau_f} - \frac{\tilde{T}}{\tilde{P}}\left(\frac{C_p T_0}{\Delta H_f}\right)\frac{1}{\tau_c} \tag{4.17}$$

For oxygen, the formulation for conservation of species is:

$$\frac{d}{dt}\int_v \rho Y_o dV = -\oint_s \rho Y_o \bar{v}\cdot\bar{n}ds - \int_v S_r \dot{R}_f dV \tag{4.18}$$

Hence, the resulted oxygen mass fraction is:

$$\frac{dY_o}{dt} = (Y_{o,i} - Y_o)\frac{\widetilde{T}}{\widetilde{P}}\frac{1}{\tau_f} - S_r\frac{\widetilde{T}}{\widetilde{P}}\left(\frac{C_p T_0}{\Delta H_f}\right)\frac{1}{\tau_c} \tag{4.19}$$

where $Y_{f,i}$ is the inlet fuel mass fraction, $Y_{o,i}$ is the inlet oxygen mass fraction, and S_r is the stoichiometric mass ratio between oxygen and fuel.

It is recognized that the equation for oxygen mass fraction (Equation (4.19)) normalized by the stoichiometric ratio has exactly the same form as Equation (4.17). It can be shown that both equations will have the same solution for stoichiometric inlet conditions, and stoichiometric initial conditions. Thus, when stoichiometric conditions are imposed, the analysis is simplified because the instantaneous oxygen mass fraction is proportional to the fuel mass fraction by a factor of S_r. Although this simplification formally restricts the analysis to stoichiometric inlet and initial conditions, the simulation can be used for lean conditions.

Complete combustion of a hydrocarbon fuel requires sufficient air to convert the fuel completely to carbon dioxide and water vapour. The stoichiometric air/fuel ratio can be readily calculated from the reaction equation as shown above, being for propane 15.81. In comparing the combustion characteristics of different fuels, it is sometimes convenient to express the mixture strength in terms of an equivalence ratio ϕ. The equivalence ratio is the actual fuel/air ratio divided by the stoichiometric fuel/air ratio. Hence, for a certain equivalence ratio ϕ, the inlet fuel (propane) and oxygen mass fractions are:

$$\begin{cases} Y_{f,i} = \dfrac{253\times\phi}{4000 + 253\times\phi} \\ Y_{o,i} = \dfrac{920}{4000 + 253\times\phi} \end{cases} \tag{4.20}$$

Combining the Equations (4.11), (4.14) and (4.15), the combustion time is then:

$$\frac{1}{\tau_c} = A' \frac{\Delta H_f}{C_p T_0} \frac{\tilde{P}^2}{\tilde{T}^{3/2}} Y_f \frac{Y_o}{S_r} e^{-\tilde{T}_a/\tilde{T}} \tag{4.21}$$

where A' is a constant derived from the product of different constants in mentioned three equations $\left(A' = (A \cdot P_0 \cdot S_r)/(R \cdot T_0^{1/2})\right)$, and $\tilde{T}_a$ is a dimensionless activation temperature $\left(\tilde{T}_a = E/(R \cdot T_0)\right)$. From Kretschmer etc [124-127], the values of A' and $\tilde{T}_a$ are $3.85 \times 10^8 s^{-1}$ and 50 respectively. The value of $\tilde{T}_a$ represents the activation energy of 30 $Kcal/Kmol$.

For stoichiometric conditions, Equation (4.21) becomes:

$$\frac{1}{\tau_c} = A' \frac{\Delta H_f}{C_p T_0} \frac{\tilde{P}^2}{\tilde{T}^{3/2}} Y_f^2 e^{-\tilde{T}_a/\tilde{T}} \tag{4.22}$$

To complete the development of the equation set, it is necessary to derive the equations for the tailpipe to determine the exit mass flow rate $\dot{m}_e$.

4.2.4 Conservation Equations in Tailpipe Zone

The exit mass flow Z_e appears in Equations (4.12) and (4.13), and must be determined for the whole development of the combustor model. A similar procedure is used to predict the Helmholtz frequency of the combined tailpipe and combustion region as described by Zinn [128]. Here it is assumed that the gases in the tailpipe move as a slug, the mean flow is neglected and the governing equations are linearized for small oscillations. In this development, only the slug flow assumption is retained, and an approximate integration of density along the tailpipe is used.

As shown in Figure 4.3 (b), a control volume indicated by the shaded region extends to the ends of the tailpipe. The pressure P_e and the temperature T_e at the entrance of the tailpipe are related to the pressure P and temperature T in the combustor by isentropic acceleration or deceleration into or from the tailpipe.

A control formulation for the momentum equation in the tailpipe is then written:

$$\sum F_x = \frac{d}{dt}\int_{pv} \rho u dV + \oint \rho u \bar{u} \cdot \bar{n} ds \tag{4.23}$$

The left side of the equation gives the summation of all forces acting in a given direction (x-direction) on a control volume. These forces include the pressure acting on the area at either end of the tailpipe, and the force generated by wall friction along the tailpipe length F_f. The first item in right side of the equation is the change rate of momentum in the tailpipe control zone, and the second is the rate of change of the net momentum flow out of the tailpipe control zone in the same direction as the sum of all forces.

Hence, Equation (4.23) is:

$$(P_e - P_0)A_e + F_f = \frac{du}{dt}\int_{pv} \rho dV + u\left(\frac{d}{dt}\int_{pv} \rho dV + \oint \rho \bar{u} \cdot \bar{n} ds\right) \tag{4.24}$$

According to the conservation of mass in tailpipe, the term in brackets on the right side is zero, that is:

$$\frac{d}{dt}\int_{pv} \rho dV + \oint \rho \bar{u} \cdot \bar{n} ds = 0$$

The integral of density in the tailpipe control volume is approximated as the product of the tailpipe entrance density ρ_e and the tailpipe volume. The friction force F_f is developed from the wall shear stress in terms of the conventional friction coefficient f, as shown in Schlichting's text [114]. Using the instantaneous tailpipe velocity in Schlichting's expression and considering the shear stress at the tailpipe wall, it is shown that:

$$\tau_0 = \frac{1}{8} f \rho u^2$$

The friction force F_f is then the shear stress τ_0 multiplied by the tailpipe surface area. The sign of the velocity is needed to be considered for the direction of the force acting on the control volume. Performing these steps, Equation (4.24) becomes:

$$\frac{du}{dt} = \left(\tilde{P}_e - 1\right)\frac{RT_0}{L_{tp}}\frac{\tilde{T}_e}{\tilde{P}_e} - \frac{f}{2D_{tp}}\frac{u^3}{|u|} \tag{4.25}$$

Using the relation $\dot{m}_e = \rho_e u A_e$, Z_e/ρ_0 in Equations (4.12) and (4.13) could be then expressed as:

$$\frac{Z_e}{\rho_0} = u\frac{\tilde{P}_e}{\tilde{T}_e}\frac{1}{L_{c2}} \tag{4.26}$$

where L_{c2} is a second characteristic length and is identified as the ratio of combustor volume to the tailpipe cross-section area, which is:

$$L_{c2} = \frac{V_c}{A_e}$$

Further effort is expended on analysis of the combustion zone exit pressure P_e and exit temperature T_e, which are related to the combustion pressure P and temperature T by isentropic process. Here it is assumed that the process changes from P and T to P_e and T_e via an adiabatic reversible process [120]. For an adiabatic constant-entropy (isentropic) process:

$$\begin{cases} PV^{\gamma} = constant \\ TV^{\gamma-1} = constant \end{cases} \tag{4.27}$$

The diameter of the combustor is regarded as much larger than that of the tailpipe. Hence, the adiabatic isentropic process from P and T to P_e and T_e is started with the velocity u_c (using subscript c for the state variables in the combustor), 0, to the velocity u at the tailpipe. With the assumption that the mass flow in the cross section of the control volume is constant, the following equation is derived [113]:

$$\frac{\gamma}{\gamma-1}RT_e+\frac{1}{2}u^2=\frac{\gamma}{\gamma-1}RT \tag{4.28}$$

Normalizing the temperature T_e with the ambient temperature T_0, it is obtained that:

$$\widetilde{T}_e=\widetilde{T}+\frac{(1-\gamma)u^2}{2\gamma RT_0} \tag{4.29}$$

For pressure P_e, it is:

$$\widetilde{P}_e=\widetilde{P}\left(\frac{2\gamma RT_0\widetilde{T}}{2\gamma RT_0\widetilde{T}+(1-\gamma)u^2}\right)^{\frac{\gamma}{1-\gamma}} \tag{4.30}$$

Thus, the simulation of the combustor model is achieved by simultaneous solutions of the differential Equations (4.12), (4.13), (4.17), (4.19) and (4.24), that is:

$$\begin{cases}
\dfrac{d\widetilde{T}}{dt}=\left(\dfrac{1}{\tau_f}+\dfrac{1}{\tau_{HT}}+\dfrac{1}{\tau_c}\right)\dfrac{\gamma\widetilde{T}}{\widetilde{P}}-\left((\gamma-1)\dfrac{Z_e}{\rho_0}+\dfrac{1}{\tau_f}+\dfrac{\gamma T_0}{\tau_{HT}T_w}\right)\dfrac{\widetilde{T}^2}{\widetilde{P}} \\
\dfrac{d\widetilde{P}}{dt}=\left(\dfrac{1}{\tau_f}+\dfrac{1}{\tau_{HT}}+\dfrac{1}{\tau_c}-\left(\dfrac{Z_e}{\rho_0}-\dfrac{T_0}{\tau_{HT}T_w}\right)\widetilde{T}\right)\gamma \\
\dfrac{dY_f}{dt}=(Y_{f,i}-Y_f)\dfrac{\widetilde{T}}{\widetilde{P}}\dfrac{1}{\tau_f}-\dfrac{\widetilde{T}}{\widetilde{P}}\left(\dfrac{C_pT_0}{\Delta H_f}\right)\dfrac{1}{\tau_c} \\
\dfrac{dY_o}{dt}=(Y_{o,i}-Y_o)\dfrac{\widetilde{T}}{\widetilde{P}}\dfrac{1}{\tau_f}-S_r\dfrac{\widetilde{T}}{\widetilde{P}}\left(\dfrac{C_pT_0}{\Delta H_f}\right)\dfrac{1}{\tau_c} \\
\dfrac{du}{dt}=(\widetilde{P}_e-1)\dfrac{RT_0}{L_{tp}}\dfrac{\widetilde{T}_e}{\widetilde{P}_e}-\dfrac{f}{2D_{tp}}\dfrac{u^3}{|u|}
\end{cases} \tag{4.31}$$

The definitions Equations (4.22), (4.26), (4.29) and (4.30) are needed to relate the various equations. The solution of the equations above gives the pressure, temperature, fuel mass fraction and oxygen mass fraction in combustion chamber and velocity in the tailpipe. The pressure and temperature at the tailpipe entrance are related to the pressure and temperature in the combustion chamber by the adiabatic isentropic process.

4.2.5 Equation Solution and Initial Conditions

The governing equations are solved with a fourth-order Runge-Kutta scheme [129]. In the simulation programs, a time step decrement/increment method is employed in order to achieve the compromise between speed and accuracy of the calculation. A time-step decrement is performed when the temperature, pressure or velocity is changed rapidly. This decrement is followed by a time-step increment when these changes are moderate.

The initial conditions are:

1) Initial temperature: $5 \times T_0$

2) Initial pressure: $1 \times P_0$

3) Initial velocity: 0.0

4) Friction factor: 0.03

The initial conditions correspond physically to filling the combustor with unburned fuel and air at ambient pressure with no exiting flow. Then, an absolute temperature of five times the ambient is used to ensure the temperature is high enough to initiate combustion. The initial pressure and temperature rise are over-predicted since there is no laboratory counterpart to mixing fuel and air at the dimensionless temperature of 5, and then suddenly allowing the reaction to start. However, the choice of initial conditions is investigated and the final solutions are not affected. This result would be expected on physical grounds since the dissipative nature of friction in the tailpipe should negate the history of start-up.

In the premixed model described in this section, stoichiometric conditions have been considered for simplicity. Two configurations for the flow of reactants have been adopted, which are a steady inlet and a sinusoidal inlet.

The steady inlet mass flow is firstly considered for the following simulation. The classic flame extinction/ignition boundaries and oscillating combustion are predicted. According to the measured pressure signal as shown in Figure 4.4 (a), the inlet mass flow can be modelled as a sinusoidal function:

$$\dot{m}_i = C_1 + C_2 \sin(2\pi\omega t + \theta) \tag{4.32}$$

where C_1 is the average value of the inlet mass flow, C_2 is the amplitude zero-maximum, ω is the angular frequency and θ is the initial phase. A theoretical comparison between these two inlet configurations is then conducted.

A steady inlet with a second sinusoidal mass flow is considered in this study. The mixed reactants, the air, and the fuel are used respectively as this second inlet mass flow to investigate the influence of the second mass flow on the pressure oscillations in the combustion zone. Finally, a simply PI controller is designed to attenuate the pressure instabilities with the steady inlet.

4.3 SIMULATION RESULTS OF PREMIXED COMBUSTOR MODEL

In Richards's simulation [108], the compressed air and gas is supplied into the combustion zone through an orifice entry port, by which the inlet stream driven by a high pressure is choked so that the inlet mass rate is constant throughout the cycle. For the combustor system investigated in this study, the mixing process of the inlet gases is more complex since the open air inlet (axial) configuration complicates the process. To simplify the simulation, it is assumed that the air and gas are well mixed before entering into the combustion zone. The combustor geometrical parameters are given in Table 4.1.

For comparing the experimental and simulation results, the FFT analysis [129-131] is undertaken to obtain the oscillating amplitude and frequency via Matlab [132, 133].

4.3.1 Premixed Combustor Model with Steady Supply of Reactants

In this section, the pressure and temperature are firstly predicted with different steady inlet mass flow rate. The influence of different combustion parameters on the pressure oscillations is then investigated.

4.3.1.1 Prediction of Pressure and Temperature

The pressure and the temperature are predicted for the premixed experimental combustor in lean conditions with steady inlet supply of the fuel and air. The simulation results are shown in Figure 4.5. The heat transfer process is predicted by fixing the wall temperature T_w at 1000 K and setting the heat transfer coefficient h at 120 W/m^{2}K. The friction coefficient f in the tailpipe is assumed as 0.03. The inlet mass flow $\dot{m}_i$ is set at 0.015 Kg/s. The equivalence ratio ϕ is firstly selected as 0.8.

As shown in Figure 4.5 (a), the initial pressure and temperature rise are caused by the initial conditions and the sudden occurrence of the reaction. However, the choice of initial conditions doesn't affect the final solutions. This result would be expected on physical grounds since the dissipative nature of the friction in the tailpipe should negate the history of the start up. About 0.4 s after start-up, the amplitude of the oscillation stabilizes. At this point, with an inlet mass flow of 0.015 Kg/s, the predicted amplitude of oscillation is approximately 12.6 kPa. The predicted frequency of the pressure oscillation is about 68 Hz, as shown in Figure 4.5 (b). As shown in Figure 4.4, the experimental measured pressure oscillation shows an amplitude of about 7.5 kPa with an oscillating frequency of about 75 Hz. The predicted amplitude and frequency of the oscillations are in reasonable agreement with measured results. The difference is considered to be primarily due to the steady inlet mass flow and difficulties in estimating the effective length of the tailpipe since the shape of the exhaust is simplified in the model.

The predicted phase shift between the heat release and the pressure is about 0.85 ms (22.1°) and does not modulate between cycles. Thus the Rayleigh criterion is satisfied and stable combustion oscillations are predicted [35].

As shown in Figure 4.6, stable oscillation amplitudes are observed when the inlet mass flow is set between 0.007 and 0.024 Kg/s with T_w=*1000K*, h=*120W/(m^{2}K)*, $\phi = 0.8$, and f=*0.03*. Compared with the amplitude of the temperature oscillation, the amplitude of the pressure oscillation is not so critically dependent on the inlet mass flow and there are not great changes within these inlet mass flow values. The frequency varies from 62.5 Hz to 75 Hz during the stable oscillation.

For the inlet mass flow below or above the limits of range 0.005~0.025 Kg/s, the extinction of the pulsations or a steady combustion condition is predicted, as shown in Figure 4.7.

After the gas and air in the combustion chamber are ignited, the sudden occurrence of the reaction will generate large heat release. This heat release will partly be taken out by exhaust products and the rest will mainly induce the initial pressure and temperature rise. The pressure rise will further drive the combustion products out to the exhaust, and there also exists similar trends towards the inlet. The smaller the inlet mass flow, the more obvious the trend to unstable combustion. At the same time, the temperature rise begins to decrease through the convection with the combustion chamber wall and via the products. Although the inertia of the moving gas column in the exhaust creates the negative pressure in the combustion zone allowing the fresh reactants to be drawn in through the inlet, there are still not enough reactants accumulating in the combustion chamber to sustain the continuous combustion process. Too much heat is also lost through the convective heat transfer and the exhaust, thus the flame will eventually die out and then extinction occurs (0.0008 Kg/s).

Increasing the inlet mass flow can help to overcome this effect and eventually it is possible to bring in enough volume of the fuel and air to sustain continuous combustion. If this process just happens before the temperature drops then sudden combustion will

greatly increase the pressure and temperature again. This cycle is repeated. Then pulse combustion occurs (0.005 Kg/s).

Continuously increasing the inlet mass flow, the reactants are sufficient to sustain the combustion process. After a certain time the temperature rise due to the heat release exceeds the temperature decrease due to the convection and the consumption by exhausted products, thus the temperature will finally increase. In the meantime, the heat release will also induce the pressure rise. The inhibition to the inlet mass flow is strengthened. The fuel and air needs more effort to enter into the combustion zone. Then, the reactants in the combustion zone start to decrease, so does the heat release. If the heat loss prevails, the temperature will begin to decrease. Then, oscillation combustion occurs (0.015 Kg/s).

When the value of the inlet mass flow is large enough, it could definitely overcome the negative influence from the pressure rise. The combustion process then reaches a steady combustion state (0.025 Kg/s).

Although no simulation is shown, the model will show that too large an inlet mass flow will blow out the flame in the combustion zone. Hence, the flame extinction will occur with too large an inlet mass flow, which is just like the blowing out of a candle flame in a strong wind.

Based on the simulation results, the combustion process could be classified into five types based on the increasing inlet mass flow, which are: Flame Extinction→Pulse Combustion→Oscillation Combustion→Steady Combustion→Flame Extinction.

4.3.1.2 Wall Temperature Effects

Figure 4.8 shows the predicted pressure and temperature with three different combustor wall temperatures, that is: 650K, 1000K, and 1100K. For lower value of the combustor wall temperature (650 K), the oscillation rapidly decreases in amplitude, which indicates the flame extinction. Similarly, steady combustion is shown with the higher combustor

wall temperature (1100 K), whilst for the intermediate combustor wall temperature (1000 K), steady oscillatory combustion is predicted.

At the higher combustor wall temperature (1100 K), the convective heat transfer between the combustor and the wall is lower. Hence, the temperature loss is smaller. The higher temperature in the combustor will increase the activity of the supplied inlet reactants, which will accelerate the reactant consumption. The faster reaction of the inlet reactants will thus remedy the loss of the pressure and temperature in the combustion zone. In the equilibrium state, the burned fuel is steadily replaced by the incoming fresh mixture, and steady combustion occurs, as shown in Figure 4.8 (a).

For the intermediate combustor wall temperature (1000 K), the convective heat transfer with the combustor wall is larger, which will induce the lower temperature in the combustion zone. This lower temperature will reduce the reaction rate. Thus it is possible to accumulate surplus reactants. The resulting excess of the reactants will result in more heat release as combustion occurs and compression of the mixture. The result is an increasing reaction followed by an increasing pressure, which will enhance the changes of the pressure and temperature in the combustion zone and makes it possible to satisfy the Rayleigh criterion. Hence, for the combustor wall temperature at 1000 K, steady oscillations are driven, as shown in Figure 4.8 (b).

When the combustor wall temperature decreases to a certain limit (650 K), the rapid convective heat transfer from the combustor wall will greatly reduce the temperature in the combustion zone. Once this temperature is lost further reaction cannot be sustained and the flame will die out, as shown in Figure 4.8 (c).

4.3.1.3 Heat Transfer Coefficient Effects

Clearly, the steady oscillation combustion occurs only when an adequate convective heat transfer rate with the control volume interface exists. Enhanced or diminished convective heat transfer will result in either flame extinction or steady combustion.

Figure 4.9 is a plot of the calculated temperature and pressure amplitudes as a function of the heat transfer coefficient h. Steady combustion occurs for h less than 105 W/m^{2}K. Above this value, combustion oscillations occur. The pressure amplitude is diminished with further increases in h, up to 245 W/m^{2}K, where heat loss is sufficient to extinguish the flame.

4.3.1.4 Tailpipe Fiction Effects

The simulation results show that the effect of friction in the tailpipe is very significant. Figure 4.10 compares the velocity and pressure with three different friction coefficients. Without friction ($f = 0$), the pressure amplitude is about 85 kPa, and the pressure curve has an abrupt change in its slope, which coincides with the transition of the tailpipe velocity between negative and positive. When the velocity in the tailpipe changes to negative from zero, the exhausted products begin to flow back to the combustor. The compression of the reactants in the combustion zone, as well as the heat brought back by the returning exhausted products, makes the pressure rise. On the contrary, when the velocity in the tailpipe is changed to positive from zero, the exhausted products begin to flow out to the tailpipe. The inertia of the moving gas column, as well as the heat loss taken by the exhausted products, makes the pressure decrease. With friction coefficients 0.02 and 0.04, the reverse flow is reduced and the pressure amplitudes are smaller, 23.82 kPa and 8.8 kPa respectively. At the higher friction coefficient 0.04, the velocity is negative for only a small portion of the cycle. The friction effect inhibits the exhausted products flow in or out of the combustor. Hence, the pressure curve does not show the immediate change in slope at the zero crossing and there exists time delays between them. Essentially the higher friction provides greater limitation to the gas velocity flowing in or out the combustor. This will reduce the variation in the temperature in the combustion zone and accordingly produce the decrease in pressure oscillation amplitude. Further increasing the friction coefficient to 0.05, the oscillation is replaced by steady combustion. In these cases, the pressure rise is a combination of the heat release and the changes of the velocity in the tailpipe.

4.3.1.5 Equivalence Ratio Effects

Figure 4.11 shows the predicted oscillation amplitudes of the pressure and temperature, frequency of oscillation, and the mean fuel mass fraction as a function of equivalence ratio with T_w=1000K, h=120W/(m^2K), f=0.03, and $\dot{m}_i = 0.02Kg/s$. As the equivalence ratio changes from 0.6 to 0.9, the oscillation amplitudes of the pressure and temperature increase to maximum values until the equivalence ratio is about 0.7, and then begin to decrease; the frequencies of the oscillation varies from 61 Hz to 76 Hz as the equivalence ratio increases.

4.3.2 Premixed Combustor Model with Variable Supply of Reactants

The original configuration of the combustor has an open-air inlet [111], which makes the mixing processes that govern the operation of the combustion system even more complicated. Not only is there interaction between heat release and the acoustic wave, but there is also interference between the inlet air flow and the acoustic flow.

As a first attempt to investigate the effect of the open-air inlet configuration, a modified premixed model is considered, in which only one inlet for both fuel and air mass flows is utilized.

In reality, the pressure in the air inlet pipe fluctuates around the atmospheric value, while the fuel inlet is driven by high upstream pressure [111]. Hence, in the model the pressure in the single inlet should fluctuate around a value slightly above atmospheric. The relationship of the inlet mass to the pressure in the inlet pipe will be considered later. Here, a simple parametrical expression is used.

Firstly, a sinusoidal supply (Equation (4.32)) is used to replace the steady inlet mass flow in the previous simulation. Then, a main steady flow combined with a second sinusoidal supply is studied to consider the influence of this second inlet mass flow on

the pressure oscillation. Finally, a simple PID controller is designed for steady inlet mass flow to accentuate the pressure oscillation.

4.3.2.1 Simulation with the Sinusoidal Supply Configuration

The sinusoidal inlet supply of the reactants can be expressed as:

$$\dot{m}_i = C_1 + C_2 \sin(2\pi\omega t + \theta)$$

The values of the parameters used for the equation are as follows:

C_1=0.033 Kg/s; C_2=0.0396 Kg/s; f=68 Hz; $\theta = 0^o$.

Considering that the frequencies and amplitudes of the inlet mass flow will couple with the ones in the combustor, a modification to the inlet flow is introduced to account for this feedback influence, in which the frequency of the inlet flow is adjusted to the internal frequency of oscillation at each time step.

The average value of the load is 0.033 Kg/s and the sinusoidal amplitude is 0.0396 Kg/s. This large sinusoidal load amplitude is to simulate the inlet back flow during the combustion process. Again the wall temperature T_w is set at 1000 K, the heat transfer coefficient h is at 120 W/(m^{2}K), and the friction factor f is at 0.03.

Figure 4.12 shows the predicted pressure and temperature oscillations. In the simulation, the frequency of the inlet flow as allowed to vary from 58 up to 84 Hz following the frequency of the pressure oscillations in the combustion chamber as discussed above. The predicted pressure curve is rather irregular, and the amplitudes of the oscillation vary from 9.5 to 49 kPa. The predicted temperature curve is also irregular.

As shown in Figure 4.12, the phase shift between temperature and pressure ranges from -1.467 ms to 1.33 ms for minimum and maximum cycles of the pressure amplitudes. Negative phase shift is equal to the large positive phase shift between the temperature

and the pressure. Hence, the updated model shows that the acoustic pressure oscillations re-excite when the phase shift between heat released from combustion and pressure oscillations reduces. Similarly, the pressure oscillations are weakened when the phase shift between temperature and pressure increases.

The phase shift appears to be the parameter that mostly affects the evolution of the oscillations and is considerably more influential than the absolute heat release during each cycle, which is to be expected via the Rayleigh criteria

4.3.2.2 Simulation with a Second Sinusoidal Supply Configuration

For combustion oscillation control purposes, simulations are run, in which the inlet mass flow is separated into two parts. One is distinguished as the main inlet mass flow, and the other is the second inlet mass flow. The main inlet mass flow is fixed at 0.02 Kg/s. The mixed reactants, air only, and fuel only are respectively used as the second inlet.

The second inlet mass flow is also modelled as a sinusoidal function, which is:

$$\dot{m}_{i,s} = C + C\sin(2\pi\omega t + \theta) \tag{4.33}$$

where C is the average value of the second inlet mass flow, ω is the angular frequency, and θ is the phase.

Figure 4.13 shows the oscillation pressure and temperature with the main steady inlet mass flow and the second sinusoidal inlet mass flow of mixed reactants, which has the same equivalence ratio as that of the main inlet mass flow. For $\dot{m}_{i,s}$, C is equal to 1.5 g/s, ω is 68 Hz, and θ is 0 rad. With this second inlet of mixed reactants, the oscillation amplitudes of the pressure vary from 10.5 kPa to 14.5 kPa, and the oscillation frequencies corresponding vary from 75 Hz to 73.1 Hz.

Figure 4.14 shows the maximum and minimum oscillation amplitudes of the pressure as function of the average value of the second inlet mass flow of mixed reactants C with

T_w=1000K, h=120W/(m^2K), f=0.03, $\dot{m}_i = 0.02\,Kg/s$ and $\phi = 0.8$. For $\dot{m}_{i,s}$, ω is 68 Hz and θ is 0 radians. With increase of the average value of the second inlet mass flow of mixed reactants, the maximum and minimum oscillation amplitudes decrease. However, the difference between the maximum and minimum oscillation amplitudes will increase. The simulation results show that the larger C will have a greater influence on the pressure oscillation.

Figure 4.15 shows the maximum and minimum oscillation amplitudes of the pressure as function of the average value of the second inlet mass flow of the fuel C with T_w=1000K, h=120W/(m^2K), f=0.03, and $\dot{m}_i = 0.02\,Kg/s$. For $\dot{m}_{i,s}$, ω is 68 Hz and θ is 0 radians. Injecting the fuel as the second inlet mass flow increases the equivalence ratio of the final mixed reactants. The average value of the second inlet mass flow of the fuel must be selected to avoid combustion with rich mixtures. In Figure 4.15, four different equivalence ratios in the main inlet mass flow are chosen, 0.9, 0.8, 0.7 and 0.6 respectively. The value of C is set to ensure the final equivalence ratio varies between the value in the main inlet mass flow and 1. The simulation results show that the smaller initial equivalence ratio in the main inlet mass flow allows increase to the larger second inlet mass flow of the fuel, thus has a significant effect on the oscillation pressure.

Figure 4.16 shows the maximum and minimum oscillation amplitudes of the pressure as function of the average value of the second inlet mass flow of the air C with T_w=1000K, h=120W/(m^2K), f=0.03, and $\dot{m}_i = 0.02\,Kg/s$. For $\dot{m}_{i,s}$, ω is 68 Hz and θ is 0 radians. Injecting the air as the second inlet mass flow decreases the equivalence ratio of the final mixed reactants. In Figure 4.16, three different equivalence ratios in the main inlet mass flow are chosen, which are 0.7, 0.8 and 0.9 respectively. The value of C is set to make the final equivalence ratio vary between the value in the main inlet mass flow and an approximate value of 0.6. The simulation results show that even if the value of C is very large (4.73 g/s), there is no evidence of change to the oscillation pressure.

From the simulation results above, it is not appropriate to select the air to be the second inlet mass flow. Even if a large average value of the inlet mass flow of the air is chosen, it is impossible to greatly change the pressure amplitude. When using fuel as the second inlet mass flow, its average value is dependent on the equivalence ratio in the main inlet

mass flow to ensure combustion under lean conditions. When the equivalence ratio in the main flow is smaller, it is thus sensible to use the fuel as the second inlet mass flow. The small injection of the fuel gives significant effects on the pressure oscillation. For the large equivalence ratios in the main inlet mass flow, the mixed reactants with the same equivalence ratio is appropriate.

4.3.3 A Simple PI Control for Steady Inlet Mass Flow

Unwanted combustion-induced pressure oscillations constitute a major technical problem in the development of high-performance propulsion systems as well industrial furnaces and power plants. Combustion instabilities induce many undesirable disturbances in the combustor and associated system. The combustion-induced pressure oscillations cause large mechanical vibrations in the system. The high-amplitude oscillations of the flow enhance the heat-transfer rate at the combustor wall. Combustion instabilities are generated by the resonant interaction between several different physical mechanisms. In general, they result from the coupling between the acoustic waves and flames.

The methods used to suppress combustion instabilities can be divided in two classes: passive and active control. In passive control techniques, modifications of the internal geometry of the combustion chamber are used to change the acoustic modes and propagation in order to prevent the resonant coupling. Designing passive control devices requires good physical understanding of the coupling mechanisms in the combustion chamber. Unfortunately the available theory seldom gives a detailed explanation of the complex phenomena involved, which makes the implementation of these techniques difficult and often limits their efficiency to a small frequency band. In contrast, active control techniques consist of injecting some external forcing disturbances into the combustor with an actuator, or adjusting the mass flow rate into the combustor to modify the pressure field to reach a stable operating condition.

As described in previous sections, stable oscillations can often result with certain steady inlet mass flows. Thus one control philosophy is to use PI control to adjust the inlet mass flow to make the combustion process stable.

Ziegler and Nichols give two methods to design PI controllers [134, 135]. In the second method, only proportional control action is used, as shown in Figure 4.17 (a). K_p is increased from 0 to a critical value K_{cr}, where the output first exhibits sustained oscillations. Thus, the critical gain K_{cr} and the corresponding period P_{cr} are experimental determined, as shown in Figure 4.17 (b). Ziegler and Nichols suggested that the values of the proportional gain K_p and integral time T_i are set according to the following equations, which are:

$$\begin{cases} K_p = 0.45K_{cr} \\ T_i = \dfrac{1}{1.2}P_{cr} \end{cases} \tag{4.34}$$

As shown in Figure 4.18 (a), when the combustor is given a steady inlet of reactants $\dot{m}_f$ equal to *0.02 Kg/s* with T_w=*1000K*, h=*120W/(m^{2}K)*, $\phi = 0.8$ and f=*0.03*, steady oscillations result. Hence, for PI controller design, the critical gain K_{cr} is equal to 1, and P_{cr} is just the oscillation period. The corresponding proportional gain K_p and integral time T_i are found as 0.45 and 0.0115 respectively. The designed PI controller is then embedded into the combustion system. Here, the ideal pressure level in the combustor is set as 1.03 bar.

Initially, the controller is off, and there is steady oscillation with the steady inlet mass flow. After 0.4 s, the controller is activated to attenuate the instability. The predicted pressure is then compared with the designed ideal output. The error between them is used by the PI controller to give variable control inputs to the combustor. The oscillatory pressure signal then decreases to a minimum level and the steady combustion process is realized.

4.4 DISCUSSION AND CONCLUSIONS

Thermo-acoustic combustion instabilities represent one of the main threats to modern combustors, as they involve pressure and heat release fluctuations characterised by large amplitudes and low frequencies. The coupling mechanism self-sustains oscillations and

causes the combustion process to become unstable, exciting the resonant acoustic modes of the combustion chamber. These combustion instabilities induce non-uniformity of exhausted gas temperature distribution, the growth of thermal-NO_x production, structure vibrations, increased heat transfer, roll torque, and sometimes, destruction of the burner.

Mathematical models can be very useful in developing understanding of the fundamental fluid dynamics, oscillation dynamics, combustion, heat transfer processes, and allow derivation of technologies to alleviate or eliminate the problem.

In this study, a premixed combustion model is designed based on the conservation laws to predict the pressure oscillations. Effects of friction in the combustor tailpipe, heat loss from the combustion zone and mass flow rate are investigated theoretically. With different inlet mass flow rate, the combustion process could be classified into five regimes based on variation of the inlet mass flow. These are: flame extinction, pulse combustion, oscillating combustion, steady combustion and flame extinction. The effects of wall temperature, heat transfer, equivalence ratio, tailpipe friction and length are also investigated. The predicted simulation results are compared with the experimental data. The laboratory observations confirm that the premixed combustor model can predict reasonably well the pressure instabilities. This forms the foundation for the establishment of more complicated models and for control of pressure oscillation.

Secondly, a sinusoidal supply (Equation (4.32)) is used to replace the steady inlet mass flow, which allows the reverse flow in the inlet. The frequency of the inlet supply is coupled to the frequency in the main combustor that induces a more stochastic oscillatory behaviour showing less similarity between temperature and pressure. Acoustic pressure oscillations are repeatedly excited and diminished from cycle to cycle as the phase-shift between heat released from combustion and pressure oscillation fluctuates.

Thirdly, a main flow with a second sinusoidal inlet supply is simulated to investigate the influence of this second mass flow on the pressure oscillations. The simulation results show that it is not appropriate to select the air as the second inlet mass flow. Even if the large average value of the inlet mass flow of the air is chosen, it is impossible to greatly change the pressure amplitude. When using fuel as the second inlet mass flow, its

average value is dependent on the equivalence ratio in the main inlet mass flow to ensure combustion stays in the lean conditions. When the equivalence ratio in the main flow is smaller, it's rational to use the fuel as the second inlet mass flow. This small injection of the fuel gives very significant changes to pressure amplitude. For higher equivalence ratios in the main inlet, mixed reactants with the same equivalence ratio is appropriate to give significant pressure amplitudes. Clearly equivalence ratio effects have a very considerable effect on the models.

Finally, a simple PI controller is designed for steady inlet mass flows, being based on the second of the Ziegler-Nichols rules. Initially the controller is switched off, and there is regular pressure oscillation with the steady inlet mass flow. At 0.4 s, the controller is activated to attenuate the instability. Under control, the predicted pressure is then compared with the designed ideal output. The error between them is sent to PI controller to give the variable control input the combustor, with which the pressure signal is converged to an ideal level and the steady combustion process is realized.

Although the inlet mass flow is variable rather than steady in reality, this simple simulation of PI control for combustion pressure instabilities still suggests that the pressure oscillation could be attenuated by varying the inlet mass flow rate. The simulation of a main flow with a second sinusoidal inlet supply also proves that small changes of the fuel or mixed reactant will induce large chances in pressure amplitudes. Possibly in the future artificial neural networks may be needed to firstly identify the dynamics of a combustion chamber before control methodologies are applied.

However this work is directed at producing models and simulation techniques which can give better insight into the fundamental processes occurring in oscillating/unstable combustors/combustion systems, whilst also developing control methodologies. Neural networks need considerable amounts of data for training and do not necessarily give significant information on the fundamental processes occurring in a system.

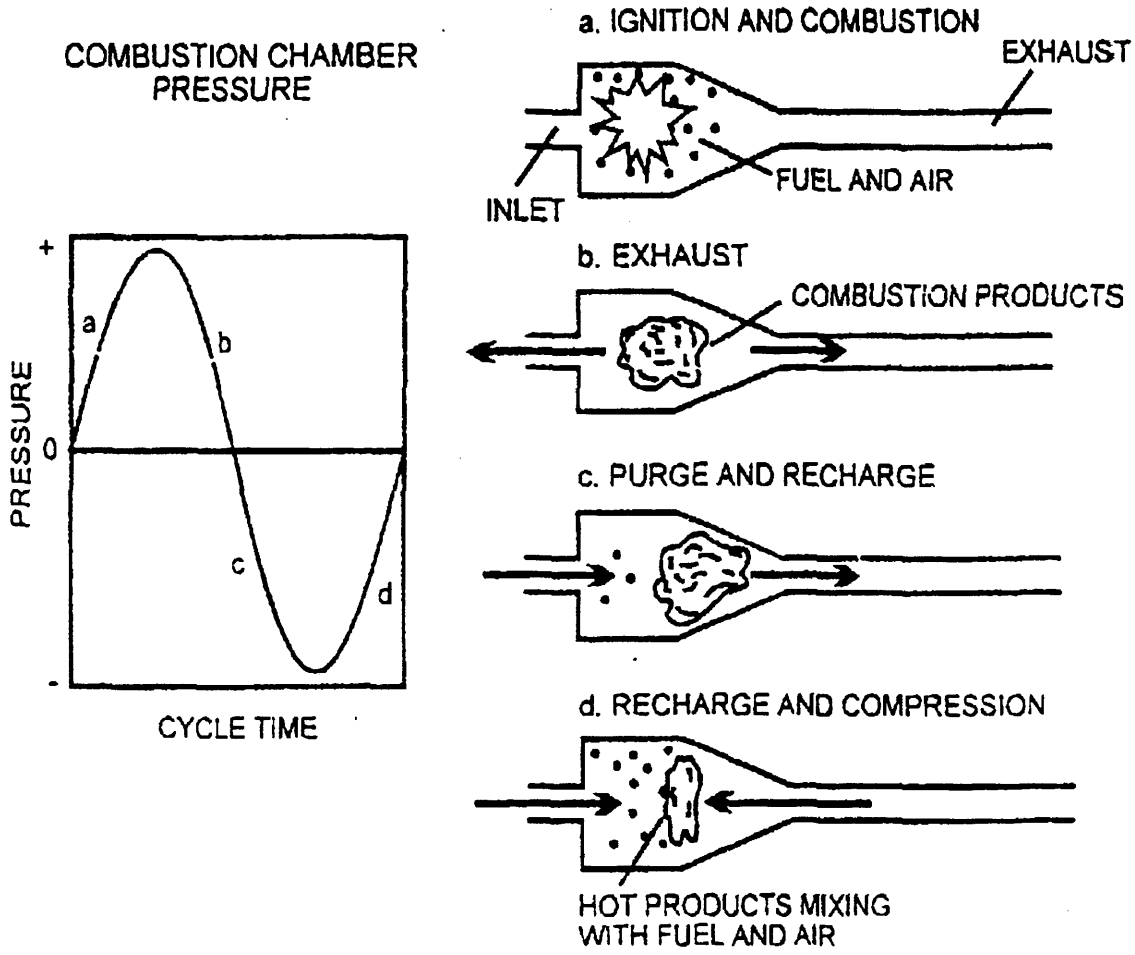

Figure 4.1: Basic Operation Cycle for a Simple Combustor

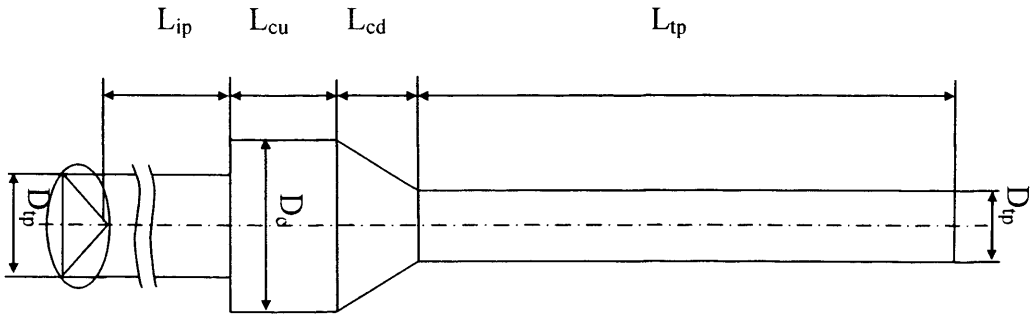

Figure 4.2: Schematic Layout of Experimental Combustor

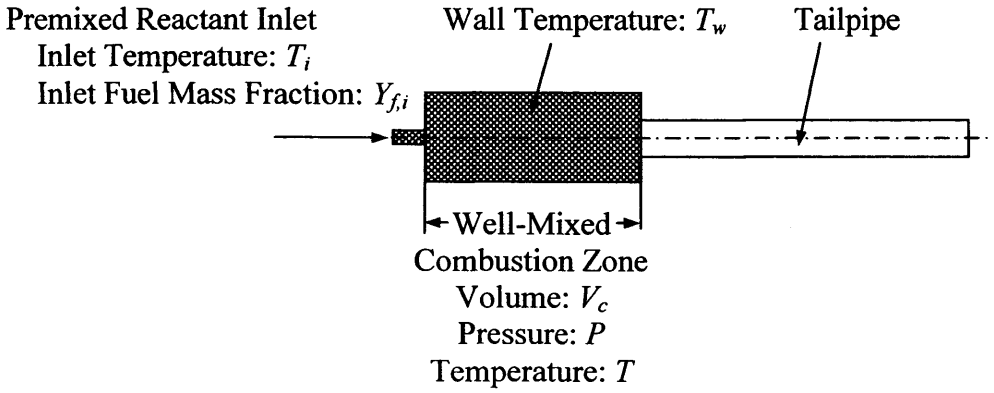

(a) Combustion Zone Geometry and Parameters

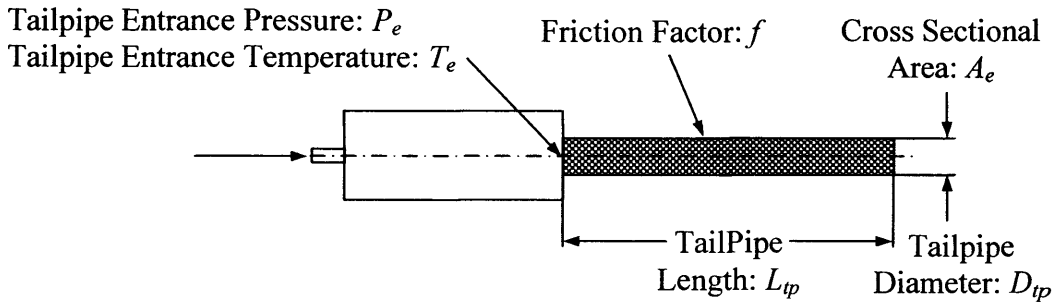

(b) Tailpipe Geometry and Parameters

Figure 4.3: Combustor Model Geometry and Parameters

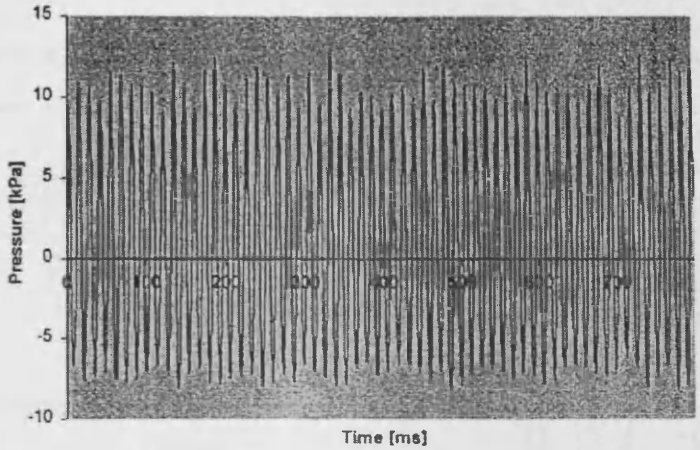

(a) Measured Pressure Oscillations in Combustion Chamber

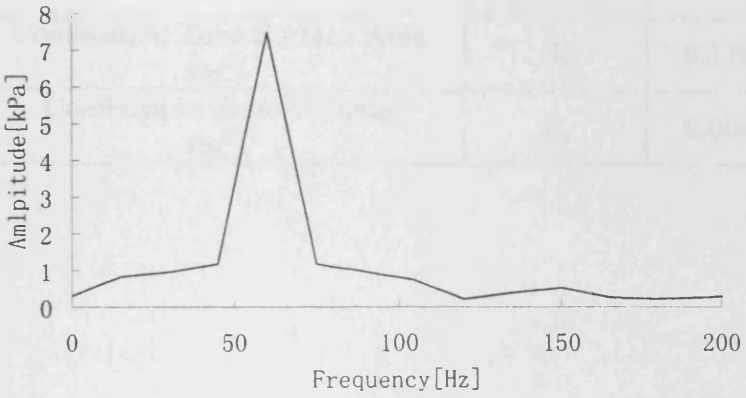

(b) FFT Analysis Result for Measured Pressure Oscillations in Combustion Chamber

Figure 4.4: Instantaneous Experimental Data of Pressure in the Combustion Chamber

Table 4.1 Geometric Conditions Employed in Combustion Model

Length (m)	L_{cu}	0.2
	L_{cd}	0.2
	L_{tp}	1.3
	L_{c1}	0.0278
	L_{c2}	2.53
Diameter (m)	D_c	0.15
	D_{tp}	0.05
Cross-section Area (m^2)	A_e	0.00196
Combustion Zone Surface Area (m^2)	A_s	0.17842
Combustion Zone Volume (m^3)	V_c	0.00496

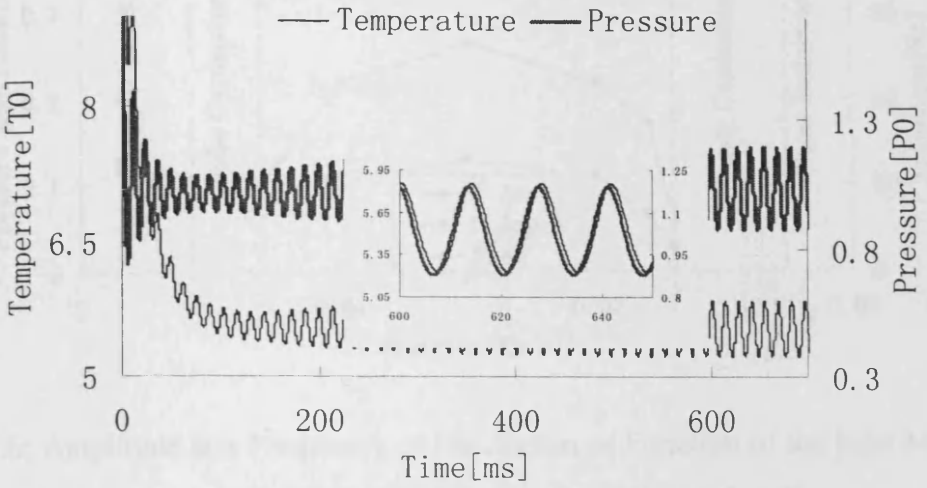

(a)

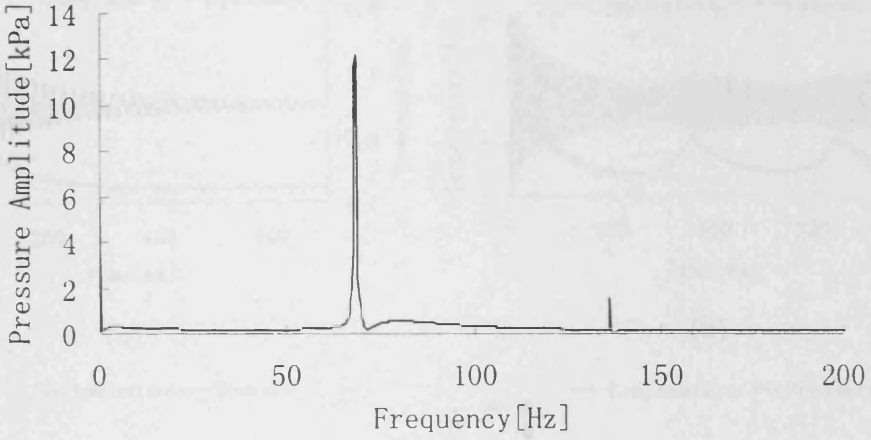

(b)

Figure 4.5: (a) Predicted pressure (thick line) and temperature (thin line) obtained with T_w=*1000K*, h=*120W/(m²K)*, $\phi = 0.8$, f=*0.03* and with a steady inlet of reactants $\dot{m}_i$ equal to *0.015Kg/s*. The close-up picture shows the phase between pressure and temperature; (b) FFT analysis result for pressure oscillation.

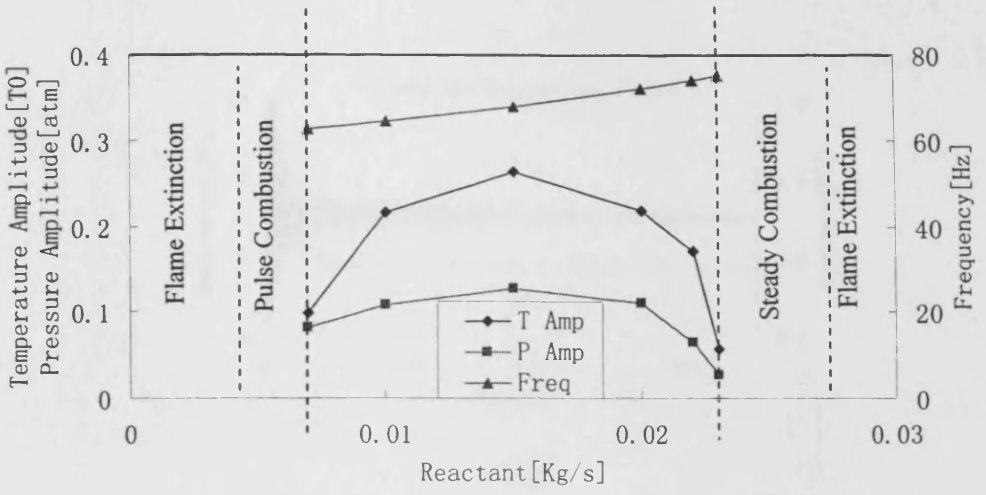

Figure 4.6: Amplitude and Frequency of Oscillation as Function of the Inlet Mass Flow of the Reactants with T_w=1000K, h=120W/(m^2K), ϕ = 0.8 and f=0.03.

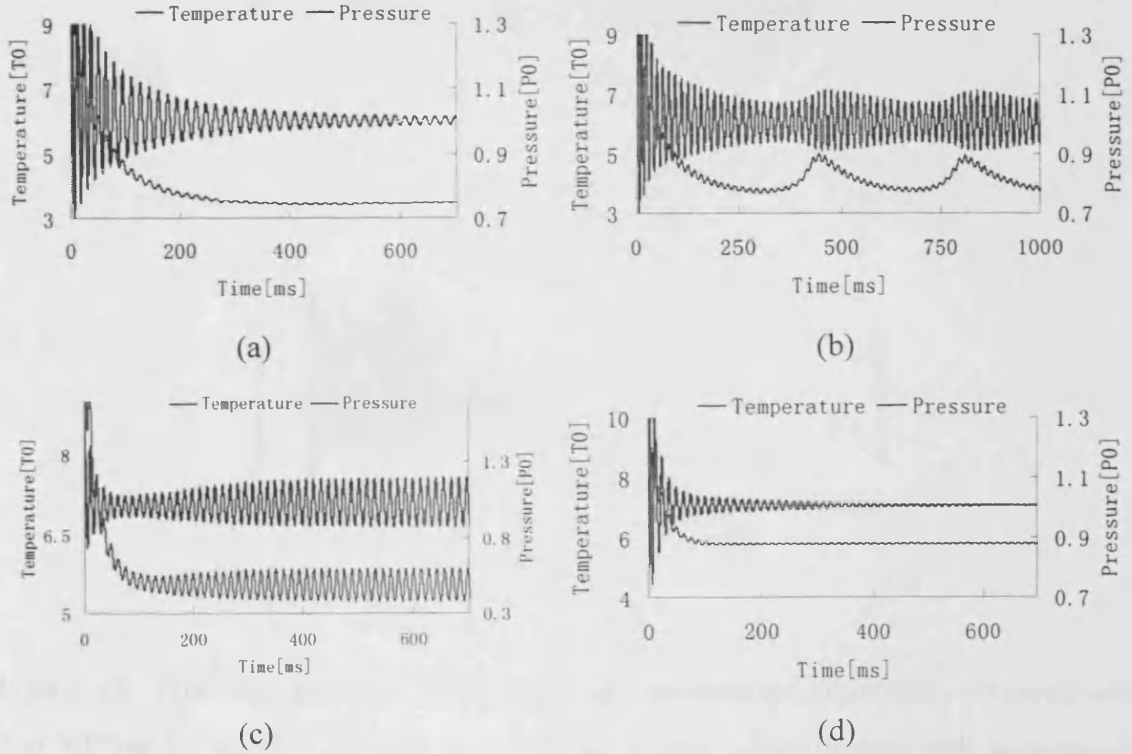

Figure 4.7: Predicted pressure (thick line) and temperature (thin line) obtained with T_w=1000K, h=120W/(m^2K), ϕ = 0.8, f=0.03 and with different steady inlet of reactants $\dot{m}_i$. (a) the inlet mass flow is 0.0008 Kg/s; (b) the inlet mass flow is 0.005 Kg/s; (c) the inlet mass flow is 0.015 Kg/s; (d) the inlet mass flow is 0.025 Kg/s.

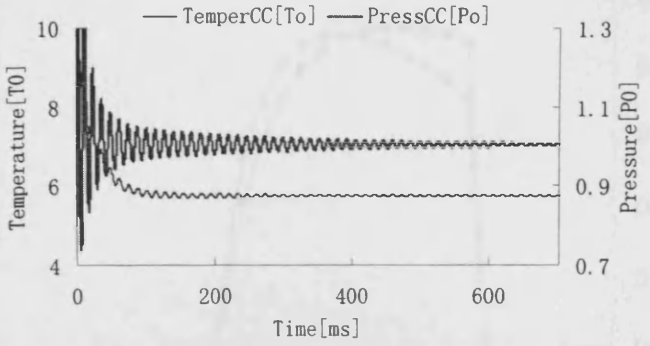

(a)

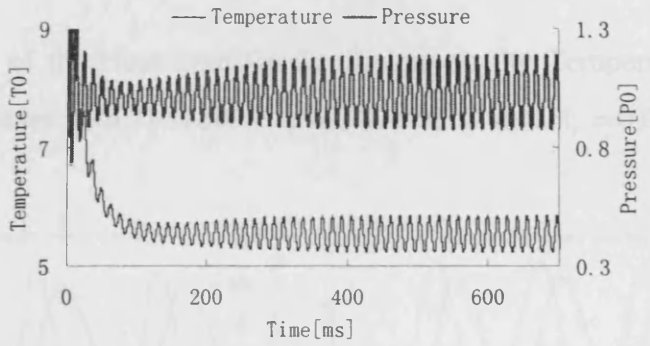

(b)

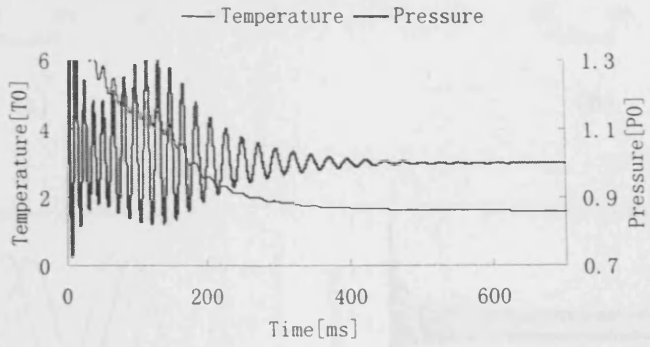

(c)

Figure 4.8: Predicted pressure (thick line) and temperature (thin line) obtained with $h=120W/(m^2K)$, $\phi = 0.8$, $f=0.03$, $\dot{m}_i = 0.02Kg/s$ and with different wall temperature T_w. (a) the wall temperature is 1100 K; (b) the wall temperature is 1000 K; (c) the wall temperature is 650 K.

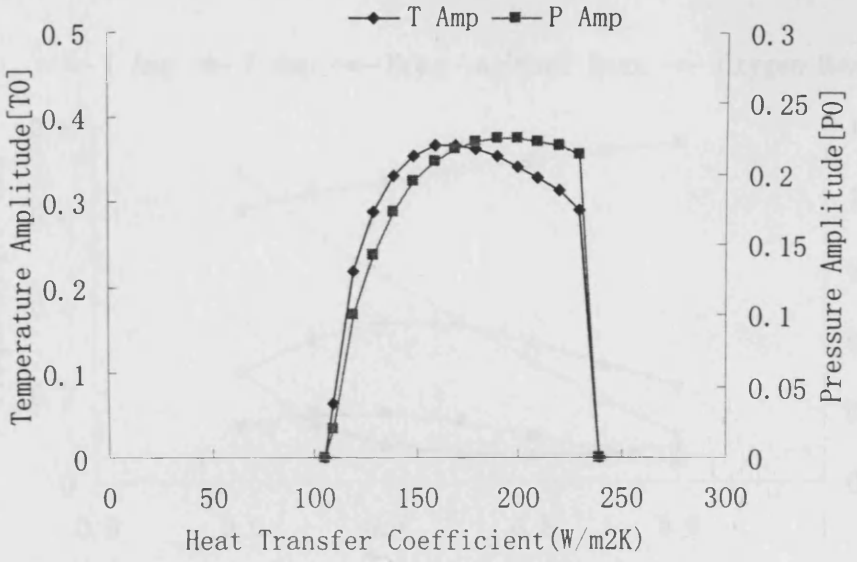

Figure 4.9: Effect of the Heat Transfer Coefficient on the Temperature and Pressure Oscillating Amplitudes with T_w=1000K, $\phi = 0.8$, f=0.03 and $\dot{m}_i = 0.02Kg/s$.

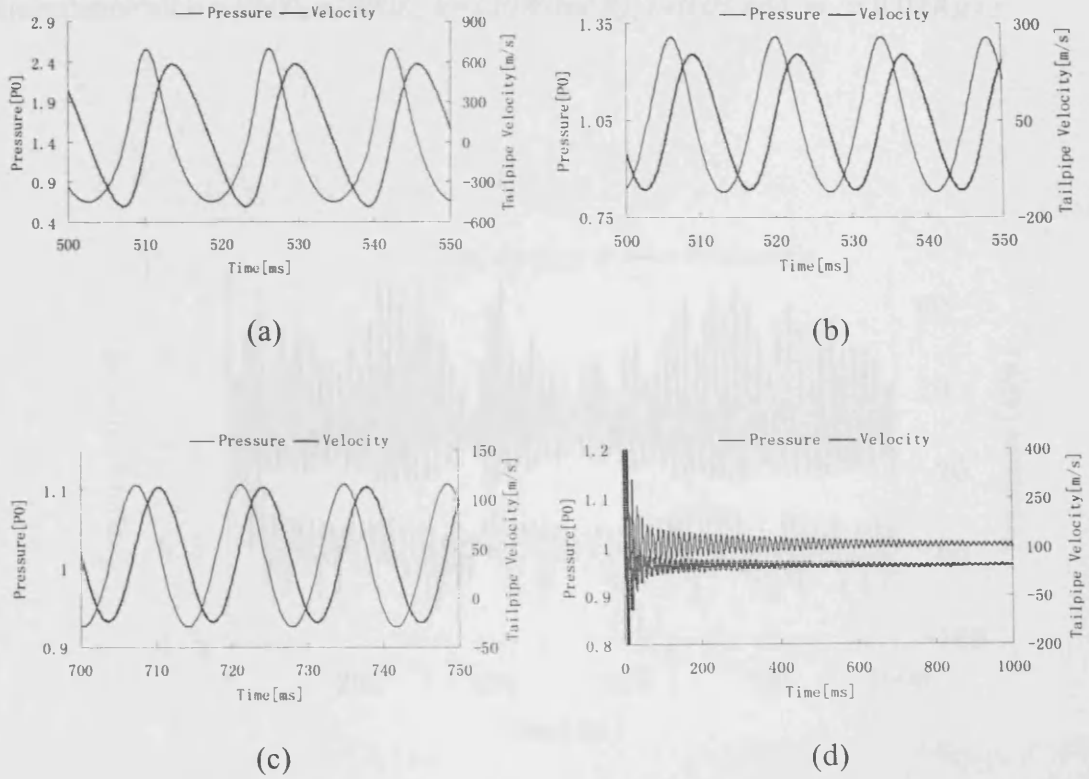

Figure 4.10: Predicted pressure (thin line) in combustion zone and velocity in tailpipe (thick line) obtained with T_w=1000K, h=120W/(m^{2}K), $\phi = 0.8$, $\dot{m}_i = 0.02Kg/s$ and with different friction coefficient f. (a) f is 0; (b) f is 0.02; (c) f is 0.04; (d) f is 0.05.

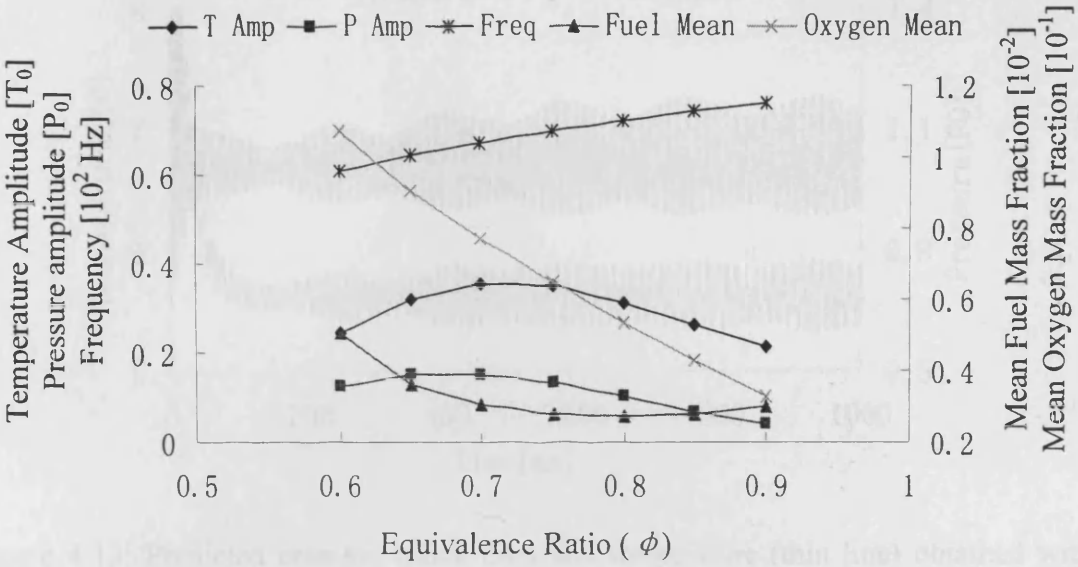

Figure 4.11: Oscillation amplitudes of the pressure and the temperature, frequency of oscillation, mean fuel mass fraction, and mean oxygen mass fraction as function of the equivalence ratio with T_w=*1000K*, *h=120W/(m²K)*, *f=0.03* and $\dot{m}_i = 0.02 Kg/s$.

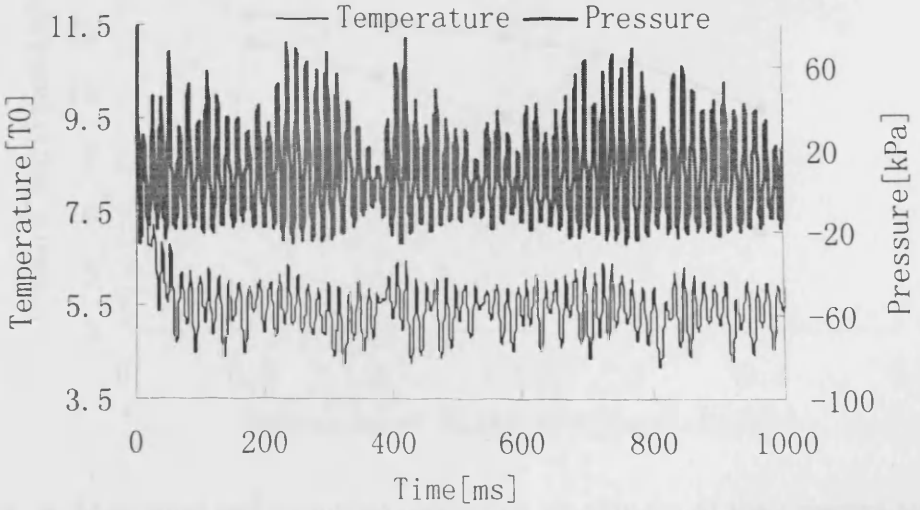

Figure 4.12: Predicted pressure and temperature oscillations with sinusoidal supply of reactants. In this simulation, the frequency of the inlet flow is related with a feedback mechanism to the frequency of the pressure oscillations in the combustion chamber.

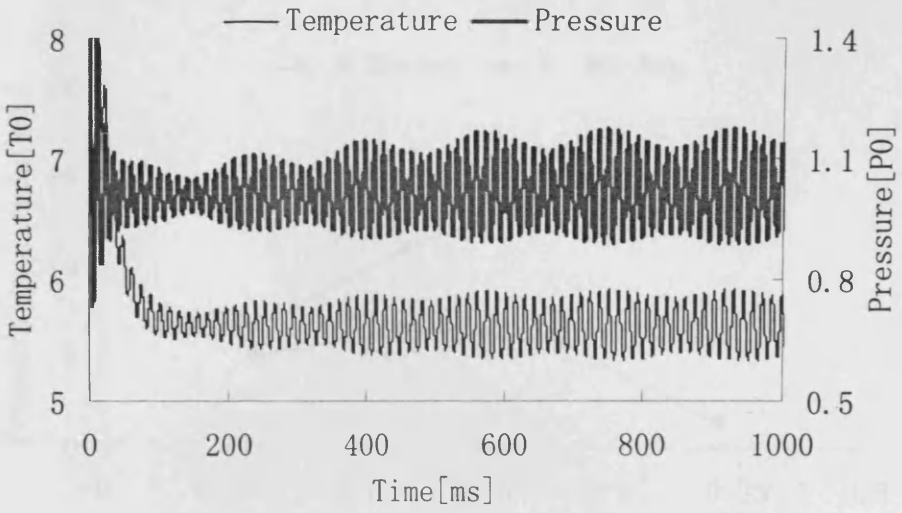

Figure 4.13: Predicted pressure (thick line) and temperature (thin line) obtained with T_w=1000K, h=120W/(m^2K), $\phi = 0.8$, f=0.03, main steady inlet of reactants $\dot{m}_i$ equal to 0.02Kg/s, and second sinusoidal inlet of mixed reactants $\dot{m}_{i,s}$ equal to $0.0015 + 0.0015\sin(2\pi \times 68t)$.

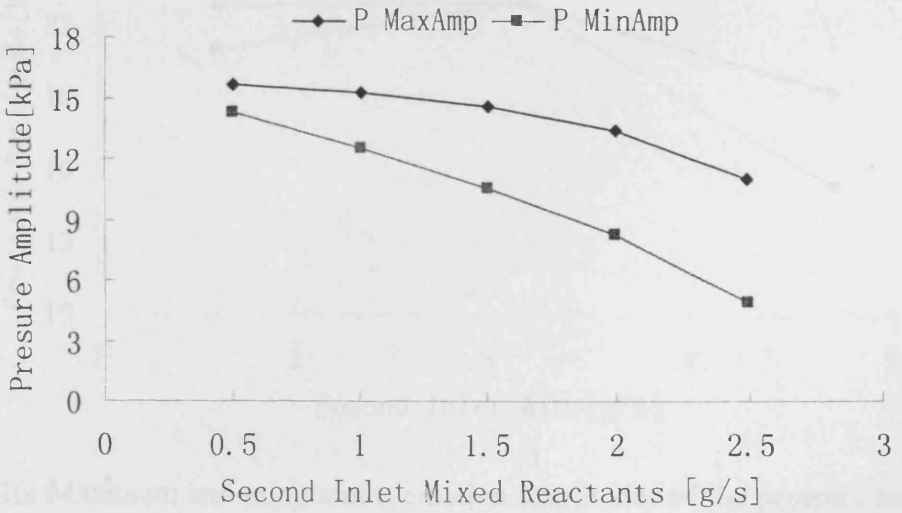

Figure 4.14: Maximum and minimum oscillation amplitudes of the pressure as function of the average value of the second inlet mass flow of mixed reactants C with T_w=1000K, h=120W/(m^2K), $\phi = 0.8$, f=0.03, and $\dot{m}_i = 0.02\,Kg/s$. For $\dot{m}_{i,s}$, ω is 68 Hz and θ is 0 rad.

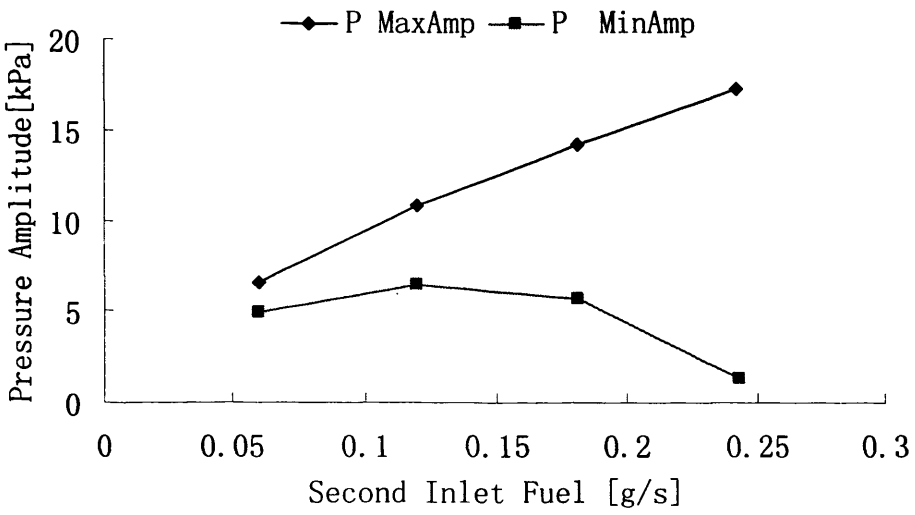

Figure 4.15: Maximum and minimum oscillation amplitudes of the pressure as function of the average value of the second inlet mass flow of the fuel C with T_w=*1000K*, h=*120W/(m²K)*, f=*0.03*, and $\dot{m}_i = 0.02\,Kg/s$. For $\dot{m}_{i,s}$, ω is 68 Hz and θ is 0 rad.

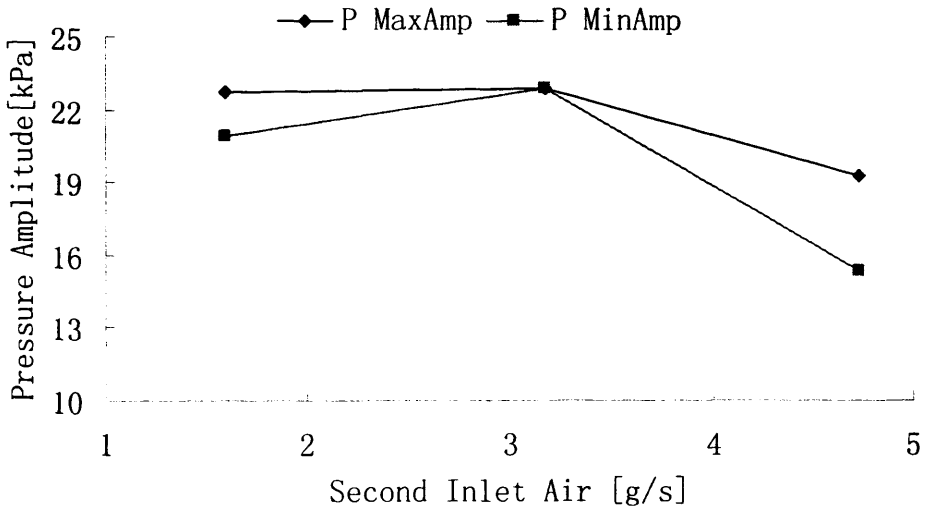

Figure 4.16: Maximum and minimum oscillation amplitudes of the pressure as function of the average value of the second inlet mass flow of the air C with T_w=*1000K*, h=*120W/(m²K)*, f=*0.03*, and $\dot{m}_i = 0.02\,Kg/s$. For $\dot{m}_{i,s}$, ω is 68 Hz and θ is 0 rad.

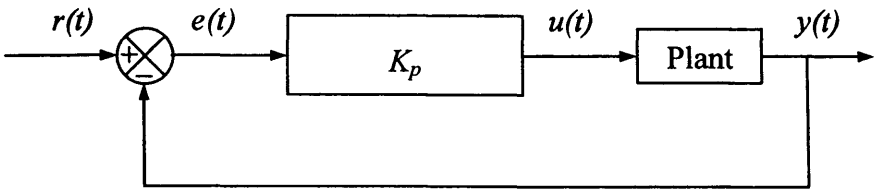

(a) Closed-loop System with a Proportional Action

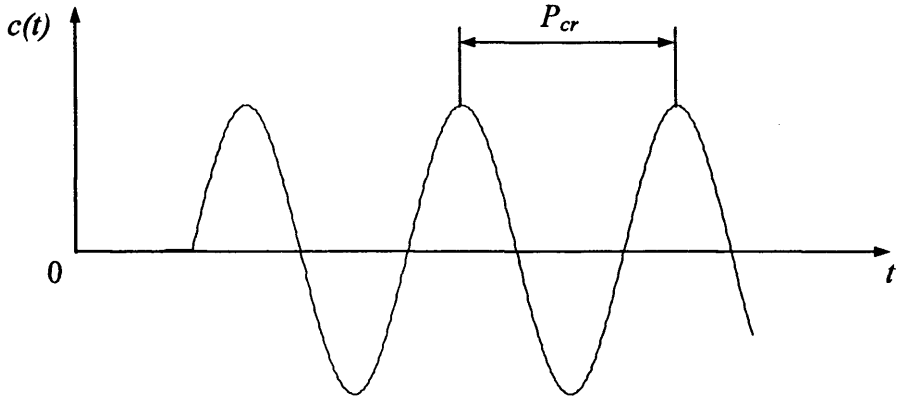

(b) Sustained Oscillation with Period P_{cr}

Figure 4.17: PI Controller Design by Ziegler-Nichols Rules

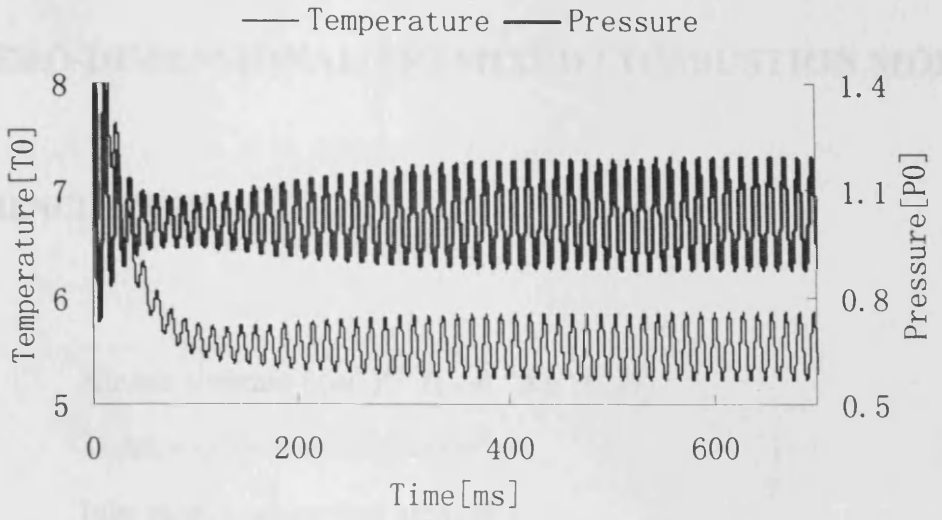

(a)

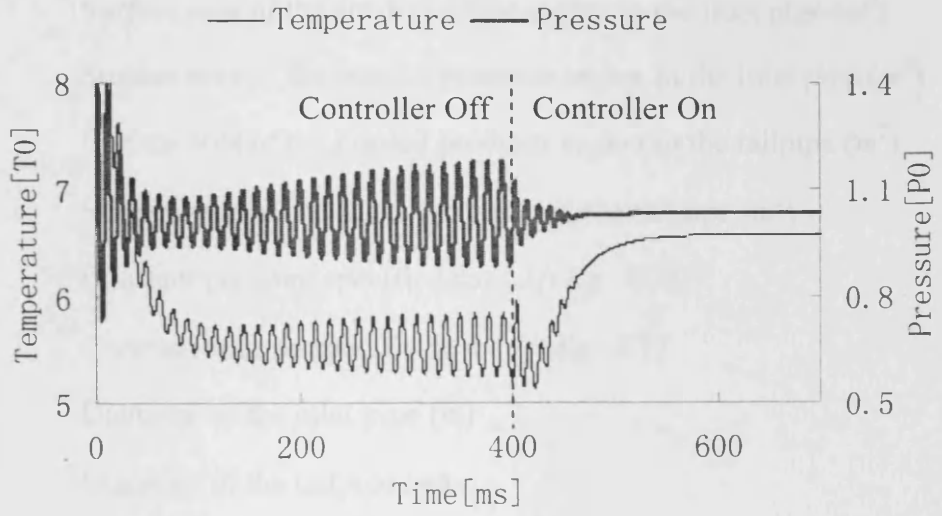

(b)

Figure 4.18: A simple PI control for steady inlet mass flow: (a) predicted pressure (thick line) and temperature (thin line) obtained with T_w=*1000K*, h=*120W/(m²K)*, $\phi = 0.8$, f=*0.03* and with a steady inlet of reactants $\dot{m}_i$ equal to *0.02 Kg/s*; (b) predicted pressure (thick line) and temperature (thin line) with PI control, in which the PI controller is on when time is 0.4 s.

5. ZERO-DIMENSIONAL PREMIXED COMBUSTION MODEL

NOMENCLATURE

A	Kinetic constant ($((m^3)^{n-1}/(\sqrt{K}\cdot Kg^{n-1}\cdot s))$)
A_e	Tailpipe cross-section area (m^2)
A_i	Inlet pipe cross-section area (m^2)
A_s	Surface area of the combustion zone (m^2)
A_{sia}	Surface area of the fresh reactant region in the inlet pipe (m^2)
A_{sib}	Surface area of the burned products region in the inlet pipe (m^2)
A_{stq}	Surface area of the burned products region in the tailpipe (m^2)
A_{str}	Surface area of the fresh air region in the tailpipe (m^2)
C_p	Constant pressure specific heat ($J/(Kg\cdot K)$)
C_v	Constant volume specific heat ($J/(Kg\cdot K)$)
D_{ip}	Diameter of the inlet pipe (m)
D_{tp}	Diameter of the tailpipe (m)
e	Specific internal energy (J/Kg)
e_a	Specific internal energy of the fresh reaction region in the inlet pipe (J/Kg)
e_b	Specific internal energy of the burned products region in the inlet pipe (J/Kg)
e_d	Specific internal energy of the tailpipe to the ambient surroundings (J/Kg)
e_e	Specific internal energy of the tailpipe exiting from the combustion zone (J/Kg)
e_i	Specific internal energy of the inlet to the combustion zone (J/Kg)
e_q	Specific internal energy of the burned products region in the tailpipe (J/Kg)
e_r	Specific internal energy of the fresh air region in the tailpipe (J/Kg)
e_u	Specific internal energy of the upstream in the inlet pipe (J/Kg)

E	Activation energy (*J/Kg* or *cal/mol*)
f	Friction coefficient
F_{fip}	Friction force on the contact surface between the flow and the inlet pipe (*N*)
F_{ftp}	Friction force on the contact surface between the flow and the tailpipe (*N*)
F_x	Force along *x*-direction (*N*)
h	Heat transfer coefficient ($W/(m^2 \cdot K)$)
L_a	Length of fresh reactant region in the inlet pipe (*m*)
L_b	Length of burned products region in then inlet pipe (*m*)
L_{c1}	First characteristic length (ratio of combustion zone volume V_c to surface area A_s) (*m*)
L_{c2}	Second characteristic length (ratio of combustion zone volume to tailpipe cross-section area A_e) (*m*)
L_{ip}	Length of the inlet pipe (*m*)
L_q	Length of burned products region in the tailpipe (*m*)
L_r	Length of fresh air region in the tailpipe (*m*)
L_{tp}	Length of the tailpipe (*m*)
$\dot{m}_d$	Exit mass flow rate from the tailpipe (*Kg/s*)
$\dot{m}_e$	Exit mass flow rate from the combustion zone (*Kg/s*)
$\dot{m}_i$	Inlet mass flow rate to the combustion zone (*Kg/s*)
$\dot{m}_u$	Upstream mass flow rate in the inlet pipe (*Kg/s*)
P	Pressure in combustion zone (*bar*)
$\widetilde{P}$	Pressure in the combustion zone normalized with the ambient pressure
P_0	Ambient pressure (*bar*)
P_a	Pressure in the fresh reactant region (*bar*)
P_b	Pressure in the burned products region (*bar*)
P_d	Pressure at the downstream position of the tailpipe (*bar*)
$\widetilde{P}_d$	Pressure at the downstream position of the tailpipe normalized with the ambient pressure
P_e	Pressure at tailpipe entrance (*bar*)

$\widetilde{P}_e$ Pressure at the tailpipe entrance normalized with the ambient pressure

P_i Inlet pressure to combustion zone (*bar*)

$\widetilde{P}_i$ Inlet pressure to combustion zone normalized with the ambient pressure

P_{ic} Pressure of the contact surface in the inlet pipe (*bar*)

P_q Pressure in the burned products region (*bar*)

P_r Pressure in the fresh air region (*bar*)

P_{tc} Pressure of the contact surface in the tailpipe (*bar*)

P_u Pressure at the upstream position of the inlet tube (*bar*)

$\widetilde{P}_u$ Pressure at the upstream position of the inlet tube normalized with the ambient pressure

$\overline{q}$ Heat transfer rate vector ($J/(m^2 \cdot s)$)

$\dot{Q}$ Heat release per unit volume ($J/(m^3 \cdot s)$)

R Gas constant ($J/(Kg \cdot K)$)

$\dot{R}_f$ Fuel reaction rate (per unit volume) ($Kg/(m^3 \cdot s)$)

S_r Stoichiometric mass ratio between fuel and oxygen

T Temperature in combustion zone (K)

$\widetilde{T}$ Temperature normalized with the ambient temperature

T_0 Ambient temperature (K)

T_a Temperature at the region *a* in inlet pipe (K)

$\widetilde{T}_a$ Temperature at the region *a* in inlet pipe normalized with the ambient temperature

T_b Temperature at the region *b* in inlet pipe (K)

$\widetilde{T}_b$ Temperature at the region *b* in inlet pipe normalized with the ambient temperature

T_d Temperature at the downstream position of the tailpipe (K)

$\widetilde{T}_d$ Temperature at the downstream position of the tailpipe normalized with the ambient temperature

T_e Temperature at tailpipe entrance (K)

$\widetilde{T}_e$ Temperature at the tailpipe entrance normalized with the ambient temperature

T_i Inlet temperature to combustion zone (K)

$\widetilde{T}_i$ Inlet temperature to combustion zone normalized with the ambient temperature

T_q Temperature at the region q in tailpipe (K)

$\widetilde{T}_q$ Temperature at the region q in tailpipe normalized with the ambient temperature

T_r Temperature at the region r in tailpipe (K)

$\widetilde{T}_r$ Temperature at the region r in inlet pipe normalized with the ambient temperature

T_u Temperature at the upstream position of the inlet tube (K)

$\widetilde{T}_u$ Temperature at the upstream position of the inlet tube normalized with the ambient temperature

T_w Wall temperature (K)

$\widetilde{T}_w$ Wall temperature normalized with the ambient temperature

u Velocity (m/s)

$\overline{u}$ Velocity vector (m/s)

u_{ip} Velocity of gas in the inlet pipe (m/s)

u_{tp} Velocity of gas in the tailpipe (m/s)

V_c Combustion zone volume (m^3)

Y_f Fuel mass fraction in the combustion zone

Y_{fb} Fuel mass fraction of the burned products region in the inlet pipe

Y_{fe} Fuel mass fraction from the exit of the combustion zone

Y_{fi} Inlet fuel mass fraction to the combustion zone

Y_{fq} Fuel mass fraction of the burned products region in the tailpipe

Y_{fu} Fuel mass fraction at position u

Y_o Oxygen mass fraction in the combustion zone

Y_{ob} Oxygen mass fraction of the burned products region in the inlet pipe

Y_{oe} Oxygen mass fraction from the exit of the combustion zone

Y_{oi} Inlet oxygen mass fraction to the combustion zone

Y_{oq} Oxygen mass fraction of the burned products region in the tailpipe

Y_{ou} Oxygen mass fraction at position u

Z_e Exit mass flow per combustion zone volume ($Kg/(m^3 \cdot s)$)

Z_i Inlet mass flow per combustion zone volume ($Kg/(m^3 \cdot s)$)

GREEK LETTERS

ΔH_f Heat of reaction (per unit fuel mass) (J/Kg)

ϕ Equivalence ratio

ρ Density in the combustion zone (Kg/m^3)

ρ_0 Ambient density (Kg/m^3)

ρ_a Density of the fresh reactant region in the inlet pipe (Kg/m^3)

ρ_b Density of the burned products region in the inlet pipe (Kg/m^3)

ρ_d Downstream density at the tailpipe (Kg/m^3)

ρ_e Density at the tailpipe entrance (Kg/m^3)

ρ_i Density at the inlet entrance of the combustion zone (Kg/m^3)

ρ_q Density of the burned products region in the tailpipe (Kg/m^3)

ρ_r Density of the fresh air region in the tailpipe (Kg/m^3)

ρ_u Upstream density at the inlet pipe (Kg/m^3)

γ Ratio of specific heat

τ_0 Shear stress of the reactant products along the tailpipe wall (N/m^2)

τ_{0ia} Shear stress of the fresh reactant region at the inlet pipe wall (N/m^2)

τ_{0ib} Shear stress of the burned products region at the inlet pipe wall (N/m^2)

τ_{0tq}	Shear stress of the burned products region at the tailpipe wall (N/m^2)
τ_{0tr}	Shear stress of the fresh air region at the tailpipe wall (N/m^2)
τ_c	Combustion time (s)
τ_e	Exit flow time (s)
τ_{HT}	Heat transfer time (s)
τ_i	Inlet flow time (s)

PREFIXES

m	Fractional reaction order in oxygen
n	Overall reaction order

SUFFIXES

cv	Control volume for combustion zone
f	Fuel
ipv	Control volume for inlet pipe zone
o	Oxygen
s	Control surface of the combustion zone
tpv	Control volume for tailpipe zone

5.1 INTRODUCTION

A combustion process is the core of numerous applications devoted to propulsion and power generation. One of the main problems affecting combustion is the birth and the growth of the oscillations of the flame-front heat release area and of the pressure field inside the combustion chamber. This phenomenon is called thermo-acoustic instability and is self-sustained when a phase coupling between the two oscillations exists, pumping energy to the resonant modes of the combustion chamber [85]. The knowledge of the dynamic evolution of continuous combustion processes affected by thermo-acoustic instability represents an important issue in view of the development of combustion systems characterised by compact size, high performance and low pollutant emissions as well as high flexibility to different operating conditions.

Beale [111] has highlighted the complex nature of operation for certain designs of pulsating combustor. The simple fuel inlet and the open air inlets of these naturally aspirating combustors generate a complex unsteady flow of reactants, which in turn varies the phase shift between heat release and acoustic pressure waves – the Rayleigh Phase [136], which results in irregularities in the oscillations such as amplitude modulations and cyclical frequency variations.

The premixed combustor model of the previous chapter generated predictions of characteristic variables such as frequency, pressure and temperature amplitude (referred to as primary variables hereafter). Furthermore, introducing a non-steady supply in the premixed inlet of the fuel/air induced variations of frequency with the cycles and accompanying modulations of amplitude.

In reality, the pressure in the air inlet pipe fluctuates around the atmospheric value, while the fuel inlet is driven by high upstream pressure as described by Beale [111]. Hence, in the model the pressure in the single inlet should fluctuate around a value slightly above atmospheric. However, relating the inlet mass flow to the pressure in the inlet pipe was not considered for the premixed combustor model in the previous chapter.

In this chapter, a zero-dimensional premixed combustion model is proposed. The essential features of the combustor geometry, combustion reaction rate and unsteady mixed reactants motion are accounted for. The governing equations presented identify key characteristic length and time scales, while the numerical simulation of the equations provides a relatively more efficient prediction of the combustion pressure oscillations. In addition, the pressure in the inlet pipe with a value slightly above atmospheric is considered.

5.2 COMBUSTION MODEL GEOMETRY AND EXPERIMENT RESULTS

The schematic layout of the experimental combustor is shown in Figure 5.1: it consists of an inlet pipe, combustion chamber and tailpipe. The combustor used is of the Helmholtz type.

For the premixed combustor model in the previous chapter, only the combustor and the tailpipe are considered. The integral of density in the tailpipe control volume is approximated as the product of the tailpipe entrance density ρ_e and the tailpipe volume. The simplified combustor model geometry is shown in Figure 4.3. In this chapter, a more complicated combustion model is considered, the geometry of which is shown in Figure 5.2. For reference, the positions u, i, e and d are identified with the upstream, inlet, exit and downstream locations. The combustion zone is defined as the region between position i and e, as shown in Figure 5.2 (a) of the shaded region. It is assumed that the combustion occurs only in this region, although the equations presented here can be modified to allow for combustion in the inlet and tailpipe regions as well. As shown in Figure 5.2 (b), the well mixed fresh reactant may be either drawn in or driven out through the inlet pipe. Similarly, the fresh air may be either drawn in or driven out through the tailpipe. It is assumed that the fresh reactant or air is separated from the burned combustion products by a contact surface, which moves through the inlet or tailpipe regions. The burned combustion products are shown as shaded regions composed of fuel, air and reactive products. Within the combustion zone, fuel and oxygen react at a rate controlled by a one-step Arrhenius kinetic mechanism. The

ambient pressure at the tailpipe exit is P_0. A constant friction factor f is specified along the inlet pipe and tailpipe length.

As described in the previous chapter, the pressure wave is measured using a fast responding piezo-electric pressure transducer, and the temperature is measured with fine wire thermocouples. Velocity measurements are carried out using Laser Doppler Anemometry [111].

The most important measurement to compare different operating conditions and burner configurations is that of pressure. The evaluation of the frequency and the pressure amplitudes shows the important features of the Helmholtz type combustor. Figure 4.4 (a) shows the experimental data of the oscillatory pressure in the combustion chamber. Figure 4.4 (b) shows the FFT analysis result for measured pressure oscillations (via Matlab), in which the oscillatory pressure amplitude is about 7.5 kPa, frequency about 75 Hz.

5.3 A ZERO-DIMENSIONAL COMBUSTION MODEL

Control volume conservation laws for each of the various regions are written next. The development that follows is similar to the one proposed in the previous chapter. The integral form of the conservations laws can also be referred to in Moody's literature [137]. Assuming uniform conditions within each region, the control volume and surface integrals are reduced to algebraic expressions, resulting in a set of first-order differential equations. Before modelling the combustion process, the following assumptions are employed:

1) The reactants are well mixed before entering the combustor, and the combustion occurs only in the combustion zone (between positions i and e).

2) A contact surface exists in the inlet pipe, which separates the fresh well-mixed reactants from the burned gases and moves within the inlet pipe. Similarly, a contact surface exists in the tailpipe, which separates the fresh air from the burned gases and moves within the tailpipe.

3) The inlet pipe is long enough to stop the burned products from the combustor returning through the inlet pipe and entering into the fresh reactant supply.

4) The combustion volume is considered as a homogeneous and isochoric zone, and ideal gas properties are used: $e=C_vT$, $C_p=C_v+R$, and $\gamma = \frac{C_p}{C_v}$.

5) Compared with the specific internal energy e, the contributions of the specific kinetic energy $u^2/2$ to the energy change in the combustion zone are negligible.

5.3.1 Conservation Equations in Combustion Zone

Based on the first law of thermodynamics, a control volume equation for energy conservation in the combustion zone is written as:

$$\frac{d}{dt}\int_{cv}\rho\left(e+\frac{1}{2}u^2\right)dV = \int_{cv}\dot{Q}dV - \oint_s\rho\left(e+\frac{1}{2}u^2\right)\bar{u}\cdot\bar{n}ds - \oint_s\bar{q}\cdot\bar{n}ds - \oint_s P\bar{u}\cdot\bar{n}ds \qquad (5.1)$$

As described in the previous chapter, the left side of this equation represents the rate of energy change of the system; while, the first item on the right side is the heat release rate due to combustion, the second is the net energy flow rate through the combustor surface, the third is the heat transfer rate with combustor wall, and the last is the rate of the net pressure work through the combustor surface. In equation (1), $u^2/2$ is the specific kinetic energy, $\bar{u}$ the velocity vector, $\bar{n}$ the unit vector, and $\bar{q}$ the heat transfer rate vector. The suffixes of the integral symbol cv and s represent the control volume and the control surface of the combustion zone respectively.

Assuming uniform conditions within each region, the volume and surface integrals are simplified to algebraic expressions, Equation (5.1):

$$\frac{V_c}{\gamma-1}\frac{dP}{dt} = C_p\left(T_i\dot{m}_i - T_e\dot{m}_e\right) + \dot{Q}V_c + hA_s\left(T_w - T\right) \tag{5.2}$$

Defining the following parameters:

1) Inlet mass flow per combustion zone volume

$$Z_i = \frac{\dot{m}_i}{V_c} \tag{5.3}$$

2) Exit mass flow per combustion zone volume

$$Z_e = \frac{\dot{m}_e}{V_c} \tag{5.4}$$

3) The first characteristic length (ratio of combustion zone volume to surface area A_s)

$$L_{c1} = \frac{V_c}{A_s} \tag{5.5}$$

The conservation of mass is:

$$\frac{d}{dt}\int_v \rho dV = -\oint \rho\bar{u}\cdot\bar{n}ds \tag{5.6}$$

which states that the mass change in the control volume is derived from the net mass flow through its control surface.

Employing similar assumptions as in Equation (5.2), Equation (5.6) for the combustion zone becomes:

$$\frac{d\rho}{dt} = Z_i - Z_e \tag{5.7}$$

By means of the ideal gas law, $\rho = \frac{P}{RT}$, Equation (5.7) becomes:

$$\frac{1}{RT}\frac{dP}{dt} - \frac{P}{RT^2}\frac{dT}{dt} = Z_i - Z_e \tag{5.8}$$

To simplify the resulting expression, the following characteristic times are defined:

1) Inlet flow time

$$\tau_i = \frac{\rho_o}{Z_i} \tag{5.9}$$

2) Exit flow time

$$\tau_e = \frac{\rho_o}{Z_e} \tag{5.10}$$

3) Heat transfer time

$$\tau_{HT} = \frac{L_{c1}\rho_0 R}{h} \tag{5.11}$$

4) Combustion time

$$\tau_c = \frac{\rho_0 C_p T_0}{\dot{Q}} \tag{5.12}$$

Note that the defined heat transfer is different from the one in previous chapter, this is mainly for the simplification of the following equations.

Referring to the definition of Z_i (Equation (5.2)), the inlet flow time is the mean residence time for non-reactive isothermal gas to pass through the combustion volume. τ_i does not correspond to a residence time in the reactive pulsating case, hence the

expression flow time is appropriately called "cold residence time" or "non-reactive residence time". The inlet and exit flow times are not constant and have negative values when the flow reverses in either the inlet pipe or the tailpipe; i.e., when the flow is moving from right to left at position *i* or *e*. For a constant heat transfer coefficient, the heat transfer time is constant. However, the combustion time is not a constant time scale, changing with the heat release rate.

Normalizing the temperature and pressure with the ambient temperature and pressure and denote them with a tilde, Equations (5.2) and (5.8) give:

$$\frac{d\widetilde{P}}{dt}=\gamma\left(\frac{\widetilde{T}_i}{\tau_i}-\frac{\widetilde{T}_e}{\tau_e}+\frac{1}{\tau_c}\right)+\frac{(\gamma-1)}{\tau_{HT}}\left(\widetilde{T}_w-\widetilde{T}\right) \tag{5.13}$$

and

$$\frac{d\widetilde{T}}{dt}=\left(\gamma\left(\frac{\widetilde{T}_i}{\tau_i}-\frac{\widetilde{T}_e}{\tau_e}+\frac{1}{\tau_c}\right)+\frac{(\gamma-1)}{\tau_{HT}}\left(\widetilde{T}_w-\widetilde{T}\right)\right)\frac{\widetilde{T}}{\widetilde{P}}-\left(\frac{1}{\tau_i}-\frac{1}{\tau_e}\right)\frac{\widetilde{T}^2}{\widetilde{P}} \tag{5.14}$$

The mass fractions of fuel and oxygen are determined from the conservation of species in the combustion zone. For fuel, it is:

$$\frac{d}{dt}\int_v \rho Y_f dV=-\oint_s \rho Y_f \bar{u}\cdot\bar{n}ds-\int_{cv}\dot{R}_f dV \tag{5.15}$$

which means that the rate of change of fuel mass is equal to the net fuel mass flow rate through the combustor surface subtracting the parts consumed in the combustion process.

With the same assumptions for deriving the Equation (5.2) from Equation (5.1), Equation (5.15) becomes:

$$\frac{d}{dt}\left(\rho Y_f V_c\right)=\dot{m}_i Y_{fi}-\dot{m}_e Y_{fe}-\dot{R}_f V_c \tag{5.16}$$

Hence, the resulting fuel mass fraction is:

$$\frac{dY_f}{dt} = (Y_{fi} - Y_f)\frac{\widetilde{T}}{\widetilde{P}}\frac{1}{\tau_i} - (Y_{fe} - Y_f)\frac{\widetilde{T}}{\widetilde{P}}\frac{1}{\tau_e} - \frac{\widetilde{T}}{\widetilde{P}}\left(\frac{C_p T_0}{\Delta H_f}\right)\frac{1}{\tau_c} \tag{5.17}$$

For oxygen, the formulation for conservation of species is:

$$\frac{d}{dt}\int_v \rho Y_o dV = -\oint_s \rho Y_o \bar{u}\cdot\bar{n}ds - \int_v S_r \dot{R}_f dV \tag{5.18}$$

With the same assumptions for deriving Equation (5.2) from Equation (5.1), Equation (5.18) becomes:

$$\frac{d}{dt}(\rho Y_o V_c) = \dot{m}_i Y_{oi} - \dot{m}_e Y_{oe} - \dot{R}_f V_c S_r \tag{5.19}$$

Hence, the resulting oxygen mass fraction is:

$$\frac{dY_o}{dt} = (Y_{oi} - Y_o)\frac{\widetilde{T}}{\widetilde{P}}\frac{1}{\tau_i} - (Y_{oe} - Y_o)\frac{\widetilde{T}}{\widetilde{P}}\frac{1}{\tau_e} - S_r\frac{\widetilde{T}}{\widetilde{P}}\left(\frac{C_p T_0}{\Delta H_f}\right)\frac{1}{\tau_c} \tag{5.20}$$

For Y_{fi}, when the velocity in the inlet pipe u_{ip} is positive (or zero), Y_{fi} is equal to Y_{fb} for positive L_b or Y_{fu} for zero L_b; when u_{ip} is negative, Y_{fi} is equal to Y_f. For Y_{fe}, when the velocity in the tailpipe u_{tp} is positive (or zero), Y_{fe} is equal to Y_f; when u_{tp} is negative, Y_{fe} is equal to Y_{fq} for positive L_q or 0 for zero L_q. There is a similar treated for Y_{oi} and Y_{oe}. That is:

when $u_{ip} \geq 0$, $Y_{fi} = \begin{cases} Y_{fb} & (L_b > 0) \\ Y_{fu} & (L_b = 0) \end{cases}$ and $Y_{oi} = \begin{cases} Y_{ob} & (L_b > 0) \\ Y_{ou} & (L_b = 0) \end{cases}$, or

when $u_{ip} < 0$, $Y_{fi} = Y_f$ and $Y_{oi} = Y_o$;

when $u_{tp} \geq 0$, $Y_{fe} = Y_f$ and $Y_{oe} = Y_o$, or

when $u_{tp} < 0$, $Y_{fe} = \begin{cases} Y_{fq} & (L_q > 0) \\ 0 & (L_q = 0) \end{cases}$ and $Y_{oe} = \begin{cases} Y_{oq} & (L_q > 0) \\ 0.232 & (L_q = 0) \end{cases}$.

Note that the oxygen mass fraction in the air is 0.232.

For solving the above equations an expression for combustion time τ_c needs to be developed. The instantaneous heat release (per unit volume) $\dot{Q}$ is the product of the heat of reaction (per unit fuel mass) ΔH_f and the fuel reaction rate (per unit volume) $\dot{R}_f$, that is:

$$\dot{Q} = \Delta H_f \dot{R}_f \tag{5.21}$$

The fuel used in the combustor is propane. Its ΔH_f value could be found in Rose's or Perry's Chemical Tables [122, 123].

A bi-molecular rate law is used to describe the fuel reaction rate, given by:

$$\dot{R}_f = A T^{1/2} \rho^n Y_o^m Y_f^{n-m} e^{-E/RT} \tag{5.22}$$

where A is the kinetic constant, Y_o the instantaneous oxygen mass fraction in the combustion zone, Y_f the instantaneous fuel mass fraction in the combustion zone, and E the activation energy; the prefix m is the fractional reaction order in oxygen, and n the reaction order.

The pressure and temperature at the inlet tube entrance (upstream position u) are expressed as P_u and T_u respectively, while the ambient pressure is P_0 and the ambient temperature is T_0.

Combining Equations (5.12), (5.21) and (5.22), the combustion time is then:

$$\frac{1}{\tau_c} = A\frac{\Delta H_f}{C_p}\frac{P_0^{n-1}}{R^{n-1}T_0^{n-0.5}}\frac{\widetilde{P}^n}{\widetilde{T}^{n-0.5}}Y_o^m Y_f^{n-m} e^{-\widetilde{T}_a/\widetilde{T}} \tag{5.23}$$

If it is assumed that the overall reaction order n is 2 and m is 1, then the Equation (5.23) becomes:

$$\frac{1}{\tau_c} = A'\frac{\Delta H_f}{C_p T_0}\frac{\widetilde{P}^2}{\widetilde{T}^{1.5}}Y_o Y_f e^{-\widetilde{T}_a/\widetilde{T}} \tag{5.24}$$

where A' is the product of the kinetic constant multiplied by various other model constants, and $\widetilde{T}_a$ is a dimensionless activation temperature.

Up to here, the models employing conservation equations for mass, species and energy in the combustion zone have been constructed. To complete the development, it is necessary to derive the equations for inlet pipe and tailpipe to determine the inlet mass rate $\dot{m}_i$ and exit mass flow rate $\dot{m}_e$.

5.3.2 Conservation Equations in Inlet Pipe

The gases in the inlet pipe are modelled as a slug flow with velocity u_{ip}. A contact surface might exist within this inlet pipe when the fresh well-mixed reactant is drawn from the upstream reservoir and flows to position i. Hence, the inlet pipe is divided into two regions: fresh reactant region 'a' and burned products region 'b'. Then the length between the position u and the contact surface is denoted as L_a. The motion of this contact surface is expressed as:

$$\frac{dL_a}{dt} = u_{ip} \tag{5.25}$$

which is valid when the regions a and b are all existing.

While for the length of burned products region in the inlet pipe L_b, it is:

$$L_b = L_{ip} - L_a \tag{5.26}$$

The regions on either side of the contact surface are characterized by a single value for all properties. The suffix '*a*' corresponds to fresh reactant drawn from the upstream of the inlet pipe, while the suffix '*b*' gives the properties of the burned products region. The combustion reaction is assumed to be quenched in the burned products region, and the concentrations of any residual fuel and oxygen are derived by the model. With the conservation of mass in the fresh reactant and burned products regions within the inlet pipe, the equations for densities are obtained.

For the density ρ_a in region *a* in the inlet pipe, it is:

$$\begin{cases} \dfrac{d\rho_a}{dt} = \dfrac{(\rho_u - \rho_i)}{L_{ip}} u_{ip} & L_a = L_{ip} \\ \dfrac{d\rho_a}{dt} = \dfrac{(\rho_u - \rho_a)}{L_a} u_{ip} & 0 < L_a < L_{ip} \end{cases} \tag{5.27}$$

For the density ρ_b in region *b* in the inlet pipe, it is:

$$\begin{cases} \dfrac{d\rho_b}{dt} = \dfrac{(\rho_u - \rho_i)}{L_{ip}} u_{ip} & L_b = L_{ip} \\ \dfrac{d\rho_b}{dt} = \dfrac{(\rho_b - \rho_i)}{L_b} u_{ip} & 0 < L_b < L_{ip} \end{cases} \tag{5.28}$$

The following is an overall momentum balance equation, which is used for the combined fresh reactants and burned products regions in the inlet pipe. The equation balances the change of the momentum for both regions as well as the corresponding pressure and friction forces acting on the slug of the fluid:

$$\sum F_x = \frac{d}{dt} \int_{pv} \rho u dV + \oint \rho u \bar{u} \cdot \bar{n} ds \tag{5.29}$$

The left side of the equation represents the sum of all forces acting in the axial direction on a control volume; while the first item on right side of the equation is the rate of change of momentum in the inlet pipe, and the second is the rate of change of the net momentum flow out of the inlet pipe in the same direction as the sum of all forces.

The sum of all forces includes the pressure on each side of the inlet pipe and the friction force F_{fip} on the contact surface between the flow and the inlet pipe.

Hence, Equation (5.29) becomes:

$$(P_u - P_i)A_i + F_{fip} = \frac{du_{ip}}{dt}\int_{pv}\rho dV + u_{ip}\left(\frac{d}{dt}\int_{pv}\rho dV + \oint\rho\bar{u}\cdot\bar{n}ds\right) \tag{5.30}$$

The integral of density in the inlet pipe is the combination of the fresh reactant and burned products regions. It is also noticed that the term in brackets on the right side is zero according to the overall conservation of mass in inlet pipe, that is:

$$\frac{d}{dt}\int_{pv}\rho dV + \oint\rho\bar{u}\cdot\bar{n}ds = 0$$

The friction force F_{fip} is developed from the wall shear stress in terms of the conventional friction coefficient f, as shown in Schlichting [114]. Using the instantaneous velocity of the inlet pipe in Schlichting's expression and considering the shear stress at the wall of the inlet pipe, it is shown that:

$$\begin{cases}\tau_{0ia} = \frac{1}{8}f\rho_a u_{ip}^2 \\ \tau_{0ib} = \frac{1}{8}f\rho_b u_{ip}^2\end{cases} \tag{5.31}$$

The friction forces of these two regions in the inlet pipe are then calculated by multiplying the wall shear stresses τ_{0ia} and τ_{0ib} by the surface areas A_{sia} and A_{sib}. The sign of the velocity needs to be considered for the direction of the force acting on the control volume. Performing these steps, Equation (5.30) becomes:

$$(\rho_a L_a + \rho_b L_b)\frac{du_{ip}}{dt} = (\tilde{P}_u - \tilde{P}_i)P_0 - \frac{f(\rho_a L_a + \rho_b L_b)}{2D_{ip}}\frac{u_{ip}^3}{|u_{ip}|} \tag{5.32}$$

In contrast to the overall momentum balance equation for the whole inlet pipe, the momentum balances applied to regions *a* and *b* are separately derived, which are:

$$\rho_a L_a \frac{du_{ip}}{dt} = (P_u - P_{ic}) - \frac{f\rho_a u_{ip}^3 A_{sia}}{8|u_{ip}|A_i} \tag{5.33}$$

and

$$\rho_b L_b \frac{du_{ip}}{dt} = (P_{ic} - P_i) - \frac{f\rho_b u_{ip}^3 A_{sib}}{8|u_{ip}|A_i} \tag{5.34}$$

When the region *b* does not exist, the P_{ic} in Equations (5.33) and (5.34) is equal to P_i; while, when the region *a* does not exist, the P_{ic} in Equations (5.33) and (5.34) is equal to P_u.

Similarly to the conservation of energy in Equation (5.1), the individual energy balance equations are developed for the fresh reactant and burned products regions. Note that the kinetic energy should not be ignored again and must be considered when deriving the energy balance equations in these two regions. Combining the Equations (5.27), (5.28), (5.33) and (5.34), the energy balance for each region in the inlet pipe could be obtained.

For the temperature T_a in region *a* in the inlet pipe, it is:

$$\begin{cases} \rho_a L_{ip} C_v \dfrac{d\tilde{T}_a}{dt} = \dfrac{C_v \dot{m}_u (\tilde{T}_u - \tilde{T}_a)}{A_i} - \dfrac{C_v \dot{m}_i (\tilde{T}_i - \tilde{T}_a)}{A_i} + \dfrac{f\rho_a u_{ip}^4 A_{sia}}{8|u_{ip}|A_i T_0} & L_a = L_{ip} \\ \rho_a L_a C_v \dfrac{d\tilde{T}_a}{dt} = \dfrac{C_v \dot{m}_u (\tilde{T}_u - \tilde{T}_a)}{A_i} + \dfrac{f\rho_a u_{ip}^4 A_{sia}}{8|u_{ip}|A_i T_0} & 0 < L_a < L_{ip} \end{cases} \tag{5.35}$$

For the temperature T_b in region *b* in the inlet pipe, it is:

$$\begin{cases} \rho_b L_{ip} C_v \dfrac{d\widetilde{T}_b}{dt} = \dfrac{C_v \dot{m}_u \left(\widetilde{T}_u - \widetilde{T}_b\right)}{A_i} - \dfrac{C_v \dot{m}_i \left(\widetilde{T}_i - \widetilde{T}_b\right)}{A_i} + \dfrac{f \rho_b u_{ip}^4 A_{sib}}{8 \left|u_{ip}\right| A_i T_0} & L_b = L_{ip} \\ \rho_b L_b C_v \dfrac{d\widetilde{T}_b}{dt} = \dfrac{C_v \dot{m}_i \left(\widetilde{T}_b - \widetilde{T}_i\right)}{A_i} + \dfrac{f \rho_b u_{ip}^4 A_{sib}}{8 \left|u_{ip}\right| A_i T_0} & 0 < L_b < L_{ip} \end{cases} \tag{5.36}$$

Assuming that the combustion reaction is quenched in the burned products region, the species conservation is then derived for fuel and oxygen within this region. Although the reaction is quenched, the species mass fractions could be varied by the changed boundary conditions, such as the one at position *i*. Combining the mass conservation equations, the species equations are obtained.

For the fuel mass fraction Y_{fb} in region *b* in the inlet pipe, it is:

$$\begin{cases} \rho_b L_{ip} \dfrac{dY_{fb}}{dt} = \dfrac{\dot{m}_u}{A_i}\left(Y_{fu} - Y_{fb}\right) - \dfrac{\dot{m}_i}{A_i}\left(Y_{fi} - Y_{fb}\right) & L_b = L_{ip} \\ \rho_b L_b \dfrac{dY_{fb}}{dt} = \dfrac{\dot{m}_i}{A_i}\left(Y_{fb} - Y_{fi}\right) & 0 < L_b < L_{ip} \end{cases} \tag{5.37}$$

For the oxygen mass fraction Y_{ob} in region *b* in the inlet pipe, it is:

$$\begin{cases} \rho_b L_{ip} \dfrac{dY_{ob}}{dt} = \dfrac{\dot{m}_u}{A_i}\left(Y_{ou} - Y_{ob}\right) - \dfrac{\dot{m}_i}{A_i}\left(Y_{oi} - Y_{ob}\right) & L_b = L_{ip} \\ \rho_b L_b \dfrac{dY_{ob}}{dt} = \dfrac{\dot{m}_i}{A_i}\left(Y_{ob} - Y_{oi}\right) & 0 < L_b < L_{ip} \end{cases} \tag{5.38}$$

Up to now, the models employing conservation equations for mass, species and energy in the inlet pipe zone have been considered. Similar methods will be used in the tailpipe zone.

5.3.3 Conservation Equations in Tailpipe

Equations (5.25)-(5.38) describe the behaviour of the species in the inlet pipe. A similar set of expressions can be applied to the tailpipe.

The gases in the tailpipe are modelled with velocity u_{tp}. A contact surface might exist within this tailpipe when the burned products are drawn from the combustion zone. Hence, the tailpipe is also divided into two regions: burned products region 'q' and fresh air region 'r'. Then the length between the position e and the contact surface is denoted as L_q. The motion of this contact surface is expressed as:

$$\frac{dL_q}{dt} = u_{tp} \tag{5.39}$$

which is valid when the regions q and r are all existing.

While for the length of fresh air region in the tailpipe L_r, it is:

$$L_r = L_{tp} - L_q \tag{5.40}$$

With the conservation of mass in the burned products and fresh air regions within the tailpipe, the equations for densities could be obtained.

For the density ρ_q in region q in the tailpipe, it is:

$$\begin{cases} \dfrac{d\rho_q}{dt} = \dfrac{(\rho_e - \rho_d)}{L_{tp}} u_{tp} & L_q = L_{tp} \\ \dfrac{d\rho_q}{dt} = \dfrac{(\rho_e - \rho_q)}{L_q} u_{tp} & 0 < L_q < L_{tp} \end{cases} \tag{5.41}$$

For the density ρ_r in region r in the tailpipe, it is:

$$\begin{cases} \dfrac{d\rho_r}{dt} = \dfrac{(\rho_e - \rho_d)}{L_{tp}} u_{tp} & L_r = L_{tp} \\ \dfrac{d\rho_r}{dt} = \dfrac{(\rho_r - \rho_d)}{L_r} u_{tp} & 0 < L_r < L_{tp} \end{cases} \tag{5.42}$$

The overall momentum balance equation within the tailpipe is:

$$(P_e - P_0)A_e + F_{ftp} = \frac{du_{tp}}{dt} \int_{pv} \rho dV \tag{5.43}$$

The friction force F_{ftp} is also developed from the wall shear stress in terms of the conventional friction coefficient f, as shown in Schlichting's text [114], which provides that:

$$\begin{cases} \tau_{0tq} = \dfrac{1}{8} f \rho_q u_{tp}^2 \\ \tau_{0tr} = \dfrac{1}{8} f \rho_r u_{tp}^2 \end{cases} \tag{5.44}$$

Hence the friction force F_{ftp} is calculated by multiplying the wall shear stresses τ_{0tq} and τ_{0tr} by the surface areas A_{stq} and A_{str}. The sign of the velocity is also needs to be considered for the direction of the force acting on the control volume. Performing these steps, Equation (5.43) becomes:

$$(\rho_q L_q + \rho_r L_r)\frac{du_{tp}}{dt} = (\tilde{P}_e - 1)P_0 - \frac{f(\rho_q L_q + \rho_r L_r)}{2D_{tp}} \frac{u_{tp}^3}{|u_{tp}|} \tag{5.45}$$

The momentum balances applied to regions q and r are separately derived, which are:

$$\rho_q L_q \frac{du_{tp}}{dt} = (P_e - P_{tc}) - \frac{f\rho_q u_{tp}^3 A_{stq}}{8|u_{tp}|A_e} \tag{5.46}$$

and

$$\rho_r L_r \frac{du_{tp}}{dt} = (P_{tc} - P_0) - \frac{f\rho_r u_{tp}^3 A_{str}}{8|u_{tp}|A_e} \tag{5.47}$$

When the region r does not exist, the P_{tc} in Equations (5.46) and (5.47) is equal to P_i, and when the region r is filled in the whole tailpipe, the P_{tc} is equal to P_e.

Combining the Equations (5.41), (5.42), (5.46) and (5.47), the energy balances for each region in the tailpipe are shown as follows.

For the temperature T_q in region q in the tailpipe, it is:

$$\begin{cases} \rho_q L_{tp} C_v \dfrac{d\tilde{T}_q}{dt} = \dfrac{C_v \dot{m}_e (\tilde{T}_e - \tilde{T}_q)}{A_e} - \dfrac{C_v \dot{m}_d (\tilde{T}_d - \tilde{T}_q)}{A_e} + \dfrac{f\rho_q u_{tp}^4 A_{stq}}{8|u_{tp}|A_e T_0} & L_q = L_{tp} \\ \rho_q L_q C_v \dfrac{d\tilde{T}_q}{dt} = \dfrac{C_v \dot{m}_e (\tilde{T}_e - \tilde{T}_q)}{A_e} + \dfrac{f\rho_q u_{tp}^4 A_{stq}}{8|u_{tp}|A_e T_0} & 0 < L_p < L_{tp} \end{cases} \tag{5.48}$$

For the temperature T_r in region r in the tailpipe, it is:

$$\begin{cases} \rho_r L_{tp} C_v \dfrac{d\tilde{T}_r}{dt} = \dfrac{C_v \dot{m}_e (\tilde{T}_e - \tilde{T}_r)}{A_e} - \dfrac{C_v \dot{m}_d (\tilde{T}_d - \tilde{T}_r)}{A_e} + \dfrac{f\rho_r u_{tp}^4 A_{str}}{8|u_{tp}|A_e T_0} & L_q = L_{tp} \\ \rho_r L_r C_v \dfrac{d\tilde{T}_r}{dt} = \dfrac{C_v \dot{m}_d (\tilde{T}_r - \tilde{T}_d)}{A_e} + \dfrac{f\rho_r u_{tp}^4 A_{str}}{8|u_{tp}|A_e T_0} & 0 < L_p < L_{tp} \end{cases} \tag{5.49}$$

Combining the mass conservation Equations (5.41) and (5.42), the species equations in the burned products region within the tailpipe are obtained.

For the fuel mass fraction Y_{fq} in region q in the tailpipe, it is:

$$\begin{cases} \rho_q L_{tp} \dfrac{dY_{fq}}{dt} = \dfrac{\dot{m}_e}{A_e}(Y_{fe} - Y_{fq}) - \dfrac{\dot{m}_d}{A_e}(Y_{fd} - Y_{fq}) & L_q = L_{tp} \\ \rho_q L_q \dfrac{dY_{fq}}{dt} = \dfrac{\dot{m}_e}{A_e}(Y_{fe} - Y_{fq}) & 0 < L_q < L_{tp} \end{cases} \tag{5.50}$$

For the oxygen mass fraction Y_{oq} in region q in the tailpipe, it is:

$$\begin{cases} \rho_q L_{tp} \dfrac{dY_{oq}}{dt} = \dfrac{\dot{m}_e}{A_e}\left(Y_{oe} - Y_{oq}\right) - \dfrac{\dot{m}_d}{A_e}\left(Y_{od} - Y_{oq}\right) & L_q = L_{tp} \\ \rho_q L_q \dfrac{dY_{oq}}{dt} = \dfrac{\dot{m}_e}{A_e}\left(Y_{oe} - Y_{oq}\right) & 0 < L_q < L_{tp} \end{cases} \tag{5.51}$$

Thus the Equations (5.39)-(5.51) describe the behaviour of the fluid in the tailpipe.

5.3.4 Equation Boundary Conditions

Further effort is needed to determine the boundary conditions for the whole combustion system.

The pressure in upstream position u, P_u, is always treated as constant, whilst the temperature T_u will depend on the direction of velocity in the inlet pipe. When $u_{ip}>0$, T_u is equal to ambient temperature T_0; when $u_{ip}<0$ and $L_a>0$, T_u is equal to T_a; and when $u_{ip}<0$ and $L_a=0$, T_u is equal to T_b.

The inlet pressure P_i, inlet temperature T_i, exit pressure P_e, and exit temperature T_e are related to the combustion pressure P and temperature T by the adiabatic isentropic process from the combustor into either pipe. Here it is assumed that the change process from P and T to P_i, P_e, T_i and T_e is an adiabatic reversible process. For an adiabatic constant-entropy (isentropic) process:

$$\begin{cases} PV^{\gamma} = constant \\ TV^{\gamma-1} = constant \end{cases} \tag{5.52}$$

The diameter of combustor is regarded as much larger than either pipe. Hence, the adiabatic isentropic process from P and T to P_i, P_e, T_i and T_e is started with the velocity u_c (using subscript c for the state variables in the combustor), 0, to the velocity u_{ip} at the inlet pipe and u_{tp} at the tailpipe. With the assumption that the mass flow in the cross section of the control volume is constant, the following equations are derived:

For inlet pipe, it is:

$$\frac{\gamma}{\gamma-1}RT_i+\frac{1}{2}u_{ip}^2=\frac{\gamma}{\gamma-1}RT \tag{5.53}$$

For tailpipe, it is:

$$\frac{\gamma}{\gamma-1}RT_e+\frac{1}{2}u_{tp}^2=\frac{\gamma}{\gamma-1}RT \tag{5.54}$$

Normalizing the temperature T_i and T_e with the ambient temperature T_0, Equations (5.53) and (5.54) become:

$$\widetilde{T}_i=\widetilde{T}+\frac{(1-\gamma)u_{ip}^2}{2\gamma RT_0} \tag{5.55}$$

and

$$\widetilde{T}_e=\widetilde{T}+\frac{(1-\gamma)u_{tp}^2}{2\gamma RT_0} \tag{5.56}$$

For pressure P_i and P_e :

$$\widetilde{P}_i=\widetilde{P}\left(\frac{2\gamma RT_0\widetilde{T}}{2\gamma RT_0\widetilde{T}+(1-\gamma)u_{ip}^2}\right)^{\frac{\gamma}{1-\gamma}} \tag{5.57}$$

and

$$\widetilde{P}_e=\widetilde{P}\left(\frac{2\gamma RT_0\widetilde{T}}{2\gamma RT_0\widetilde{T}+(1-\gamma)u_{tp}^2}\right)^{\frac{\gamma}{1-\gamma}} \tag{5.58}$$

The equations above are only suitable for the flow from the combustion zone to either pipe. For the flow into the combustion zone from either pipe, it is assumed that the fluid enters the combustion zone at the combustor pressure, whilst the temperature T_i is equal to T_a for $L_a=L_{ip}$ or T_b for $L_b>0$. A similar treatment is used for T_e.

When $u_{tp}>0$, the pressure P_d in position d is P_0 (ambient pressure), and the temperature T_d is equal to T_q for $L_q=L_{tp}$ or T_r for $L_r>0$; when $u_{tp}<0$, P_d and T_d are calculated just like equations (5.55)-(5.58):

$$\widetilde{T}_d = 1+\frac{(1-\gamma)u_{tp}^2}{2\gamma RT_0} \tag{5.59}$$

and

$$\widetilde{P}_d = \left(\frac{2\gamma RT_0}{2\gamma RT_0+(1-\gamma)u_{tp}^2}\right)^{\frac{\gamma}{1-\gamma}} \tag{5.60}$$

Thus, the simulation of the combustion model is achieved by simultaneous solutions of the differential equations in the combustor, inlet pipe and tailpipe. These are summarized as follows:

for combustor, the required differential equations are:

$$\frac{d\widetilde{P}}{dt} = \gamma\left(\frac{\widetilde{T}_i}{\tau_i}-\frac{\widetilde{T}_e}{\tau_e}+\frac{1}{\tau_c}\right)+\frac{(\gamma-1)}{\tau_{HT}}\left(\widetilde{T}_w-\widetilde{T}\right)$$

$$\frac{d\widetilde{T}}{dt} = \left(\gamma\left(\frac{\widetilde{T}_i}{\tau_i}-\frac{\widetilde{T}_e}{\tau_e}+\frac{1}{\tau_c}\right)+\frac{(\gamma-1)}{\tau_{HT}}\left(\widetilde{T}_w-\widetilde{T}\right)\right)\frac{\widetilde{T}}{\widetilde{P}}-\left(\frac{1}{\tau_i}-\frac{1}{\tau_e}\right)\frac{\widetilde{T}^2}{\widetilde{P}}$$

$$\frac{dY_f}{dt} = \left(Y_{fi}-Y_f\right)\frac{\widetilde{T}}{\widetilde{P}}\frac{1}{\tau_i}-\left(Y_{fe}-Y_f\right)\frac{\widetilde{T}}{\widetilde{P}}\frac{1}{\tau_e}-\frac{\widetilde{T}}{\widetilde{P}}\left(\frac{C_pT_0}{\Delta H_f}\right)\frac{1}{\tau_c}$$

$$\frac{dY_o}{dt} = \left(Y_{oi}-Y_o\right)\frac{\widetilde{T}}{\widetilde{P}}\frac{1}{\tau_i}-\left(Y_{oe}-Y_o\right)\frac{\widetilde{T}}{\widetilde{P}}\frac{1}{\tau_e}-S_r\frac{\widetilde{T}}{\widetilde{P}}\left(\frac{C_pT_0}{\Delta H_f}\right)\frac{1}{\tau_c}$$

for inlet pipe, the required differential equations are:

$$\frac{dL_a}{dt} = u_{ip}$$

$$\begin{cases} \dfrac{d\rho_a}{dt} = \dfrac{(\rho_u - \rho_i)}{L_{ip}} u_{ip} & L_a = L_{ip} \\ \dfrac{d\rho_a}{dt} = \dfrac{(\rho_u - \rho_a)}{L_a} u_{ip} & 0 < L_a < L_{ip} \end{cases}$$

$$\begin{cases} \dfrac{d\rho_b}{dt} = \dfrac{(\rho_u - \rho_i)}{L_{ip}} u_{ip} & L_b = L_{ip} \\ \dfrac{d\rho_b}{dt} = \dfrac{(\rho_b - \rho_i)}{L_b} u_{ip} & 0 < L_b < L_{ip} \end{cases}$$

$$(\rho_a L_a + \rho_b L_b)\frac{du_{ip}}{dt} = (\tilde{P}_u - \tilde{P}_i)P_0 - \frac{f(\rho_a L_a + \rho_b L_b)}{2D_{ip}} \frac{u_{ip}^3}{|u_{ip}|}$$

$$\begin{cases} \rho_a L_{ip} C_v \dfrac{d\tilde{T}_a}{dt} = \dfrac{C_v \dot{m}_u (\tilde{T}_u - \tilde{T}_a)}{A_i} - \dfrac{C_v \dot{m}_i (\tilde{T}_i - \tilde{T}_a)}{A_i} + \dfrac{f\rho_a u_{ip}^4 A_{sia}}{8|u_{ip}| A_i T_0} & L_a = L_{ip} \\ \rho_a L_a C_v \dfrac{d\tilde{T}_a}{dt} = \dfrac{C_v \dot{m}_u (\tilde{T}_u - \tilde{T}_a)}{A_i} + \dfrac{f\rho_a u_{ip}^4 A_{sia}}{8|u_{ip}| A_i T_0} & 0 < L_a < L_{ip} \end{cases}$$

$$\begin{cases} \rho_b L_{ip} C_v \dfrac{d\tilde{T}_b}{dt} = \dfrac{C_v \dot{m}_u (\tilde{T}_u - \tilde{T}_b)}{A_i} - \dfrac{C_v \dot{m}_i (\tilde{T}_i - \tilde{T}_b)}{A_i} + \dfrac{f\rho_b u_{ip}^4 A_{sib}}{8|u_{ip}| A_i T_0} & L_b = L_{ip} \\ \rho_b L_b C_v \dfrac{d\tilde{T}_b}{dt} = \dfrac{C_v \dot{m}_i (\tilde{T}_b - \tilde{T}_i)}{A_i} + \dfrac{f\rho_b u_{ip}^4 A_{sib}}{8|u_{ip}| A_i T_0} & 0 < L_b < L_{ip} \end{cases}$$

$$\begin{cases} \rho_b L_{ip} \dfrac{dY_{fb}}{dt} = \dfrac{\dot{m}_u}{A_i}(Y_{fu} - Y_{fb}) - \dfrac{\dot{m}_i}{A_i}(Y_{fi} - Y_{fb}) & L_b = L_{ip} \\ \rho_b L_b \dfrac{dY_{fb}}{dt} = \dfrac{\dot{m}_i}{A_i}(Y_{fb} - Y_{fi}) & 0 < L_b < L_{ip} \end{cases}$$

$$\begin{cases} \rho_b L_{ip} \dfrac{dY_{ob}}{dt} = \dfrac{\dot{m}_u}{A_i}(Y_{ou} - Y_{ob}) - \dfrac{\dot{m}_i}{A_i}(Y_{oi} - Y_{ob}) & L_b = L_{ip} \\ \rho_b L_b \dfrac{dY_{ob}}{dt} = \dfrac{\dot{m}_i}{A_i}(Y_{ob} - Y_{oi}) & 0 < L_b < L_{ip} \end{cases}$$

and for tailpipe, the required differential equations are:

$$\frac{dL_q}{dt} = u_{tp}$$

$$\begin{cases} \dfrac{d\rho_q}{dt} = \dfrac{(\rho_e - \rho_d)}{L_{tp}} u_{tp} & L_q = L_{tp} \\ \dfrac{d\rho_q}{dt} = \dfrac{(\rho_e - \rho_q)}{L_q} u_{tp} & 0 < L_q < L_{tp} \end{cases}$$

$$\begin{cases} \dfrac{d\rho_r}{dt} = \dfrac{(\rho_e - \rho_d)}{L_{tp}} u_{tp} & L_r = L_{tp} \\ \dfrac{d\rho_r}{dt} = \dfrac{(\rho_r - \rho_d)}{L_r} u_{tp} & 0 < L_r < L_{tp} \end{cases}$$

$$(\rho_q L_q + \rho_r L_r)\frac{du_{tp}}{dt} = (\tilde{P}_e - 1)P_0 - \frac{f(\rho_q L_q + \rho_r L_r)}{2D_{tp}} \frac{u_{tp}^3}{|u_{tp}|}$$

$$\begin{cases} \rho_q L_{tp} C_v \dfrac{d\tilde{T}_q}{dt} = \dfrac{C_v \dot{m}_e (\tilde{T}_e - \tilde{T}_q)}{A_e} - \dfrac{C_v \dot{m}_d (\tilde{T}_d - \tilde{T}_q)}{A_e} + \dfrac{f\rho_q u_{tp}^4 A_{stq}}{8|u_{tp}| A_e T_0} & L_q = L_{tp} \\ \rho_q L_q C_v \dfrac{d\tilde{T}_q}{dt} = \dfrac{C_v \dot{m}_e (\tilde{T}_e - \tilde{T}_q)}{A_e} + \dfrac{f\rho_q u_{tp}^4 A_{stq}}{8|u_{tp}| A_e T_0} & 0 < L_p < L_{tp} \end{cases}$$

$$\begin{cases} \rho_r L_{tp} C_v \dfrac{d\tilde{T}_r}{dt} = \dfrac{C_v \dot{m}_e (\tilde{T}_e - \tilde{T}_r)}{A_e} - \dfrac{C_v \dot{m}_d (\tilde{T}_d - \tilde{T}_r)}{A_e} + \dfrac{f\rho_r u_{tp}^4 A_{str}}{8|u_{tp}| A_e T_0} & L_q = L_{tp} \\ \rho_r L_r C_v \dfrac{d\tilde{T}_r}{dt} = \dfrac{C_v \dot{m}_d (\tilde{T}_r - \tilde{T}_d)}{A_e} + \dfrac{f\rho_r u_{tp}^4 A_{str}}{8|u_{tp}| A_e T_0} & 0 < L_p < L_{tp} \end{cases}$$

$$\begin{cases} \rho_q L_{tp} \dfrac{dY_{fq}}{dt} = \dfrac{\dot{m}_e}{A_e}(Y_{fe} - Y_{fq}) - \dfrac{\dot{m}_d}{A_e}(Y_{fd} - Y_{fq}) & L_q = L_{tp} \\ \rho_q L_q \dfrac{dY_{fq}}{dt} = \dfrac{\dot{m}_e}{A_e}(Y_{fe} - Y_{fq}) & 0 < L_q < L_{tp} \end{cases}$$

$$\begin{cases} \rho_q L_{tp} \dfrac{dY_{oq}}{dt} = \dfrac{\dot{m}_e}{A_e}(Y_{oe} - Y_{oq}) - \dfrac{\dot{m}_d}{A_e}(Y_{od} - Y_{oq}) & L_q = L_{tp} \\ \rho_q L_q \dfrac{dY_{oq}}{dt} = \dfrac{\dot{m}_e}{A_e}(Y_{oe} - Y_{oq}) & 0 < L_q < L_{tp} \end{cases}$$

In summary, the conservations laws for the combustion zone, inlet pipe and tailpipe have been developed. The solution of the equations above gives the pressure, temperature, fuel mass fraction and oxygen mass fraction in combustion zone, inlet pipe and tailpipe. The pressure and temperature at each pipe are related to the pressure and temperature in combustion chamber by the adiabatic isentropic process when the flow is from the combustor to either pipe.

5.3.5 Equation Solution and Initial Conditions

The governing equations are solved with a fourth-order Runge-Kutta scheme [130]. In the simulation programs, a time step decrement/increment method is employed in order to achieve the compromise between speed and accuracy of the calculation. A time-step decrement is performed when the temperature, pressure or velocity changes rapidly. This decrement is followed by a time-step increment when these changes are moderate.

The initial conditions are:

1) Initial temperature: $5 \times T_0$

2) Initial pressure: $1 \times P_0$

3) Friction factor: 0.03

The initial conditions correspond physically to filling the combustor with unburned fuel and air at ambient pressure with no exiting flow. An absolute temperature of five times the ambient is used to ensure the temperature is high enough to initiate combustion.

5.4 SIMULATION RESULTS OF ZERO-DIMENSIONAL PREMIXED COMBUSTION MODEL

To simplify the simulation, it is assumed that the air and gas are well mixed before entering into the inlet pipe zone. The combustion system geometrical parameters are given in Table 5.1.

For comparison of the experimental and simulation results, an FFT analysis [129-131] is undertaken to obtain the oscillating amplitude and frequency by via Matlab [132, 133] software.

5.4.1 Prediction of Pressure Oscillation in Combustor

The pressure is firstly predicted for the zero-dimensional combustion model at lean conditions, and is shown in Figure 5.3. The heat transfer process is predicted by fixing the wall temperature T_w at 1200 K and setting the heat transfer coefficient h at 120 W/m^{2}K. The friction coefficient f in the inlet pipe and tailpipe is assumed as 0.03.

Figure 5.3 (a) shows the instantaneous simulation result of the pressure oscillation in the combustion chamber. Compared with the simulation result in Figure 4.5 (a) in previous chapter, the proposed zero-dimensional premixed combustion model gives more accurate pressure oscillation. Similar to the experimental data, the peak values of the simulated pressure vary from cycle to cycle. As shown in Figure 5.3 (b) by FFT analysis, the predicted peak amplitude of the pressure oscillation is approximately 7.8 kPa, and the predicted frequency of the pressure oscillation is about 70 Hz. Figure 4.4 shows the experimental measured pressure oscillation has an amplitude of about 7.5 kPa with oscillating frequency about 75 Hz. The predicted amplitude and frequency of the oscillations are here in more reasonable agreement with measured results than the premixed combustor model with steady inlet mass flow.

Figure 5.4 and Figure 5.5 show the instantaneous simulation results of the inlet and exit mass flow rates. The inlet mass flow rate approximately varies from -0.0015 kg/s to 0.02 kg/s; while the exit mass flow rate approximately varies from -0.037 kg/s to 0.052 kg/s. As mentioned above, the fuel inlet is driven by high upstream pressure during the experiment. In addition, the cold air in the inlet acts as a resistance for the gases attempting to exit the combustion chamber through the inlet. Hence, most of the burned products from the combustor due to the high pressure will be driven out to the tailpipe, as demonstrated by the simulation results.

Figure 5.5 also shows the phase shift between the pressure in the combustor and the exit mass flow rate. Due to the reaction of fuel and oxygen, the pressure in the combustor will increase to drive the burned products out to the exhaust. When the pressure value in the combustor starts to decrease, the inertia of the fluid will keep accelerating the fluid

until the exit mass flow rate in the exhaust reaches the peak value. Hence, the phase of the pressure in the combustor is ahead of that of the exit mass flow rate in the exhaust. A similar analysis can be used for the phase relationship between the pressure in the combustor and the inlet mass flow rate.

5.4.2 Tailpipe Length Effects

Figure 5.6 shows the experiment result of the oscillation frequency of the pressure in the combustor for a number of tailpipe lengths. With increasing the tailpipe length, the oscillated pressure frequency in the combustor will continuously decrease, that is approximately from 80 Hz to 60 Hz.

Figure 5.7 shows the simulated results for the influence of the tailpipe length on the pressure amplitude and frequency in the combustor. The oscillation frequency of the pressure decreased from 75 Hz to 52 Hz as the tailpipe length increases. Figure 5.7 also shows the relationship between the maximum and minimum amplitude of the pressure oscillations and the tailpipe length. With increasing the tailpipe length, the maximum pressure amplitude trends to increase. The inverse trend is for the minimum pressure amplitude. For too long an exhaust, it will be more difficult for exhausted products to be driven out. Hence, the cold and fresh reactants will gradually accumulate in the combustion zone, and hence the flame will die out finally.

5.4.3 Inlet Pipe Length Effects

Figure 5.8 shows the simulated results for the influence of the inlet pipe length on the pressure amplitude and frequency in the combustor. The frequency of oscillations decreased from 87 Hz to 70 Hz as the inlet pipe length increases.

During the experiment, the fuel inlet is driven by high upstream pressure. In addition, the cold air in the inlet acts as a resistance for the gases attempting to exit the combustion chamber through the inlet. The effects of them are simplified by a constant pressure at the entrance of inlet pipe with a value slightly above atmospheric during the

simulation, causing most of the burned products to be driven out to the exhaust. The inlet pipe length needs to be selected to be long enough to avoid the burned products returning into the fresh reactant supply. In addition, if the inlet pipe is too long, the fresh premixed reactants need longer time to enter into the combustor. Too much heat is lost through the convective heat transfer and the exhaust before the enough fresh reactants are supplied to sustain the continuous combustion. Then the flame will eventually die out and extinction occurs.

5.5 DISCUSSION AND CONCLUSIONS

A zero-dimensional premixed combustion model is proposed and developed in this chapter. The essential features of the combustor geometry, combustion reaction rate and unsteady mixed reactants motion are accounted for. The governing equations presented identify key characteristic length and time scales, while the numerical simulation of the equations provides a relatively more efficient prediction of the combustion pressure oscillations. In addition, the pressure in the inlet pipe with a value slightly above atmospheric is considered.

The proposed zero-dimensional premixed combustion model gives pressure oscillations closer to those measured experimentally, with the peak values of the simulated pressure varying from cycle to cycle. The simulation results show agreement with the experiment as the tailpipe length varies. For too long an exhaust, it will be more difficult for products to exhaust. Hence, the cold and fresh reactants will gradually accumulate in the combustion zone, and the flame will die out finally. For a too short an inlet pipe, the burned products may pass directly into the fresh reactant supply, which should be avoided. If the inlet pipe length is too long, more heat would be lost through convective heat transfer and the exhaust before enough fresh reactants are supplied to sustain the continuous combustion. Thus the flame will eventually die out with extinction occuring.

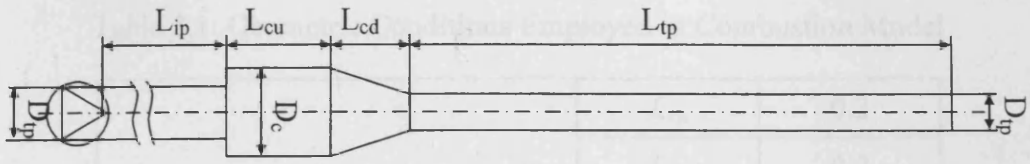

Figure 5.1: Schematic Layout of Experimental Combustor

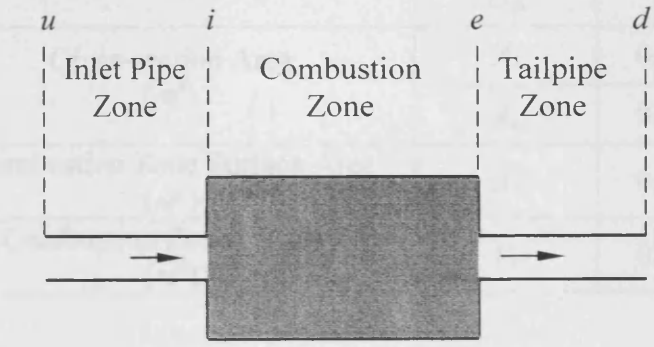

(a)

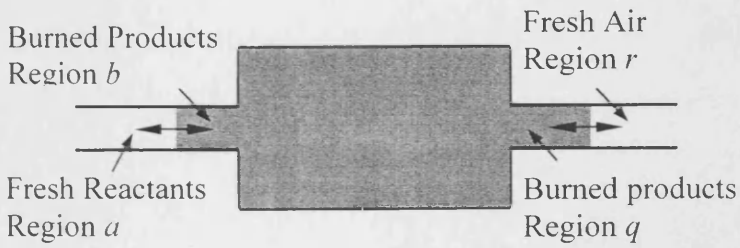

(b)

Figure 5.2: Schematic Layout of Combustion System

Table 5.1: Geometric Conditions Employed in Combustion Model

Length (m)	L_{cu}	0.2
	L_{cd}	0.2
	L_{ip}	8.5
	L_{tp}	1.12
	L_{c1}	0.0278
	L_{c2}	2.53
Diameter (m)	D_c	0.15
	D_{ip}	0.075
	D_{tp}	0.05
Cross-section Area (m^2)	A_i	0.00442
	A_e	0.00196
Combustion Zone Surface Area (m^2)	A_s	0.17842
Combustion Zone Volume (m^3)	V_c	0.00496

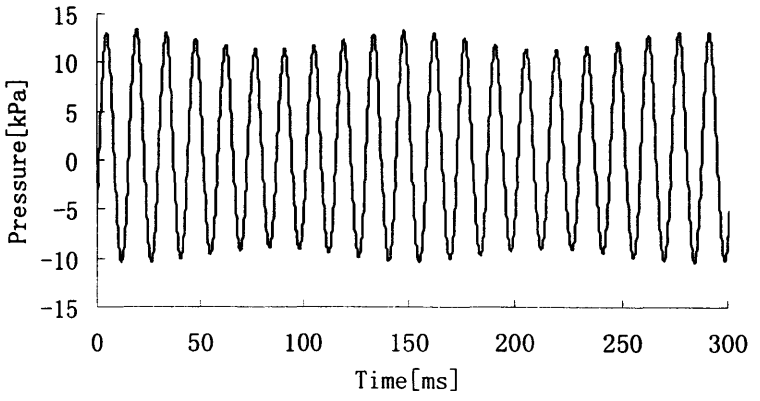

(a) Simulated Pressure Oscillations in Combustion Chamber

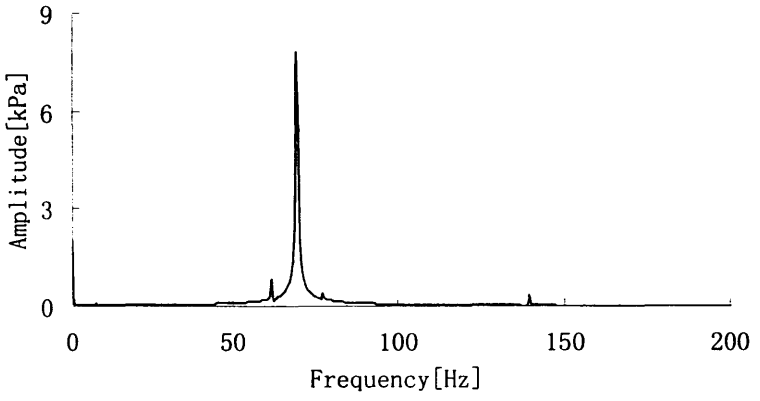

(b) FFT Analysis Result for Simulated Pressure Oscillations in Combustion Chamber

Figure 5.3: Instantaneous Simulation Result of Pressure in the Combustion Chamber

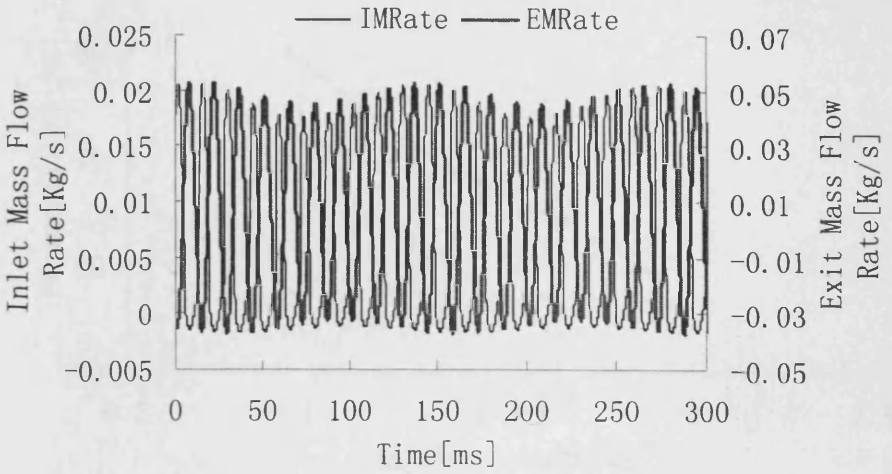

Figure 5.4: Instantaneous Simulation Results of the Inlet and Exit Mass Flow Rates

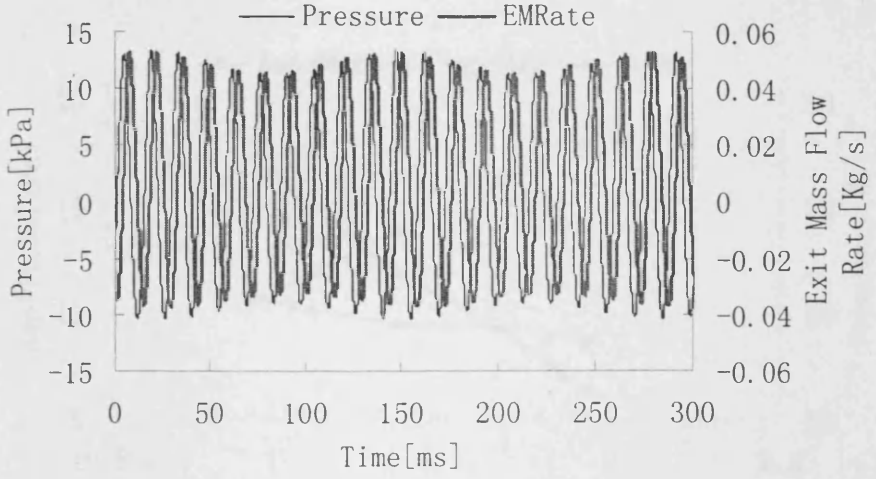

Figure 5.5: Relationship between Pressure in Combustor and Exit Mass Flow Rate

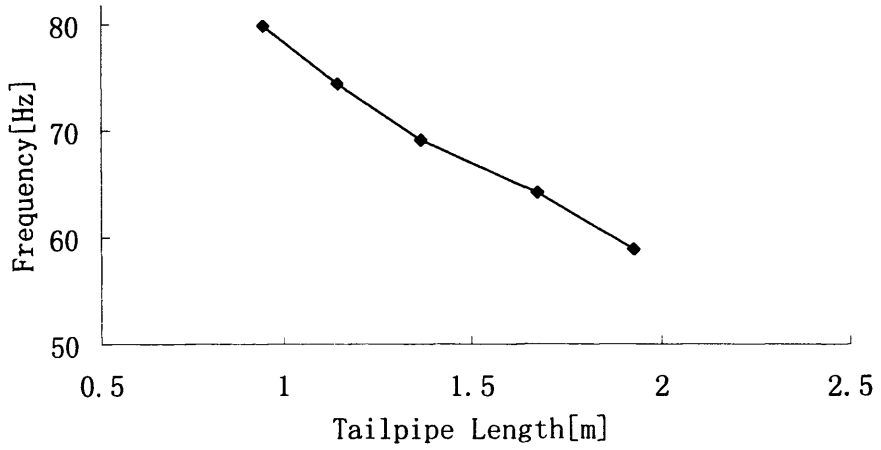

Figure 5.6: Experimental Frequency of Pressure Oscillations in Combustor as Function of the Tailpipe Length

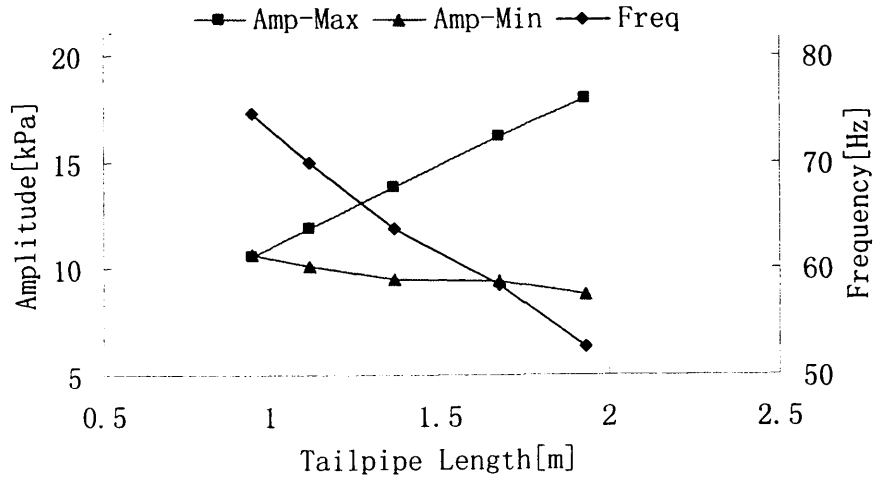

Figure 5.7: Simulated Amplitude and Frequency of Pressure Oscillations in Combustor as Function of the Tailpipe Length (Amp-Max means the maximum pressure amplitude, and Amp-Min means the minimum pressure amplitude.)

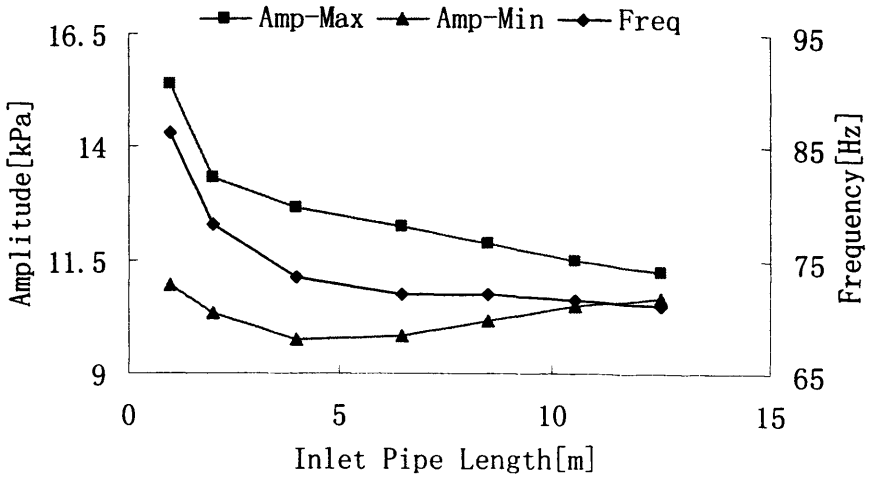

Figure 5.8: Simulated Amplitude and Frequency of Pressure Oscillations in Combustor as Function of the Inlet Pipe Length (Amp-Max means the maximum pressure amplitude, and Amp-Min means the minimum pressure amplitude.)

6. PREMIXED COMBUSTION MODEL BASED ON ONE-DIMENSIONAL TRANSMISSION LINE THEORY

6.1 INTRODUCTION

In Chapter 4, a premixed combustor model has been developed. This can predict the classic flame extinction and ignition boundaries, but also oscillating combusting at certain conditions with a steady premixed supply of fuel and air. A sinusoidal supply is then considered to simulate the influence of the back flow to the inlet due to the high pressure in the combustor.

In Chapter 5, a more accurate zero-dimensional premixed combustion model is developed. The essential features of the combustor geometry, combustion reaction rate and unsteady mixed reactants motion are accounted for. A contact surface is assumed to separate the fresh reactant or fresh air from the burned products, which moves through the inlet pipe and tailpipe regions. Assuming uniform conditions within each region, the volume and surface integral are reduced to algebraic expressions, resulting in a set of first-order differential equations. The proposed zero-dimensional premixed combustion model gives more accurate pressure oscillation predictions. Similar to the experimental data, the peak values of the simulated pressure vary from cycle to cycle. The simulation results show agreement with the experiment as the tailpipe length varies.

In reality, when the burned product is driven out to the inlet or exhaust, mixing processes between the fresh reactants and fresh air with the burned product occurs. To overcome the assumption of the slug flow in the inlet pipe and tailpipe in the previous chapter, a premixed combustion model with an added one-dimensional transmission line is proposed in this chapter. The parameters in combustor and tailpipe are only considered as the function of time variable; while the extra spatial variable is included for the parameters in the inlet pipe.

6.2 COMBUSTION MODEL GEOMETRY AND EXPERIMENT RESULTS

The schematic layout of the experimental combustor is shown in Figure 6.1, which consists of an inlet pipe, combustion chamber and tailpipe. The combustor used is the Helmholtz type as described before.

The geometry of combustion model is shown in Figure 6.2, which is separated into inlet and combustion regions. The combustion region, including the combustor and tailpipe, is just as the layout of combustor model in Chapter 4, in which all the parameters are only considered as the function of time variable. In the inlet pipe region, the spatial variable is included into the parameters, which is similar to the one-dimensional transmission line model in Chapter 3.

As described in previous chapters, the pressure wave is measured using a fast responding piezo-electric pressure transducer, and the temperature is measured with fine wire thermocouples. Velocity measurements are carried out using Laser Doppler Anemometry [111].

Figure 4.4 (a) and (b) show the instantaneous experimental data of combustion chamber pressure and associated FFT analysis, the pressure amplitude is about 7.5 kPa with oscillating frequency about 75 Hz.

6.3 PREMIXED COMBUSTION MODEL INCORPORATING ONE-DIMENSIONAL TRANSMISSION LINE ANALYSIS FOR THE INLET

The new model incorporates a one-dimensional transmission line analysis for the inlet and the developed premixed combustor model. The equations established in Chapter 4 are directly used for the premixed combustor model and the one-dimensional transmission line model including the mass fraction equations is used to predict the fluid dynamics in inlet pipe. The orifice equations are used to derive the linkage of these two models. The relevant assumptions are as before.

6.3.1 Conservation Equations in Combustion Region

The combustion region includes the combustor and the tailpipe, as established in Chapter 4. The model includes the effects of heat transfer with the combustor wall and friction in the tailpipe. The governing equations are integrated over the combustion chamber and the tailpipe volumes to simplify the description of the physical process and the computation of the numerical solution. The mixture of fuel and air in lean condition is considered. Thus, the combustion region equations are obtained by simplifying the balances of energy, mass and fuel in the combustion chamber, together with momentum balance in the tailpipe.

The conservation equations used for combustion region are summarized as:

$$\begin{cases} \dfrac{d\widetilde{T}}{dt} = \left(\dfrac{1}{\tau_f} + \dfrac{1}{\tau_{HT}} + \dfrac{1}{\tau_c}\right)\dfrac{\gamma\widetilde{T}}{\widetilde{P}} - \left((\gamma-1)\dfrac{Z_e}{\rho_0} + \dfrac{1}{\tau_f} + \dfrac{\gamma T_0}{\tau_{HT}T_w}\right)\dfrac{\widetilde{T}^2}{\widetilde{P}} \\ \dfrac{d\widetilde{P}}{dt} = \left(\dfrac{1}{\tau_f} + \dfrac{1}{\tau_{HT}} + \dfrac{1}{\tau_c} - \left(\dfrac{Z_e}{\rho_0} - \dfrac{T_0}{\tau_{HT}T_w}\right)\widetilde{T}\right)\gamma \\ \dfrac{dY_f}{dt} = \left(Y_{f,i} - Y_f\right)\dfrac{\widetilde{T}}{\widetilde{P}}\dfrac{1}{\tau_f} - \dfrac{\widetilde{T}}{\widetilde{P}}\left(\dfrac{C_pT_0}{\Delta H_f}\right)\dfrac{1}{\tau_c} \\ \dfrac{du}{dt} = \left(\widetilde{P}_e - 1\right)\dfrac{RT_0}{L_{tp}}\dfrac{\widetilde{T}_e}{\widetilde{P}_e} - \dfrac{f}{2D_{tp}}\dfrac{u^3}{|u|} \end{cases} \tag{6.1}$$

6.3.2 Conservation Equations in Inlet Pipe Region

A combined transmission line model proposed in Chapter 3 is used to describe the premixed reactants dynamics in inlet pipe. The schematic layout of the inlet pipe region is shown as Figure 6.3.

The inlet pipe is separated into N segments. To update the boundary conditions, the lumped model is used to represent the primitive variables in the first and the last segments; while the finite difference model is used to simulate the primitive variables in

the rest of the segments. As shown in Figure 6.3, the position u is linked with the premixed fresh reactant supply. Here, it is assumed that the premixed fresh reactant supply is so large that the pressure and the temperature are unchanged. The orifice equations are used to calculate the mass flow rate into the position u. The segments in the middle, such as position k, are modelled by finite difference equations. The position i is the one linked with the following combustor model. The orifice equations are used to calculate the mass flow rate into or out from the combustor. Considering that the burned products due to the high pressure in the combustor are mainly driven out to the tailpipe, the temperature in the inlet pipe is assumed to be constant.

For the lumped model in the first and last segments, the orifice equation is:

$$\dot{M}_d = C_d \cdot C_m \cdot A \cdot P_u / \sqrt{T_u} \tag{6.2}$$

For the finite difference model in the middle segments, the conservation equations are:

$$\begin{cases} \dfrac{\partial \rho_{ip}}{\partial t} + \dfrac{\partial (\rho_{ip} u_{ip})}{\partial x} = 0 \\ \dfrac{\partial (\rho_{ip} Y_{f,ip})}{\partial t} + \dfrac{\partial (\rho_{ip} u_{ip} Y_{f,ip})}{\partial x} = 0 \\ \dfrac{\partial (\rho_{ip} u_{ip})}{\partial t} + \dfrac{\partial \left(\rho_{ip} u_{ip}^2 + P_{ip} - \frac{4}{3} \mu \dfrac{\partial u_{ip}}{\partial x} \right)}{\partial x} = 0 \end{cases} \tag{6.3}$$

Compared with the air transmission line model, the mass fraction equation is added to predict the variance of the fuel due to the convection in the inlet pipe.

In addition, it is found that variations of the kinematic viscosity scarcely affect the simulation results in Chapter 3. Hence, the kinematic viscosity is assumed to be constant in the following research.

6.3.3 Equation Solution and Initial Conditions

The governing equations for premixed combustor model are solved with Eulers method [129]. The initial conditions are:

1) Initial temperature: $5 \times T_0$

2) Initial pressure: $1 \times P_0$

3) Friction factor: 0.03

The initial conditions correspond physically to filling the combustor with unburned fuel and air at ambient pressure with no exiting flow. Again an absolute temperature of five times the ambient is used to ensure the temperature high enough to initiate combustion.

The Upwind Method is used to discretize the Equation (6.3) in this study.

6.4 SIMULATION RESULTS OF PREMIXED COMBUSTION MODEL INCORPORATING ONE-DIMENSIONAL TRANSMISSION LINE ANALYSIS FOR THE INLET

To simplify the simulation, it is assumed that the air and gas are well mixed before entering into the inlet pipe zone. The combustion system geometrical parameters are given in Table 6.1.

For comparison of the experimental and simulation results, the FFT analysis [129-131] of the pressure analysis is again used as before.

The simulation results are shown as Figure 6.4. From the FFT analysis, it is shown that the peak frequency of the pressure oscillation is about 58 Hz with the oscillation amplitude 3.84 kPa.

6.5 DISCUSSION AND CONCLUSIONS

With the combustion system geometrical parameters listed in Table 6.1, the comparison of experimental and simulation results for different combustion models are shown in Table 6.2. It is obvious that Zero-dimensional Combustion Model gives the most accurate results at the moment. The combustion model using a one-dimensional transmission line analysis for the inlet gives the largest divergence from the experimental results, but potentially has the most promise. The reasons might be:

1) Due to the high pressure from the combustor, parts of the burned products must be exhausted into the inlet pipe, which will heat the reactants there. The temperature in the inlet pipe may thus be higher than that of the atmosphere. However the ambient temperature in the inlet pipe is assumed constant for the convenience of simulation, although this could be changed in future work.

2) The orifice equations are used to link the combustor model and one-dimensional transmission line model, which is also used to update the boundary conditions for the inlet pipe. The orifice equations could be treated as a static model. The mass flow rate through the orifice is only determined by the pressure values before and after the orifice, hence the inertial force of the reactants is neglected. For the models in the previous transmission model, this neglect is acceptable due to the gradual change of the pressure in different positions within the transmission line. However, for combustion model, the pressure inside of the combustor is changed significantly due to the chemical reaction. Hence, the neglect of the inertial force will induce this significant difference between the simulation and experimental results.

For the future research, the energy equations should be considered for the inlet pipe and tailpipe, which also includes the effect of the heat conduction between the exhausted heat products and pipe walls. In addition, more accurate differential equations should be studied to replace the orifice equations to update the boundaries conditions for the inlet pipe and tail pipe. Based on this, the one-dimensional conservation equations can be used to calculate the density, velocity and temperature, and then to predict more accurate dynamic characteristics in the inlet pipe and tailpipe.

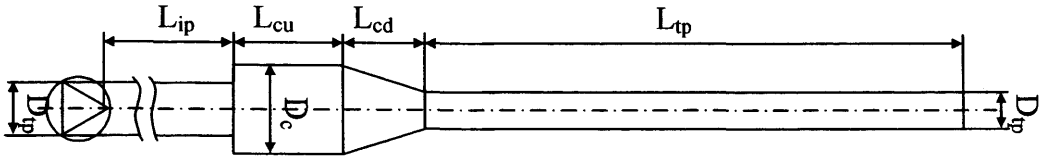

Figure 6.1: Schematic Layout of Experimental Combustor

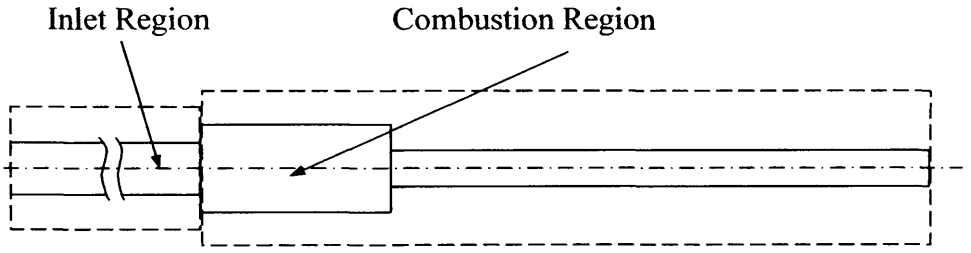

Figure 6.2: Schematic Layout of Combustion System

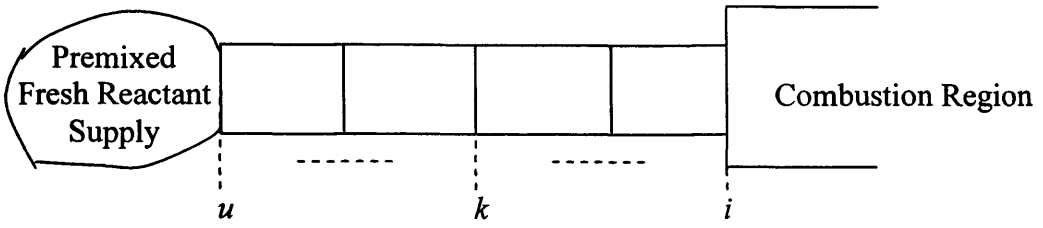

Figure 6.3: Schematic Layout of Inlet Region

Table 6.1: Geometric Conditions Employed in Combustion Model

Length (m)	L_{cu}	0.2
	L_{cd}	0.2
	L_{ip}	8.5
	L_{tp}	1.12
	L_{c1}	0.0278
	L_{c2}	2.53
Diameter (m)	D_c	0.15
	D_{ip}	0.075
	D_{tp}	0.05
Cross-section Area (m^2)	A_i	0.00442
	A_e	0.00196
Combustion Zone Surface Area (m^2)	A_s	0.17842
Combustion Zone Volume (m^3)	V_c	0.00496

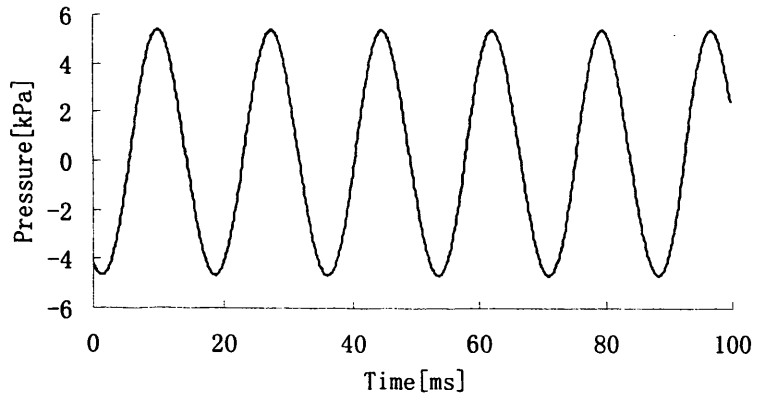

(a) Simulated Pressure Oscillations in Combustion Chamber

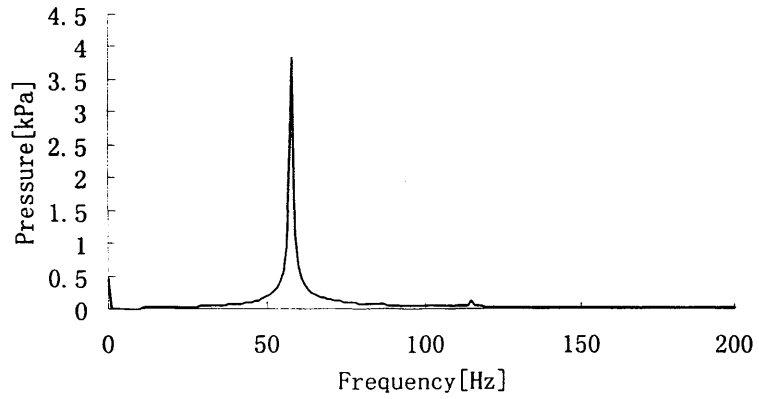

(b) FFT Analysis Result for Simulated Pressure Oscillations in Combustion Chamber

Figure 6.4: Instantaneous Simulation Result of Pressure in the Combustion Chamber

Table 6.2: Comparison of Experimental and Simulation Results

	Peak Oscillation Frequency [Hz]	Peak Oscillation Amplitude [kPa]
Experimental Result	75	7.51
Combustor Model	68	12.9
Zero-dimensional Combustion Model	70	7.8
One-dimensional Combustion Model	58	3.84

7. CONCLUSIONS AND RECOMMENDATIONS FOR FUTURE WORK

7.1 CONCLUSIONS

The thrust of this thesis has been the development of generalised dynamic combustion models, which can be adapted to a wide variety of different situations. The aim of the study has been to provide quantitative tools, which are relatively simple to use and provide solutions in relatively short time-scales, yet are sufficiently elaborate to be of use for design purposes, and can contribute to the understanding and control of transient combustion processes, thus laying the foundations for the future improved passive and active control of pressure oscillations and emissions during the combustion process.

Three combustion models for premixed conditions have been presented. The models predicted instabilities of the combustion oscillations similarly to those observed in the pulsating combustion system at Cardiff University. Discussions are made about how the model can achieve wider applicability

7.1.1 Inlet Pipe Model for the Combustor

Using air as the working medium presents several key modelling problems as it is highly compressible and thus affects the overall system response. The investigation regarding air dynamics especially in transmission line is needed to understand the air flow mechanism and thus provides the necessary consideration that can be included in the combustor model and future system control algorithm.

The transmission line diameter calibration experiment shows that the relationship between the diameter and the exerted pressure is close to linear, which is then applied to the simulation algorithm to conclude the influence of the working pressure on the

transmission line diameter expansion.

Another important aspect in air transmission line investigation is the determination of working fluid viscosity since this affects the pressure wave propagation characteristics. This pressure wave propagation diminishes over time due to energy loss. The energy loss is mainly in the form of viscous friction between the fluid and inner wall of the transmission line. From this understanding, the determination of the air viscosity value is vital in order to model the air dynamics in the transmission line to an acceptable degree of accuracy. In this study, the pressure drop equation along the pipe line is then utilized to find the kinematic viscosity, which is about 0.00011 m^2/s.

The Navier-Stokes equations are then used with the conservation laws, which are the continuity, momentum and energy equations. However, the Navier-Stokes equations in three-dimensional format are complex to solve especially in specifying the correct boundary conditions. Assumptions are then needed to simplify modelling while still obtaining the required results. Vector form of equations offers a more convenient way of applying the algorithm into the computer programming language and enables the decoding of the specified algorithm to obtain the primitive variables needed to compute the changes of the respective air parameters such as mass, pressure, density, velocity and viscosity before completing each time iteration.

For the model, completely blocked at the ends the rod type-T thermocouples are used to measure the temperature as the trapped air is disturbed by pressure ripples. Hence, it is assumed the temperature is constant for the simulation in this study.

The lumped modelling can be used to model pneumatic systems to some accuracy depending on the system modelled and assumptions applied. It is easier to implement compared to a finite difference approach and consumes less computing power due to the simplicity of the equations involved. However, this method can not be used to predict the propagation of the pressure waves for both-end blocked transmission lines, although the steady state pressure characteristics in the pneumatic system can be predicted.

From the experiments, it is shown that the transmission line has a very significant influence on the whole system dynamics. Hence, a valid mathematical model and

method is needed to properly represent the pressure wave in it. In this study, a time domain model describing the dynamics of air in a transmission line is developed by considering changes in air density, pressure and mass flow rate and assuming the temperature to be constant. A combined model is proposed to simulate the dynamics of trapped air in a blocked transmission line and the charging of a large volume with the transmission line. In order to update the boundary conditions, the first and the last segments are considered as two lumped volumes. The rest of the transmission line segments are represented by means of a finite difference model. The effectiveness of the proposed model is shown through comparisons of simulated pressure responses against pressures measured by practical experiments. The simulated results can be concluded to be successful since it matches well with the captured experimental data though the simulated results show longer system transient state for the completely blocked model.

7.1.2 Premixed Combustor Model

Initially, a simplified premixed combustor model was proposed. This premixed model has been able to reproduce most of the dynamic characteristics in the combustor such as amplitude modulations and phase shift changes in the pressure oscillations.

Several variations of the premixed model, for inlet flow of reactants to the combustor, have been proposed and investigated. This includes the effects of wall temperature, heat transfer, tailpipe friction, and equivalence ratio. Within the stable regime, for steady inlet flow conditions, reasonable agreement was found between the predicted pressure amplitude of the combustor diagnostics and the experimental data. However, modelling the inlet flow as a premixed sinusoidal supply of reactants, and allowing eventually reverse flow in the inlet, induced the modulations between the primary variables.

A main flow with a second sinusoidal inlet supply is simulated to investigate the influence of this second mass flow on the pressure oscillations. The simulation results show that it is not appropriate to select the air as the second inlet mass flow. Even if the large average value of the inlet mass flow of the air is chosen, it is impossible to greatly change the oscillation amplitudes of the pressure. For the usage of the fuel as the second inlet mass flow, its average value is dependent on the equivalence ratio in the main inlet

mass flow to ensure the combustion is in the lean condition. When the equivalence ratio in the main flow is smaller, it's rational to use the fuel as the second inlet mass flow. The small injection of the fuel causes evident changes of the oscillation pressure amplitude. While for larger equivalence ratios in the main inlet mass flow, the mixed reactants with the same equivalence ratio is appropriate.

7.1.3 Zero-dimensional Premixed Combustion Model

To include the dynamics of the inlet pipe and tailpipe, a zero-dimensional premixed combustion model has been developed from the earlier work. The governing equations presented identified key characteristic length and time scales, while the numerical simulation of the equations provides a relatively more efficient prediction of the combustion pressure oscillations. In addition, the pressure in the inlet pipe with a value slightly above atmospheric is considered. A contact surface is assumed to separate the fresh reactant or fresh air from the burned products, which moves through the inlet pipe and tailpipe regions.

The effects of the inlet pipe and tailpipe length are investigated for the proposed zero-dimensional premixed combustion model, which gives more accurate pressure oscillation predictions similar to the experimental data with the peak values of the simulated pressure varying from cycle to cycle. The simulation results also show agreement with the experiment as the tailpipe length is varied.

7.1.4 Premixed Combustion Model Based Incorporating a One-dimensional Transmission Line Analysis for the Inlet

Here the premixed combustion model from Chapter 4 is integrated with the air transmission line model of Chapter 3. Appropriate model modifications for the inlet pipe, which includes the mass fraction equations are made.

Compared with the experimental data, this model gives poorer results, probably due to the omission of the temperature influence on the fluid dynamics and the updating methods for boundary conditions in the inlet pipe.

The models produced have already shown considerable promise in predicting oscillations in a pulsating combustor. Further work is needed on the inlet pipe prediction and model integration, but nevertheless this provides a firm foundation for future work.

In terms of integration with neural network analysis as reviewed in Chapter 2, it is clear that there are several parameters which could be optimised by such techniques to further improve predictions. These include resonant frequencies (ω_1-first harmonic; ω_2-second harmonic) and *rms* (root mean squares of the pressure in combustor) values.

7.2 RECOMMENDATIONS FOR FUTURE WORK

An inlet pipe model with the energy equation is clearly needed to allow for the influence of temperature. New discretisation methods should be considered to improve the accuracy of the model, whilst maybe more rational equations are needed to replace the lumped models for updating the boundary conditions of the inlet pipe.

Modelling the feedback mechanism between the combustor and fuel-supply oscillations, and improvements in modelling the inlet pipe and tailpipe fluid mechanics are likely to improve the accuracy of the predictions. A modified one-dimensional transmission line model combined with the combustor model should be better able to simulate the fluid dynamics when the fluid is entering into or exhausting from the combustor.

As pressure, temperature and fuel mass fraction, etc, are now predicted within the combustion model, a post-processor sub-model could easily be implemented in the future for continuous NO_x prediction over the cycles, maybe using Chemkin.

The simple simulation of PI control for combustion pressure instabilities in Chapter 4 suggests that the pressure oscillation could be attenuated by varying the inlet mass flow rate. The simulation of a main flow with a second sinusoidal inlet supply also proves

that small changes of the fuel or mixed reactant will induce large chances of the oscillation amplitudes of the pressure. For the combustion instabilities control purpose in the future work, the model developed above is needed, suitably tuned by the artificial neural network to follow as closely as possible the dynamics of the system. This identification model is then used to train a second neural network controller, which is then used to adjust the second inlet mass flow of fuel or mixed reactants (probably via a pneumatic proportional valve) to attenuate the pressure oscillations, after which a more complex control algorithm needs be designed to consider both pressure oscillations and NO_x emission. The possible experimental layout is shown as Figure 7.1.

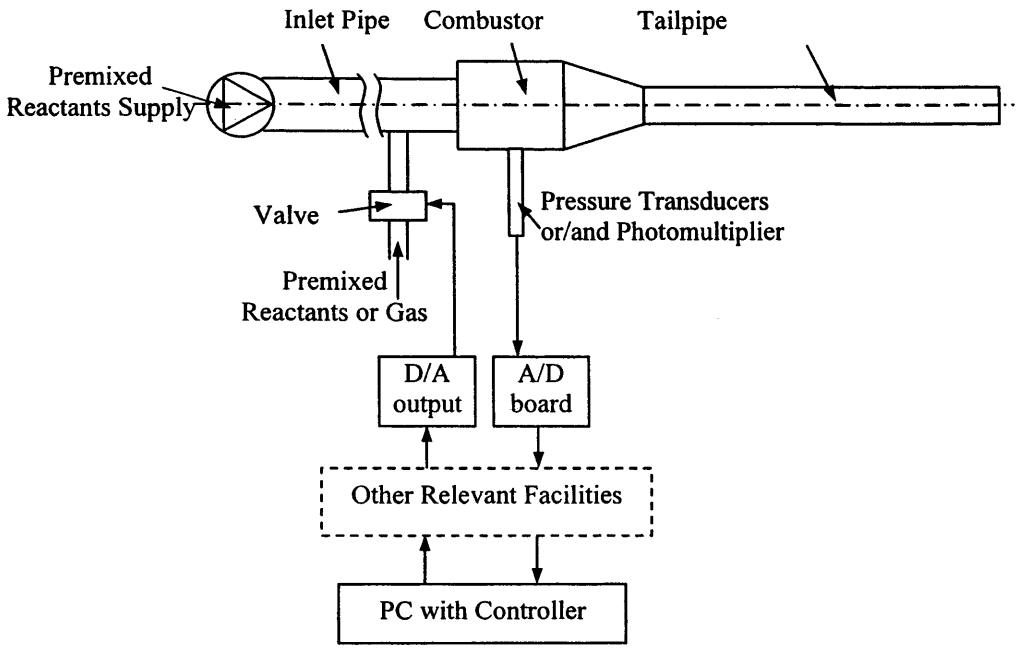

Figure 7.1: Layout for Experimental Combustion System Instabilities Control

REFERENCES

1. R. Blonbou, A. Layerdant, S. Zaleski and P. Kuentzmann. *Active Adaptive Combustion Control Using Neural Networks*. Combustion Sci. and Tech., Vol. 156, pp. 25-47, 2000.

2. L. Cammarata, A. Fichera and A. Pagano. *Neural Prediction of Combustion Instability*. Applied Energy, Vol. 72, Issue 2, pp. 513-528, June 2002.

3. Soteris A. Kalogirou. *Artificial Intelligence for the Modeling and Control of Combustion Processes: a Review*. Progress in Energy and Combustion Science, Vol. 29, Issue 6, pp. 515-566, 2003.

4. A. E. Ruano, P. J. Fleming, C. Teixeira, K. Rodríguez-Vázquez and C. M. Fonseca. *Nonlinear Identification of Aircraft Gas-turbine Dynamics*. Neurocomputing, Vol. 55, Issues 3-4, pp. 551-579, October 2003.

5. M. M. Awais. *Application of Internal Model Control Methods to Industrial Combustion*. Applied Soft Computing, Vol. 5, Issue 2, pp. 223-233, January 2005.

6. Irvin Glassman. *Combustion*. Academic Press, 1996, San Diego, CA, USA.

7. Reynst F. H.. *Pulsating Combustion*. Pergamon Press, NY, 1952.

8. Y. Xue, N. Syred, V. Rodriguez-Martinez, T. O'Doherty and Y. Qin. *Dynamic Modeling of a Swirl Burner Using Artificial Neural Networks*. Proceedings of Combustion and Noise Control, pp. 149-162, 2003, Cranfield, UK.

9. K. Hornik, M. Stinchcombe and H. White. *Mutliplayer Feedforward Neural Networks are Universal Approximators*. Neural Networks, Vol. 2, pp. 359-366, 1989.

10. Kumpati S. Narendra and Kannan Parthasarathy. *Identification and Control of Dynamical Systems Using Neural Networks*. IEEE Transactions on Neural Networks, Vol. 1, No. 1, pp. 4-27, March 1990.

11. N. Bhat and T. J. McAvoy. *Use of Neural Nets for Dynamic Modeling and Control of Chemical Process Systems*. Comput. Chem. Eng. Vol. 14, pp. 573-582, 1990.

12. D. C. Psichogios and L. H. Ungar. *Direct and Indirect Model Based Control Using Artificial Neural Networks*. Ind. Engin. Chem. Res. Vol. 30, pp. 2564-2573, 1991.

13. E. P. Nahas, M. A. Henson, and D. E. Seborg. *Nonlinear Internal Model Control Strategy for Neural Network Models*. Comput. Chem. Eng. Vol. 16, pp. 1039-1057, 1992.

14. M. Nikolaou, and V. Hanagandi. *Control of Nonlinear Dynamical Systems Modeled by Recurrent Neural Networks*. Am. Inst. Chem. Eng. J. Vol. 39, pp. 1890-1894, 1993.

15. Su H. T. and McAvoy T. J.. *Integration of Multilayer Perceptron Networks and Linear Dynamic Models: a Hammerstein Modeling Approach*. Ind. Engin. Chem. Res. Vol. 32, pp. 1927-1936, 1993.

16. D. Urbani, P. Roussel-Ragot, L. Personnaz and G. Dreyfus. *The Selection of Neural Models of Non-Linear Dynamical Systems by Statistical Tests*. Neural Networks for Signal Proceeding [1994] IV, Proceedings of the 1994 IEEE Workshop, pp. 229-237, 6-8 Sep 1994, Ermioni, Greece.

17. M. S. Ahmed and I. A. Tasadduq. *Neural-net Controller for Nonlinear Plants: Design Approach through Linearisation*. IEE Proc-Control Theory Appl. Vol. 141, pp. 315-322, 1994.

18. Sjoberg J.. *Nonlinear Black-box Structure-Some Approaches and Some Examples*. In Advances in Intelligent Control, Edited by C. J. Harris, Taylor and Franchis Publisher, 1994.

19. Passino K. M.. *Intelligent Control for Autonomous Systems*. IEEE Spectrum, pp. 55–62, June 1995.

20. Sjoberg J., Zhang Q., Ljung L., Beneviste A., Deylon B., Hjalmarsson P.Y.G.H., and Juditsky A.. *Nonlinear Black-box Modeling in System identification: a Unified Overview*. Automatica, Vol. 31, pp. 1691-1724, 1995.

21. Wang Fuli, Li Mingzhong and Yang Yinghua. *Neural Network Pole Placement Controller for Nonlinear Systems Through Linearisation*. American Control Conference, pp. 1984-1988, Albuquerque, New Mexico, June 1997.

22. J.M. Zamarreno and P. Vega. *Neural Predictive Control: Application to a Highly Non-linear System*. Engineering Applications of Artificial Intelligence, Vol. 12, pp. 149-158, 1999.

23. Huailin Shu and Youguo Pi. *PID Neural Networks for Time-delay Systems*. Computers and Chemical Engineering, Vol. 24, pp. 859-862, 2000.

24. N. Yadaiah, B.L. Deekshatulu, L. Sivakumar and V. Sree Hari Rao. *Neural Network Algorithm for Parameter Identification of Dynamical Systems Involving Time Delays*. Applied Soft Computing, Vol. 7, Issue 3, pp. 1084-1091, June 2007.

25. Rodriquez-Martinez, V.M., PhD thesis, University of Wales, Cardiff, 2003.

26. Stecki J. and Davis D.. *Fluid Transmission Lines-Distributed Parameter Models, Part 1: A Review of the State of the Art*. Proc. Instn. Mech. Engrs., Part A, Vol. 200, pp. 215-228, 1986.

27. Stecki J. and Davis D.. *Fluid Transmission Lines-Distributed Parameter Models, Part 2: Comparison of Models*. Proc. Instn. Mech. Engrs., Part A, Vol. 200, pp. 229-236, 1986.

28. Watton J. and Tadmori M.. *A Comparison of Techniques for the Analysis of Transmission Line Dynamics in Electrohydraulic Control Systems*. Appl. Math. Modelling, Vol. 12, pp. 457-466, 1988.

29. Hullender D., Woods R. and Hsu C.. *Time Domain Simulation of Fluid Transmission Lines using Minimum Order State Variable Models*. In Fluid Transmission Line Dynamics, Edited by M. Franke and T. Drzewiecki, ASME, pp. 78-97, 1983.

30. Piche R. and Ellman A.. *A Fluid Transmission Line Model for Use with ODE Simulators*. The Eight Bath International Fluid Power Workshop, Sep 20-22, 1995, Bath, UK 1995.

31. John C. Tannehill, Dale A. Anderson and Richard H. Pletcher. *Computational Fluid Mechanics and Heat Transfer (Second Edition)*. Taylor & Francis, Washington, USA, 1997.

32. Griffiths J. F., and Barnard J. A.. *Flame and Combustion*. Blackie Academic & Professional, 1995.

33. Jones J. C.. *Combustion Science, Principle and Practice*. Millennium Books, Australia, 1993.

34. Lord Rayleigh. *The Explanation of Certain Acoustical Phenomena*. Nature, 18:319, 1878.

35. Rayleigh J. W.. *The Theory of Sound*. Vol. II, Dover Publications, New York, USA, 1945.

36. Chomiak J.. *Combustion a Study in Theory, Fact and Application*. Abacus Press/Gordon & Breach Science Publishers, Switzerland, 1990.

37. Reynolds O.. *An Experimental Investigation of the Circumstances Which Determine Whether the Motion of Water shall be Direct or Sinuous, and of the Law of Resistance in Parallel Channels*. Philosophical Transactions of the Royal Society, 174, pp. 935-982, 1883.

38. Marsano S.. *Modelling Transient Combustion Systems*. PhD Thesis, Division of Mechanical Engineering and Energy Studies, Cardiff University, 1999.

39. N. Syred, VI Hanby, and AK Gupta, *Resonant Instabilities Generated by Swirl Burners*. Journal of the Institute of Fuel, pp. 402-407, London, December 1973.

40. M.A. Macquisten and A. P. Dowling. *Combustion in a Twin-Stream Afterburner*. Journal of Sound and Vibration, pp. 545-560, 188(4), 1995.

41. K. H. Yu, K. J. Wilson and K. C. Schadow. *Liquid-Fuelled Active Instability Suppression.* Twenty-Seventh Symposium on Combustion, The Combustion Institute, pp. 2039-2046, Pittsburgh, Pa 1998.

42. Dowling, A. P. and Stow S. R.. *Acoustic Analysis of Gas Turbine Combustors,* AIAA Journal of Propulsion and Power, Vol. 19, No. 5, pp. 751-764, 2003.

43. Lieuwen, T.. *Modeling Premixed Combustion-Acoustic Wave Interactions: A Review.* AIAA Journal of Propulsion and Power, Vol. 19, No. 5, pp. 765-781, 2003.

44. K. J. Hunt, D. Sbarbaro, R. Zbikowski, and P. J. Gawthrop. *Neural Networks for Control Systems- A Survey.* Automatica, Vol. 28, No. 6, pp. 1083-1112, 1992.

45. S. Haykin. *Neural Networks.* Macmillan College Publishing Company, Inc. 1994.

46. Y. Xue and J. Watton *Dynamics Modelling of Fluid Power Systems Applying a Global Error Descent Algorithm to a Self-organising Radial Basis Function Network.* Mechatronics, Vol. 8, pp. 727-745, 1998.

47. Simon Haykin. *Neural Networks: A Comprehensive Foundation.* Prentice-Hall, Inc., New Jersey, Second Edition, 1999.

48. Mead C. A., *Analog VLSI and Neural Systems.* Addison-Wesley, Reading, MA, USA, 1989.

49. G. Cybenko. *Approximation by Superposition of Sigmoidal Function.* Math, Control Signal System, Vol. 2, pp. 303-314, 1989.

50. G. Gammarata, A. Fichere, C. Losenno and A. Pagan. *Modelling Combustion Instability with a Neural Network.* Proceedings of the Sixth International Conference on Technologies and Combustion for a Clean Environment, pp. 941-944. Edificio da Alfandega, Oporto, Portuga. 9-12 July, 2000.

51. Ramana Vitthal, P. Sunthar and CH. Durgaprasada Rao. *The Generalized Proportional-Integral-Derivative (PID) Gradient Descent Back Propagation Algorithm.* Neural Network, Vol. 8, No. 4, pp. 563-569, 1995.

52. D. McCloy. *Control of Fluid Power: Analysis and Design (2^{nd} (Revised) Edition).* Ellis Horwood Limited, Chichester, UK, 1980.

53. Stewart H. L. and Store J. M.. *Fluid Power,* Howard W. Sams & Co.., USA, 1968.

54. Watton J.. *Fluid Power Systems: Modeling, Simulation, Analog and Microcomputer Control.* Prentice Hall, UK, 1989.

55. R. Courant and K. O. Friedrichs. *Supersonic Flow and Shock-Wave.* Interscience Publisher, New York, USA, 1948.

56. Mary Lister. *The numerical Solution of Hyperbolic Partial Differential Equations by the Method of Characteristics*. Mathematical Methods for Digital Computers, pp. 165-179, Wiley, New York, USA, 1960.

57. Hartree D. R.. *Some Practical Methods of Using Characteristics in the Calculation of Non-steady Compressible Flow*. Harvard University, Department of Mathematics, Report LA-HU-1, 1953.

58. Streeter V. L. and Wylie E. B.. *Hydraulic Transients*. McGraw-Hill, New York, USA, 1967.

59. J. R. Manning. *Computerized Method of Characteristics Calculations for Unsteady Pneumatic Line Flows*. Journal of Basic Engineering, Transaction of the ASME, pp. 1-10, June, 1968.

60. S. Ikeo, H. Zhang and K. Takahashi. *Simulation of Pneumatic Systems Using BGSP*. Sixth Bath International Fluid Power Workshop, pp. 11-14, 1993, Bath, UK.

61. P. Krus, A. Jansson, J-O. Palmberg and K. Weddfelt. Distributed Simulation of Hydromechanical Systems. Third Bath International Fluid Power Workshop, 1990, Bath, UK.

62. Petter Krus. *Distributed Modelling for Simulation of Pneumatic Systems*. Forth JHPS International Symposium on Fluid Power, pp. 443-452, 1999, Tokyo, Japan.

63. Bao Gang, Li Yujun and Wang Zuwen. *The Calculation of Two-dimension Viscous Field in Tube of Pneumatic System*. 5th International Conference on Fluid Power Transmission and Control (ICEP 2001), pp. 293-243, 2001, Zhejiang University, P.R. China.

64. Xue Y. and Yusop M. Y. M.. *Time Domain Simulation of Air Transmission Lines*, 8th International Symposium on Fluid Control, Measurement and Visualization (FLUCOME), Paper 277, 2005, Chengdu, P. R. China.

65. Sorli M. and Franco W.. *Gas Line Pulse Analysis*. Sixth International Symposium on Fluid Control, Measurement and Visualization, 13-17 Aug 2000, Sherbrooke, Canada.

66. Sorli M. and Franco W.. *Pneumatic Line Transients*. The Seventy International Conference on Fluid Power, SUCFP'01, pp. 181-196, 30 May-1 June, 2001, Linkoping, Sweden.

67. W. Franco and M. Sorli. *Time-domain Models for Pneumatic Transmission Lines*. Bath Workshop on Power Transmission and Motion Control, pp. 257-268, 2004, Bath, UK.

68. C. A. J. Fletcher. *Computational Techniques for Fluid Dynamics: Volume 1, Fundamental and General Techniques (Second Edition)*. Springer, New York, USA, 2000.

69. C. A. J. Fletcher. *Computational Techniques for Fluid Dynamics: Volume 2, Specific Techniques for Different Flow Categories (Second Edition)*. Springer, New York, USA, 2000.

70. John D. Anderson, Jr.. *Modern Compressible Flow with Historical Perspective (Second Edition)*. McGraw-Hill, USA, 1990.

71. M. B. Abbott and D. R. Basco. *Computational Fluid Dynamics: an Introduction for Engineers*. Longman Group Limited, UK, 1989.

72. Roger Peyret and Thomas D. Taylor. Computational Methods for Fluid Flow. Springer-Verlag, New York, USA, 1983.

73. Victor L. Streeter and E. Benjamin Wylie. *Fluid Mechanics (First SI Metric Edition)*. McGraw-Hill Ryerson, 1983.

74. H. K. Versteeg and W. Malalasekera. *An Introduction to Computational Fluid Dynamics (The Finite Volume Method)*. Longman Group Ltd., 1995.

75. L. M. Milne-Thomson. *Theoretical Hydrodynamics (Fifth Edition)*. Macmillan, London, UK, 1968.

76. Y. Xue, Y. Qin, M Y Yosup and N. Syred. *Time Domain Simulation for Pneumatic Transmission Line*. Submitted to Proceedings I of IMechE.

77. G. Carducci, N. I. Giannoccaro, *A. Messina and G. Rollo. Identification of Viscous Friction Coefficients for a Pneumatic System Model Using Optimization Methods*. Mathematics and Computers in Simulation, Vol. 71, pp. 385-394, 2006.

78. Andersen B. W.. *The Analysis and Design of Pneumatic Systems*. John Wiley, UK, 1968.

79. Blackburn J. F., Reethof G., and Shearer J. L.. *Fluid Power Control*. MIT Press, USA, 1960.

80. V. Vemuri and Walter J. Karplus. *Digital Computer Treatment of Partial Differential Equations*. Prentice-Hall, UK, 1981.

81. Lax P. D., and Wendroff B. *Systems of Conversation Laws*. Commun. Pure Appl. Math., Vol 13, pp. 217-237, 1960.

82. Peter D. Lax. *Hyperbolic Systems of Conservation Laws and the Mathematical Theory of Shock Waves*. Society for Industrial and Applied Mathematics, 1973.

83. MacCormack R. W.. *The Effect of Viscosity in Hypervelocity Impact Cratering*. AIAA Paper, 69-354, Cincinnati, Ohio, 1969.

84. MacCormack R. W.. *A Perspective on a Quarter Century of CFD Research*. AIAA Paper, 85-0032, Reno, Nevada.

85. Arthur H. Lefebvre. *Gas Turbine Combustion*. Taylor & Francis, USA, 1983.

86. Williams F. A.. *Combustion Theory (Second Edition)*. Benjiamin Cummings, Menlo Park, USA, 1985.

87. Jerzy Chomiak. *Combustion: A Study in Theory, Fact and Application*. Gordon and Breach, Switzerland, 1990.

88. J. R. Cornforth. *Combustion Engineering and Gas Utilisation (Third Edition)*. E & FN Spon, UK, 1992.

89. Gary L. Borman. *Combustion Engineering*. McGraw-Hill, USA. 1998.

90. Stephen R. Turns. *An Introduction to Combustion: Concepts and Applications (Second Edition)*. McGraw-Hill, Boston, USA, 2000.

91. Kenneth K. Kuo. *Principles of Combustion*. John Wiley & Sons, New Jersey, USA, 2005.

92. Tyndall J.. *Sound*. D. Appleton & Co., New York, USA. 1897.

93. R. Blonbou, A. Laverdant, S. Zaleski and P. Kuentzmann. *Active Control of Combustion Instabilities on a Rijke Tube Using Neural Networks*. Proceedings of the Combustion Institute, Vol. 29, pp. 747-755, 2000.

94. Fureby C.. *Large Eddy Simulations of Pulsating Combustion*. Doctoral Dissertation, Lund Institute of Technology, Lund, Sweden, 1995.

95. Benelli G., Cossalter V., and Da Lio M.. *Advances in Numerical Simulation at ENEL*, Combustion Science and Technology, 94:317-335, 1993.

96. Annaswamy A. M. and Ghoniem A. F.. *Active Control in Combustion Systems*. IEEE Contr. Syst. Mag., Vol. 15. pp. 49-63, 1995.

97. Culick F. E. C.. *Some Recent Results for Nonlinear Acoustics in Combustion Chambers*. AIAA Journal, Paper 90-3927, Vol. 32, No. 1, pp. 146-169, 1996.

98. Krstic M., Krupadanam A., Jacobson C.. *Self-tuning Control of Nonlinear Model of Combustion Instabilities*. IEEE Trans. Contr. Syst. Techn., Vol. 7, No. 4, pp. 424-436, 1999.

99. L. Cammarata, A. Fichera and A. Pagano. *Neural Prediction of Combustion Instability*. Applied Energy, Vol. 72, 513-528, 2002.

100. F. C. Christo, A. R. Masri and E. M. Nebot. *Utilising Artificial Neural Network and Repro-modelling in Turbulent Combustion*. IEEE International Conference on Neural Networks, Vol. 2, pp. 911-916, 1995, Perth, Australia.

101. E. Gutmark, T. P. Parr, D. M. Hanson-Parr and K. C. Schadow. *Use of Chemiluminescence and Neural Networks in Active Combustion Control*. Twenty-

Third Symposium (International) on Combustion/The Combustion Institute, pp. 1101-1106, 1990.

102. K. R. McManus, T. Poinsot and S. M. Candel. *A Review of Active Control of Combustion Instabilities*. Prog. Energy Combust. Sci., Vol. 19, pp. 1-29, 1993.

103. G. P. Liu and S. Daley. *Output-model-based Predictive Control of Unstable Combustion Systems Using Neural Networks*. Control Engineering Practice, Vol. 7, pp. 591-600, 1999.

104. Nicolas Docquier and Sebastien Candel. *Combustion Control and Sensors: a Review*. Progress in Energy and Combustion Science, Vol. 28, pp. 107-150, 2002.

105. N. Peters. *A Spectral Closure for Premixed Turbulent Combustion in the Flamelet Regime*. Journal of Fluid Mechanics, Vol. 242, pp. 611-629, 1992.

106. Hans-Peter Schmid, Peter Habisreuther and Wolfgang Leuckel. *A Model for Calculating Heat Release in Premixed Turbulent Flames*. Combustion and Flame, Vol. 113, Issues 1-2, pp. 79-91, April 1998.

107. C. Hirsch, J. Wasle, A. Winkler and T. Sattelmayer. *A Spectral Model for the Sound Pressure from Turbulent Premixed Combustion*. Proceedings of the Combustion Institute, 2006, doi:10.1016/j.proci.2006.07.154.

108. G. A. Richards, G. J. Morris, D. W. Shaw, S. A. Keeley, and M. J. Welter. *Thermal Pulse Combustion*. Combustion Science and Technology, Vol. 94, pp. 57-88, 1993.

109. S. Marsano, P. J. Bowen and T. O'Doherty. Cyclic Modulation Characteristics of Pulse Combustors. Twenty-Seventy Symposium (International) on Combustion/The Combustion Institute, pp. 3155-3162, 1998.

110. Hamid Momahedi Heravi. *Integrated Physical and Chemical Modelling of Pulse Combustor*. PhD Thesis, Division of Mechanical Engineering and Energy Studies, Cardiff University, 2003.

111. Andrew John Beale. *Aerovalved Pulse Combustion*. PhD Thesis, Division of Mechanical Engineering and Energy Studies, Cardiff University, 1999.

112. Richard K. Pefley and R. Ian Murray. *Thermofluid Mechanics*. McGraw-Hill, USA, 1966.

113. Y. Nakayama and R. F. Boucher. *Introduction to Fluid Mechanics*. Arnold, UK, 1999.

114. Schlichting Herrmann, and Klaus Gersten. *Boundary-layer Theory*. Springer, New York, USA, 2000.

115. Samuel Glasstone, Keith J. Laidler and Henry Eyring. *The Theory of Rate Processes (Fifth Edition)*. McGraw-Hill, USA, 1941.

116. Warren M. Rohsenow and Harry Y. Choi. *Heat, Mass, and Momentum Transfer.* Prentice-Hall, New Jersey, 1961.

117. A. J. Reynolds. *Thermofluid Dynamics.* John Wiley & Sons, Hungary, 1971.

118. Frank P. Incropera and David P. De Witt. *Fundamentals of Heat Transfer.* John Wiley & Sons, Canada, 1981.

119. Gordon J. Van Wylen and Richard E. Sonntag. *Fundamentals of Classical Thermodynamics (Third Edition).* John Wiley & Sons, Canada, 1985.

120. Arthur Shavit and Chaim Gutfinger. *Thermodynamics from Concepts to Application.* Prentice Hall, UK, 1995.

121. Michael J. Moran and Howard N. Shapiro. *Fundamentals of Engineering Thermodynamics (Fifth Edition).* John Wiley & Sons, Chichester, UK, 2006.

122. J. W. Rose and J. R. Cooper. *Technical Data on Fuel. British National Committee World Energy Conference,* 1977.

123. Perry J. *H.. Chemical Engineers Handbook.* McGraw-Hill, New York, USA, 1984.

124. W. H. Avery and R. W. Hart. *Combustor Performance with Instantaneous Mixing.* Industrial and Engineering Chemistry, Vol. 45, pp. 1634-1637, 1953.

125. John P. Longwell and Malcolm A. Weiss. *High Temperature Reaction Rates in Hydrocarbon Combustion.* Industrial and Engineering Chemistry, Vol. 47, Part 8, pp. 1634-1648, 1956.

126. A. E. Clarke, A. J. Harrison and J. Odgers. *Combustion Stability in a Spherical Combustor.* Prod. of the 7th International Symp. on Combustion, pp. 664-673, 1959, London, UK.

127. D. Kertschmer and J. Odgers. *Modelling of Gas Turbine Combustors-A Convenient Reaction Rate Equation.* Journal of Engineering for Power, 173-180, July 1972.

128. Zinn B. T.. *Pulsating Combustion.* In Advanced Combustion Methods, F. J. Weinberg, ed., pp. 151-154, 1986.

129. William H. Press, Brain P. Flannery, Saul A. Teukolsky and William T. Vetterling. *Numerical Recipes.* Cambridge University Press, Cambridge, UK, 1986.

130. James H. McClellan and Charles M. Rader. *Number Theory in Digital Signal Processing.* Prentice-Hall, London, 1979.

131. V. Cappellini and A. G. Constantinides. *Digital Signal Processing.* Academic Press, London, 1980.

132. Adrian Biran and Moshe Breiner. *Matlab for Engineers.* Addison-Wesley Pub. Co., Reading, UK, 1995.

133. Ke Chen, Peter Giblin and Alan Irving. *Mathematical Explorations with Matlab.* Cambridge University Press, Cambridge, 1999.

134. Ziegler J. G., Nichol N. B.. *Optimum Settings for Automation Controllers.* Trans ASME, Vol. 64, pp. 759–768, 1942.

135. Katsuhiko Ogata. *Modern Control Engineering.* Prentice-Hall, Inc., NJ, 1997.

136. Rayleigh J. W.. *The explanation of certain acoustical phenomena.* Royal Institute Proceedings, London, 1978, 3:536-42.

137. Moody F. J.. *Introduction to Unsteady Thermofluid Mechanics.* Wiley, New York, USA, 1990.

PUBLISHED PAPERS

Xue Y., Syred N., Rodriguez-Martinez V. M., Doherty T. and Qin Y.. *Dynamic Modelling of a Swirl Burner Using Artificial Neural Networks.* Proceedings combustion and noise control symposium, B Cranfield University Press, (2003)

Xue Y., Qin Y. and Syred N.. *Controller Prediction Using Artificial Neural Networks.* 4th Conference on Applied Cybernetics, IEEE Systems, Man and Cybernetics Society, UK and Ireland Chapter, London 2005, pp. 100-104, ISSN 1774-9189.

SUBMITTED PAPERS

Xue Y., Qin Y., Yosup M. Y. and Syred N.. *Time-domain Simulation for Pneumatic Transmission Line.* Submitted to Proceedings I of IMechE